3D-printed Stimuli-responsive Soft Microrobots

Von dem Stuttgarter Zentrum für Simulationswissenschaften (SC SimTech) der Universität Stuttgart zur Erlangung der Würde eines Doktor-Ingenieurs (Dr.-Ing.) genehmigte Abhandlung

Vorgelegt von

Yunwoo Lee

aus South Korea

Hauptberichter: Prof. Dr. Metin Sitti

Mitberichter: Prof. Dr. Syn Schmitt

Mitberichter: Prof. Dr. Hakan Ceylan

Tag der mündlichen Prüfung: 11. September 2023

Max-Planck-Institut für Intelligente Systeme

2023

Dedicated to my beloved family

Acknowledgments

First and foremost, I would like to express my sincere gratitude to my supervisor, Prof. Metin Sitti for his full of support and guidance with his wisdom and creativity during my research. Without his support and guidance, I could not finish my Ph.D. and the dissertation. Thank you again for giving me an opportunity to work in the Physical Intelligence Department at the Max Planck Institute for Intelligent Systems. I also greatly appreciate Prof. Syn Schmitt and Prof. Johannes Kästner for serving on my examination committee and for all their guidance.

I deeply wish to express thanks to Prof. Hakan Ceylan for his warm mentorship and support through the initial stage of my Ph.D. He helped me become a better researcher. It was great pleasure working with him on the stimuli-responsive microswimmer project. I would like to thank my amazing research collaborators, Dr. Ceren Yasa, Dr. Ugur Bozuyuk, Nihal Olcay Dogan, Muhammad Turab Ali Khan, Anitha Shiva, Dr. Anna-Maria Wild, Ugur Kilic, Dr. Xinghao Hu, Dr. Martina Schneider, and all our technical staff for always being helpful. They gave me advice and offered meaningful discussions during my entire Ph.D.

I also greatly appreciate my fellows of the Physical Intelligence Department. I had an unforgettable time in my life with wonderful people during my PhD time, especially Prof. Amirreza Aghakhani, Dr. Meng Li, Dr. Aniket Pal, Birgül Akolpoglu, Saadet Baltaci, Dr. Yingdan Wu, Dr. Aarushi Bhargava, Dr. Muhammad Yunusa, Dr. Mingchao Zhang, Dr. Guarav Gardi, Ren Hao Soon, Cem Balda Dayan, Dr. ShuaiZhong Zhang, Dr. Zhiqiang Zheng, Jie Han, Chong Hong, Li Mingtong, Dr. Savas Tasoglu, Yingbo Yan, Dr. Wenbin Kang, Dr. Wei Feng, Nagaraj Krishna-Subbaiah, Asli Aydin, Zemin Liu, Dr. Mingchao Zhang, Dr. Martin Phelan, Dr. Ziyu Ren, Dr. Mehmet Efe Tiryaki, Fan Wang, Paul Wrede, Dr. Gaurav Gardi, Dr. Yunus Alapan, Anitha Shiva, Prof. Morteza Amjadi, Dr. Alp Can Karacakol, Xianglong Lyu, Dr. Yunus Alapan, Dr. Tianlu Wang, Dr. Utku Culha, Devin Sheehan, Prof. Zoey Davidson, Prof. Xiaoguang Dong, Dr. Dirk Drotlef, Dr. Onder Erin, Dr. Pelin Erkoc, Prof. Abdon Pena-Francesch, Dr. Joshua Giltinan, Dr. Erdost Yildiz, Dr. Chantal Göttler, Dr. Sandhya Rani Goudu, Prof. Yubing Guo , Prof. Vimal Kishore, Prof. Kristen Kozielski, Dr. Ville Liimatainen, Musab Cagri Ugurlu, Prof. Guo Zhan Lum, Prof. Hamed Shahsavan, Dr. Ajay Vikram Singh, Dr. Sukho Song, Dr. Yichao Tang, Prof. Wendong Wang, Prof. Matthew Woodward, Dr. Oncay Yasa, Dr. Mehmet Berk Yigit, and Prof. Jiachen Zhang. I would also like to show my deepest gratitude to my officemates Hyungyu Kim, Dr. Varun Sridhar, and Nima Mahkam. They were always around and supported me during my Ph.D life. I deeply thank Patricia Martinez, Janina Schwartz, Jack Saud, Gerd Hoerner, Ildikó Papp-Wiedmann, and Eugenia Komnik for their administrative support.

I also would like to express sincere gratitude to Prof. Jongkuk Ko and Prof. Jaekang Kim. Without their help, the last part of my Ph.D. work would have not been possible. I am indebted to Dr. Jaekang Kim again for having interesting academic discussions with numerous cups of coffee. In addition, I am very grateful to my Korean friends in our group, Prof. CK Yoon, Prof. Byung-Wook Park, Prof. Kwanghyo Son, Prof. Dong-hoon Son, Prof. Sungwoo Chun, Dr. Junghwan Byun, Dr. Dongwook Kim, Siyeon Jang, and Dr. Dongha Tahk.

Finally, I would like to express my special and deepest gratitude to my family, Jong Woo Lee, Keum Hee Hwang, Eun Jo Lee, Isaac Chung and Jin Seo Lee. They gave endless support and love to me. They have been a great motivation and energy source for me during my Ph.D.

Abstract

Untethered microrobots, i.e., mobile microrobots, with overall sizes less than 1 mm are receiving significant attention due to their great potential to conduct targeted and minimally invasive therapeutic delivery and medical treatment of diseases in the local region of the biological environment. However, there are many technical barriers in the integration of conventional on-board sensors, actuators, and batteries into micro-scale systems. To overcome these limitations, stimuli-responsive active materials with both sensing and actuation properties are integrated to mobile microrobots. Stimuli-responsive materials can morph their shape and size via swelling and deswelling mechanisms in response to external chemical, physical and other stimuli, such as heat, pH, light, magnetic field, and acoustic field, with no aid from complex wires, sensors, or batteries.

While conventional fabrication methods with passive materials have led to the production of static structures, 3D printing with stimuli-responsive materials opens a new direction for 3D objects possessing volumetric transformation behavior, material property change, and shape morphing ability. In this dissertation, I integrate different stimuli-responsive materials and 3D microprinting to provide more multifunctional, versatile and complex microrobot designs based on bioinspired design principles, with a wide range of stimuli-responsive sensing and actuation properties to use them in potential biomedical applications inside the human body.

In the first part, I introduce magnetically steerable 3D-printed microroller and microscrew robot designs with stimuli-responsive materials to develop volume-controllable microrobots for spatial adaptation. These wirelessly controlled microrobots possess the ability to function in response to multiple stimuli, including magnetic fields, temperature, pH, and cations, which can enhance the adaptability of the microbots to various unstructured environments.

Second, octopus-inspired architectures with temperature-responsive materials to control the adhesion properties for medical purposes is proposed. Introduction of pNIPAM material leads temperature-responsive volume morphing behavior enabled controllable tissue adhesion by using externally applied magnetic fields. Furthermore, I demonstrate the capability of implementing a wide range of medical tasks repeatedly via showing the repetition of attachment and detachment processes using an external magnetic field.

Finally, I present a multifunctional pollen-grain-inspired hydrogel robot by 3D direct laser printing in order to enhance the functional diversity of microrobots in biological environments. I also demonstrated multi-responsive hydrogel structures to decouple the stimulus inputs of magnetically actuated locomotion, temperature-responsive controllable attachment, and pH-responsive on-demand cargo release, respectively. The temperature-responsive outer crust shells made of pNIPAM enabled controlling the attachment of the microrobot by shrinking up to 49%, revealing the robot's spikes. In addition, the inner pollen-grain-inspired structure with spikes made of PETA with FePt nanoparticles demonstrated an improved attachment performance and magnetically guided locomotion along biological surfaces. The inner sphere made of pNIPAM-AAc successfully released drugs by pH-induced swelling.

Zusammenfassung

Ungebundene Mikroroboter sind Roboter im Submikrometerbereich, die wegen ihres großen Potenzials aufgrund ihrer Fähigkeit zur gezielten und minimalinvasiven therapeutischen Verabreichung und medizinischen Behandlung von Krankheiten in der lokalen Region der biologischen Umgebung Beachtung finden. Es gibt jedoch viele technische Hindernisse bei der Integration herkömmlicher Sensoren, Aktoren und Batterien in Systeme im Mikromaßstab, die dazu führen können, dass der Zweck der realisierbaren Funktionalität in schwer zugänglichen Bereichen zunichte gemacht wird. Um diese Einschränkungen zu überwinden, werden andere selbsterfassende und aktivierende Materialien untersucht, um passive und statische Materialien zu ersetzen. Auf Stimuli ansprechende Materialien können ihr Volumen über Quell- und Abschwellmechanismen als Reaktion auf externe chemische oder physikalische Auslöser wie Hitze, pH-Wert, Licht, Magnetfeld und Akustik ohne Hilfe von komplexen Drähten, Sensoren oder Batterien verändern.

Während herkömmliche Herstellungsmethoden mit passiven Materialien zur Herstellung statischer Strukturen geführt haben, schlägt der 3D-Druck mit stimuliresponsiven Materialien eine neue Richtung für 3D-Objekte vor, die ein volumetrisches Transformationsverhalten, Änderungen der Materialeigenschaften und die Fähigkeit zur Formveränderung aufweisen. In dieser Dissertation integriere ich die verschiedenen stimuliresponsiven Materialien und den Mikro-3D-

Druck, um Multifunktionalität, höhere Vielseitigkeit, komplexeres Design basierend auf bioinspiriertem Design und ein breites Spektrum an Stimuli-Response bereitzustellen, um neue Horizonte im Design verschiedener zu eröffnen medizinische Roboter und Geräte zur Umsetzung biomedizinischer Funktionen im Körper.

Im ersten Teil demonstriere ich die Einführung von magnetisch steuerbaren 3D-gedruckten Mikrorollen- und Mikroschraubendesigns mit stimuliresponsiven Materialien, um volumensteuerbare Mikroroboter zur räumlichen Anpassung zu entwickeln. Diese drahtlos gesteuerten Mikroroboter besitzen die Fähigkeit, als Reaktion auf mehrere Reize zu funktionieren, darunter Magnetfelder, Temperatur, pH-Wert und Kationen, was die Anpassungsfähigkeit der Mikrobots an verschiedene unstrukturierte Umgebungen verbessern kann.

Zweitens werden Oktopus-inspirierte Architekturen mit temperaturempfindlichen Materialien zur Steuerung der Adhäsionseigenschaften für medizinische Zwecke vorgeschlagen. Die Einführung von pNIPAM-Material führt zu einem temperaturabhängigen Volumenmorphing-Verhalten, das eine kontrollierbare Gewebeadhäsion durch die Verwendung von extern angelegten Magnetfeldern ermöglicht. Darüber hinaus demonstriere ich die Fähigkeit, verschiedenste medizinische Aufgaben wiederholt umzusetzen, indem ich die Wiederholung von An- und Ablösevorgängen mit einem externen Magnetfeld zeige.

Drittens stelle ich einen multifunktionalen, von Pollenkörnern inspirierten Hydrogel-Roboter durch 3D-Laserdirektdruck vor, um die funktionelle Vielfalt von Mikrorobotern in biologischen Umgebungen zu verbessern. Ich habe auch multiresponsive Hydrogelstrukturen demonstriert, um die Stimuluseingaben von magnetisch aktivierter Fortbewegung, temperaturgesteuerter kontrollierbarer Befestigung bzw. pH-responsiver Ladungsfreisetzung auf Abruf zu entkoppeln. Die temperaturempfindlichen äußeren Krustenschalen aus pNIPAM ermöglichten die Steuerung der Befestigung des Mikroroboters, indem sie um bis zu 49 % schrumpften und die Stacheln des Roboters freilegten. Darüber hinaus zeigte die innere Pollenkörner-inspirierte Struktur mit Spikes aus PETA mit FePt-Nanopartikeln eine verbesserte Bindungsleistung und magnetisch geführte Fortbewegung entlang biologischer Oberflächen. Die innere Sphäre aus pNIPAM-AAc setzte Arzneimittel erfolgreich durch pH-induziertes Quellen frei.

Table of Contents

List of Figures

Chapter 1. Introduction

Three-dimensional (3D) printing technology, known as additive manufacturing, has gained great interest from researchers and engineers due to its tremendous benefits as fast prototyping, low cost in production, in-time fabrication, and capability of printing very accurate, complex structures.[1] The 3D solid objects can be fabricated using different materials including polymers, metals, ceramics, and composites.[2-5] The capability of 3D printing allows different industries and applications to be broadly used, such as in aerospace[6], electronics[7], robotics[8], and healthcare.[9-11] Commonly used 3D printing has many different techniques are stereo-lithography, digital light processing, fused deposition modeling, and direct writing methods.[12-15]

As the 3D printing technology advances, innovation of the new material for 3D printing technology was led to possessing the capability to morph their structural shape and properties in response to different stimuli.[16-18] These innovations of materials may lead to simplification of the design and fabrication process, cost-effectiveness, and automation of structure. While conventional 3D printing with passive material led to the production of static structures, the 3D printing with stimuli responsive materials suggest a new direction to 3D objects possessing a volumetric transformation behavior, material property changes and shape morphing ability.[19] These stimuli-responsive behaviors are activated in response to external triggers, such as temperature[20], light [21], ultrasound[22] , pH[23-24] , and voltage[25] , among other environmental stimuli.

In terms of the size scale, 3D printing provides a wide spectrum of sizes ranging from large macroscale objects to very small objects.[26] One of the targeted applications for micro and nano-size objects is microrobots. Traditional robots are more than centimeter scale, which composed of DC/AC motors, and numerous assembled structures. However, micro-scale mobile robots

commonly refer to the robot with size less than 1 mm. The micro size of the robot enables them to access the hard-to-reach local sites such as the intestine, blood vessels, and other narrow harsh environments of the human body.

Unlike traditional robots, microrobots are typically relied on materials with less complicated, straightforward designs. Thus, the integration of 3D printing and stimuli-responsive material at a micro scale possess high potential in the field of microrobotics.[27-29] Traditional 3D printing with passive materials is highly limited in terms of design, geometries, and functionalities. However, the introduction of stimuli-responsive and 3D micro printing system could render diverse designs, materials, and functionalities to the field of microrobots. (Figure 1.1)

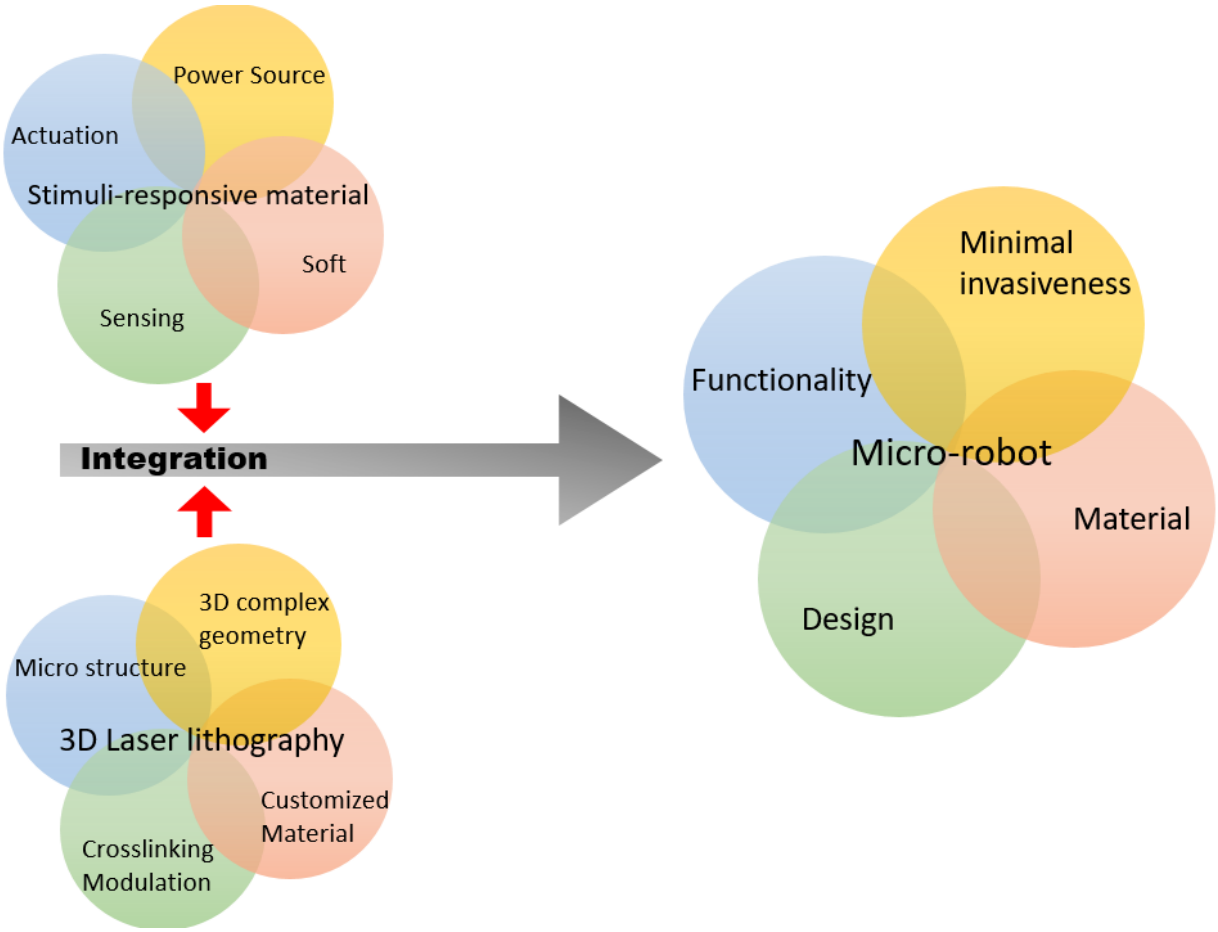

Figure 1.1 Features of integration of 3D printing, stimuli-responsive materials and mobile microrobots.

1.1 Untethered actuation methods for microrobots

In untethered mobile microrobots, current miniaturization limitations constrain their on-board actuation, powering and propulsion capabilities. Different untethered approaches, such as, chemical, light, acoustic and magnetic, have been proposed to solve such issue.[30] One of the prominent untethered approaches is magnetic actuation since it possesses capability of long-range, precise, fast, and robust actuation and controllability.

1.2 Magnetic actuation of mobile microrobots

Magnetically actuated microrobots transform magnetic energy into mechanical energy, which is available in the form of magnetic field gradient-based pulling force or magnetic field-based torque to propel the microrobots.[31] One of the most prominent methods of remote actuation toward bioengineering application is magnetically driven propulsion methods, since they are mostly compatible with the living organisms by safely penetrating into biological tissues.[32]

An external permanent magnet or electromagnetic coil system exerts pulling magnetic forces or rotating magnetic torques on microrobots with a hard or soft magnetic body. The magnetic force (*F*) and magnetic torque (*T*) on the magnetic microrobot body is given by[33]

$$\vec{F} = V\left(\vec{M}\cdot\nabla\right)\vec{B} \tag{1a}$$

$$\vec{T} = V\,\vec{M}\times\vec{B} \tag{1b}$$

where *V* is the volume of the object, *M* is the magnetization, and *B* is the magnetic flux density. To get a continuous motion of the magnetic robot, the magnetic field varies spatially or temporally by using multiple electro-magnetic coils or multiple permanent magnets. By integrating magnetic

properties with other material responsive properties and structural designs, more advanced functions, such as shape memory, environmental adaptation and mechanical tunability, can be achieved.

One of the widely known swimming propulsion designs is helical magnetic microrobot body designs inspired by helical flagella of swimming bacteria. [34] They use helical rotation of their flagella to propel forward and steer in diverse fluids. Helical microrobot structures are composed or coated with magnetic materials and controlled by a rotating magnetic field. These helical structures are fabricated via different materials and fabrication approaches to use in a myriad of biomedical applications. (Figure 1.2)[35-37]

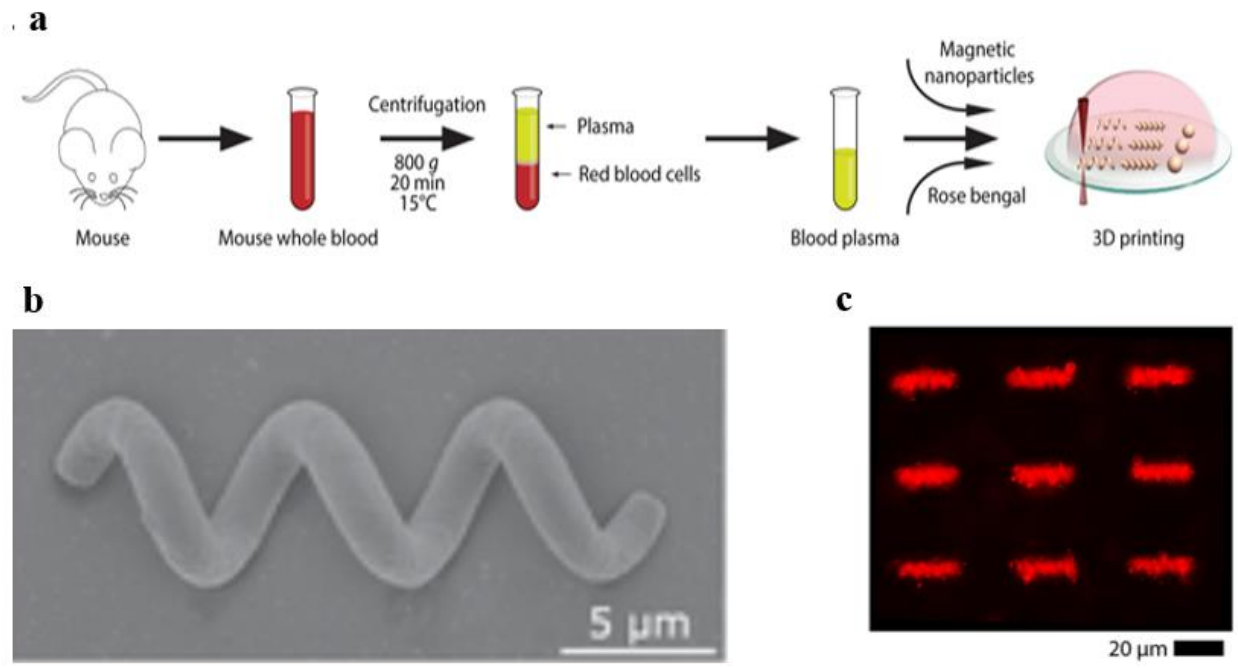

Figure 1.2 Examples of mobile microrobots actuated by magnetic field-based rotation. (a) 3D microprinting process of the mouse blood plasma-based helical microrobots. Reproduced from reference [36]. (b) Helical microrobot made of zwitterionic non-immunogenic materials.

Reproduced from reference [35]. (c) Fluorescence optical microscope image of a drug-encapsulated helical microrobot. Reproduced from reference [37].

1.3 Material Selection and Synthesis for Microrobots

In terms of material selection for the untethered micro-robots, their size is too small to embed power sources and actuators on board to implement such functions. To overcome such limitation, an innovative approach is required to create advanced microrobots using stimuli-responsive materials. Most stimuli-responsive materials morph their physical and chemical properties (rigidity, volume, shape) in response to external chemical or physical stimuli (pH[38], light[39], magnetic field[40], humidity[41], electricity[42]) without any support of sensors, actuators, and batteries (Figure 1.3). Particularly, temperature-responsive materials have been extensively used because temperature change is a common environmental and externally created stimulus. The temperature-responsive materials are composed of hydrophilic and hydrophobic groups to demonstrate their unique property, which is lower critical solution temperature (LCST).[43] LCST exhibits abrupt transition at the specific temperature. A widely used hydrogel with LCST is Poly N-isopropylacrylamide (pNIPAM).[44] Below the LCST of PNIPAM, the hydrogel undergoes expansion due to the hydrogen bonding of the hydrophilic groups to keep water inside the polymer network; at temperatures above the LCST, the hydrogel becomes hydrophobic to contract with expelling water out of its hydrogel matrix (Figure 1.4).

In addition to temperature responsiveness, pH-responsive stimuli-responsive systems are also common due to the variation of pH inside the human body or in the environment. The pH-dependent ionization of basic functional groups on hydrogel chains includes weak acid or alkaline

groups, such as carboxyl or amino because of the transition in their protonated/deprotonated states.[45-47] They swell or shrink in aqueous solutions of different pH values. Upon exposure to an aqueous solution with a pH value above its acidity constant (pKa), the −COOH group on the polymer chains deprotonates and creates the negatively charged −COO– group. The negatively charged molecular chains absorb more water, driving a significant expansion of the network size. Reversely, the carboxylate groups will be protonated when the pH value is lower than its pKa, driving off the water molecules and hence shrinking network size (Figure 1.5).

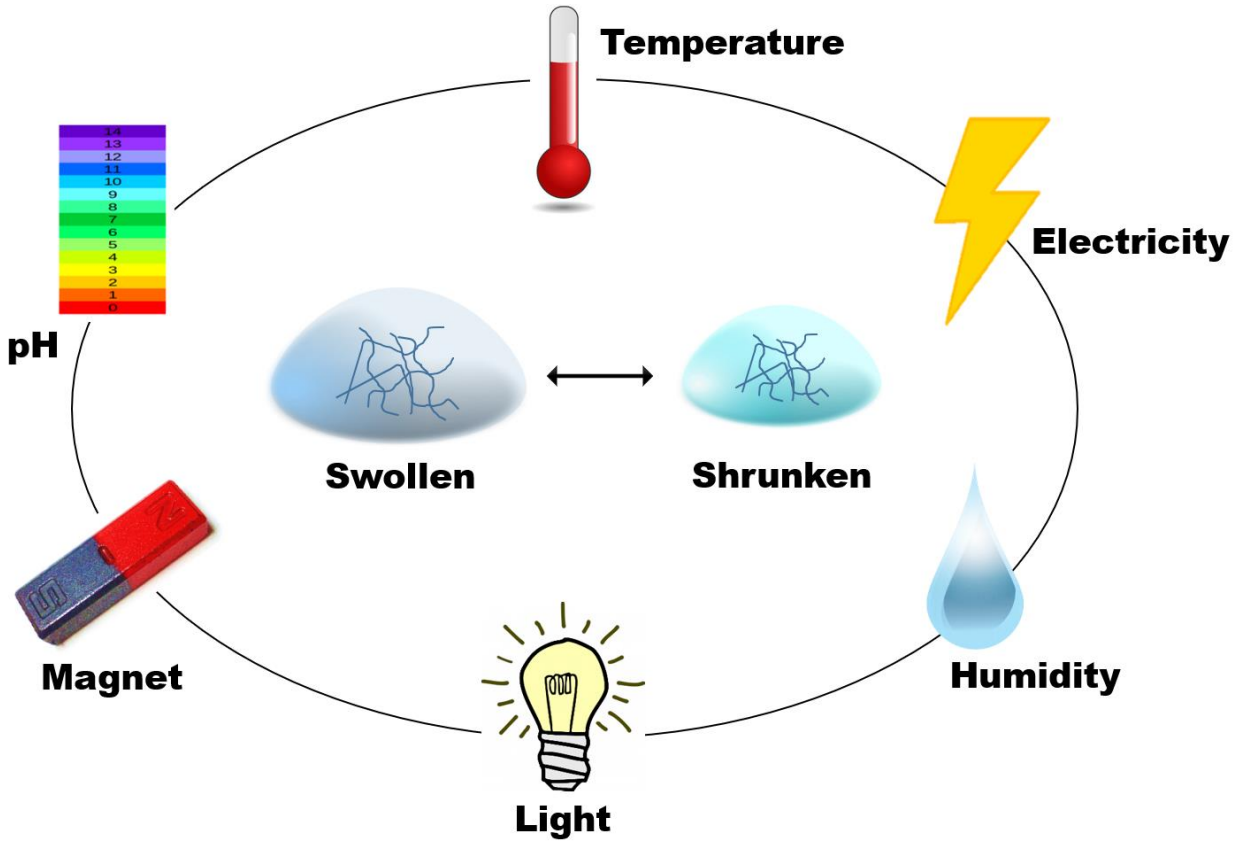

Figure 1.3 Volume transition of stimuli-responsive materials with reversible swelling/shrinking states in response to a wide range of environmental stimuli (temperature, electricity, pH value, magnetic field, light, and humidity).

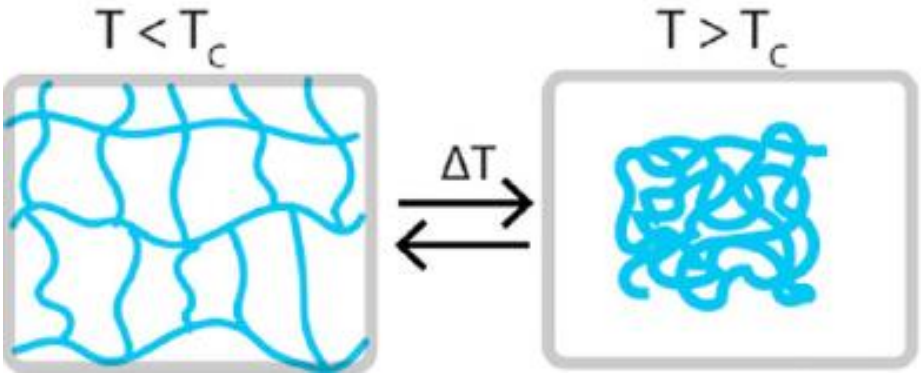

Figure 1.4 Schematic image of mechanism of temperature responsiveness: Left image shows under LCST state and right image shows above LCST image. Under LCST, they absorb water to well. Above LCST, they expel water to shrink. Reproduced from reference [48].

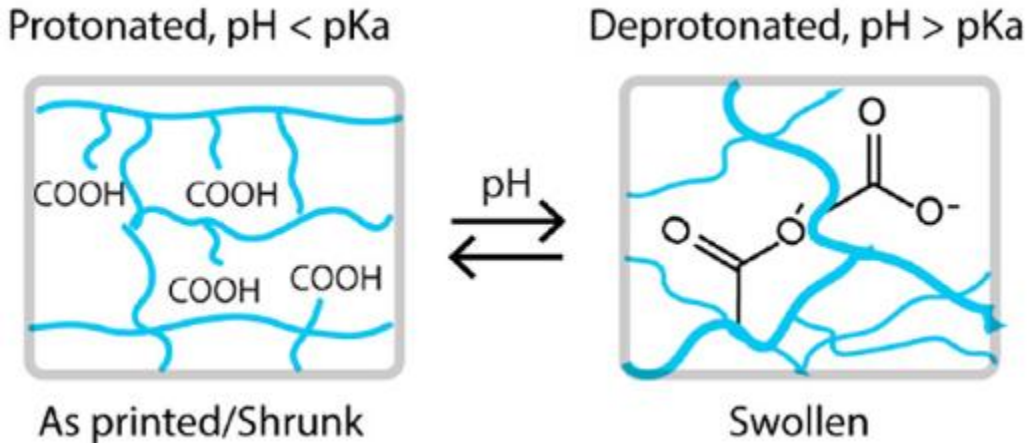

Figure 1.5 Schematic image of mechanism of pH responsiveness. At high pH, the carboxylic acid groups of the hydrogel expand due to deprotonation. At low pH, the groups of the hydrogel protonate to shrink. Reproduced from reference [48].

1.4 3D laser lithography at the microscale

As robots are miniaturized from macro to micro size, the fabrication technique is the most challenging part because widely used manufacturing systems are 2D-based fabrication processes, such as photolithography, and micro/nano-imprinting. (Figure 1.6) [49-51] However, those fabrication techniques possess limitations in miniaturization, design flexibility, functionality, and choice of materials.[52]

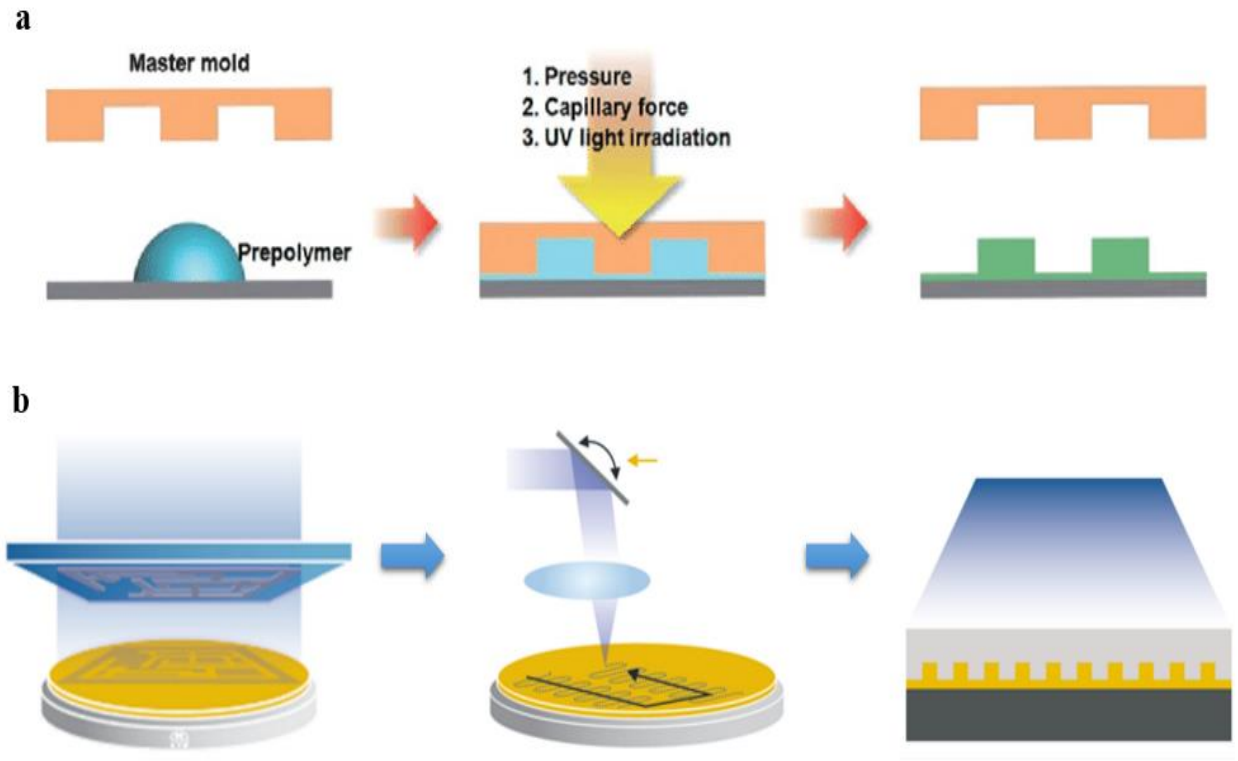

Figure 1.6 Schematic illustration of 2D microfabrication processes. (a) Micro-molding techniques. Reproduced from reference [49]. (b) Photolithography. Reproduced from reference [51].

In order to overcome the limitations, 3D laser lithography, also known as two-photon polymerization or direct-laser writing, has emerged alternatively by enabling the versatility of 3D microfabrication of light-sensitive resins with a sub-micrometer precision and feature size down to 100 nm.[53-54] In terms of the mechanism of 3D laser lithography, they absorb two or more photons simultaneously to allow the electrons transition to the state where not possible with a single photon as shown in Figure 1.7. This approach requires extremely short transition duration (scale of femtoseconds) so that the speed of the laser requires being fast enough to reach a higher state than single-photon absorption. The laser beam can only trigger tight focal point polymerization resulting in higher resolution compared to traditional methods. Recently, microprinting using 3D Laser lithography has been achieved mainly in developing 3D geometric designs, such as photonic structures[55], metamaterials[56], 3D scaffolds for cells[57], and microfluidics[58]. Despite the high level of structural information that could be printed by the 3D laser lithography, the resulting materials and systems lack spatial adaptability and functionality by shape morphing and chemical versatility.[59] These limitations also cause passive systems that are incapable of advanced smart spatial adaptability and functionality to serve as micro/nano soft robotic appliances in structural, mechanical, and biomedical applications. To overcome these restrictions, 3D laser lithography was used as an enabling tool for 3D microprinting with stimuli-responsive material. In other words, 3D-structure can morph their shape over time in response to stimuli or other environments.

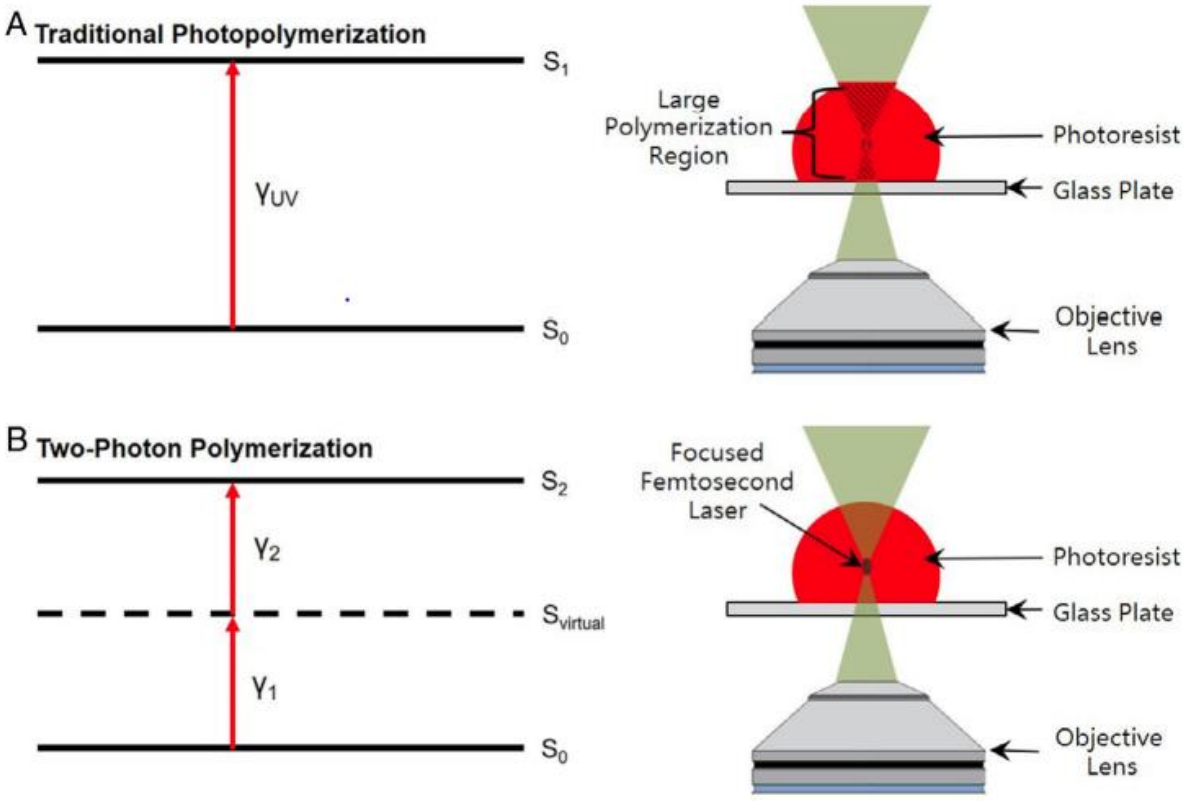

Figure 1.7 Schematic illustration of two-photon polymerization-based 3D laser lithography compared with traditional polymerization method. Reproduced from reference [60].

1.5 3D laser lithography using stimuli-responsive materials at the microscale

Despite the recent progress in the actuation, locomotion, and control capabilities of microrobots [61-63], a majority of the reported microrobots so far have been made from passive backbone materials[64], which possess simple actuation or sensing capabilities. They only provided a limited range of applications due to the lack of the versatility of the microrobot. To overcome this limitation and increase the functional capabilities of the microrobots, the integration of 3D laser lithography and stimuli-responsive material allows the fabrication of a newly suggested micro-sized robots that can be actuated in response to stimuli.

1.6 Effects of laser power on the material density of the structure of pNIPAM

Beyond the availability of use of stimuli-responsive materials, 3D laser lithography provides modulation of cross-linking density within the same structure.[65-66] When fabricating passive and static structures, only mechanical stability and fine fabricating conditions are the most important factors. For the selection of these non-responsive materials, I only consider strong and dense polymer networks via choosing crosslinkers composed of photo-reacted groups to develop. Therefore, high laser power and low scanning speed exhibit good mechanical stability and fine printing resolution whereas their degree of swelling or de-swelling of the material is highly restrained as shown in Figure 1.8. However, when it comes to use of stimuli-responsive materials to print, the balance of fabrication parameters plays a crucial role in the characteristics of stimuli-responsive structure. It is important matter for possessing both stability of the structure and how

much each part of the structure can be actuated in response to stimuli so that I could acquire a programmable design for the 3D structure.

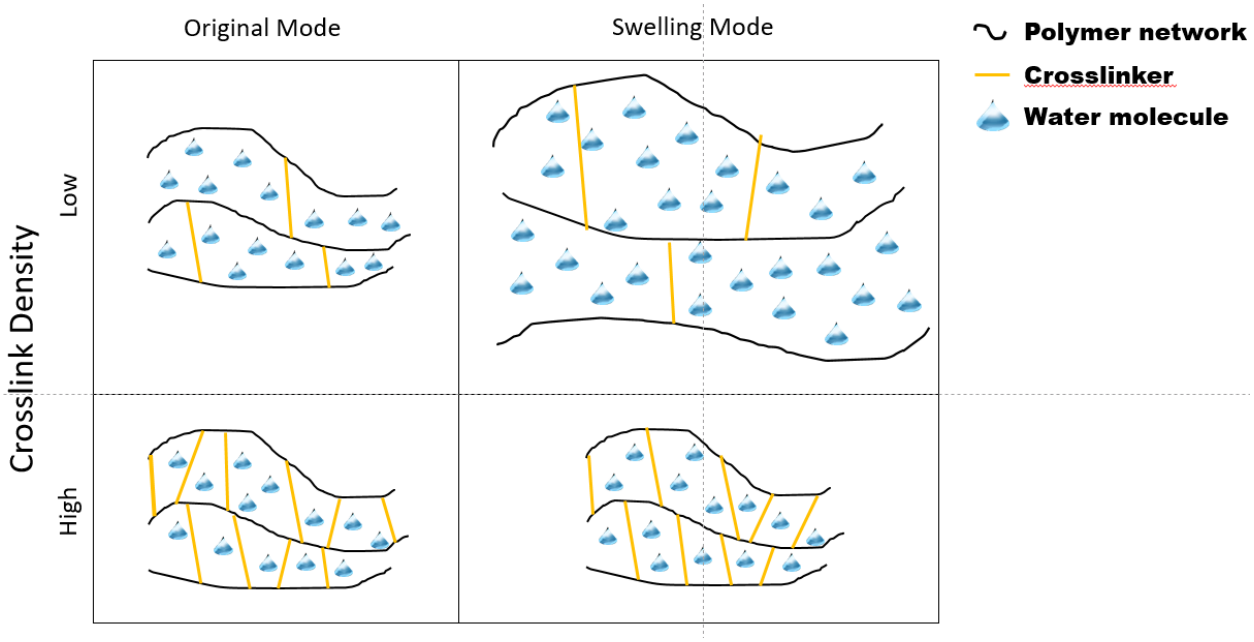

Figure 1.8 Schematic illustration of the effect of the crosslinking density on stimuli responsiveness. As the crosslinking density increases, mechanical stiffness increases whereas their responsiveness of the structure decreases. Crosslinking density is dependent on exposure dose of light.

1.7 Bioinspired design for adhesive part of microrobots

3D micro printing offers a great opportunity to add the versatility to the microrobot in terms of design and optimization of responsive microrobot due to the high availability of fabricating complex 3D shape structures and the use of materials. Especially, the customized 3D complex design allows for executing specific tasks in complex physiological and unstructured environments for personalized medical applications.[36] There has been efforts to investigate and design novel biomimetic synthetic microstructures inspired by nature, which have received scientific interest. Especially, recent studies on biomimetic microstructures for adhesion functions have shown, including geckos[67], octopus[68], snakes[69], and sunflower pollen grain[70] , etc. (Figure 1.9).

1.8 Octopus-inspired micro sucker structure for adhesion

Obtaining strong adhesion on biological surfaces that are soft, rough, and wet is an important factor for the robots to operate various medical functions.[71-73] Despite their sheer development of adhesives based on biomaterials and chemicals, those adhesives are exposed to several limitations such as the presence of water to lose adhesion, non-invasiveness, and reusability. Therefore, octopus-inspired microstructures are proposed to satisfy the reusability, high adhesion on wet surface, and non-invasiveness.[74-77] The octopus-inspired sucker structure is composed of two different parts which are the outer cup-like structure inspired by the infundibulum of the octopus and the sphere like inner protuberance structure inspired by the acetabulum of the octopus.[68] (Figure 1.10a) When they apply preload into contact with a wet surface, the inner volume of the structure reduces to minimize the amount of liquid inside so that side walls of the sucker-like structure and protuberance-like structure are brought into contact. Consequently, the elastic deformation of those structures renders separation into upper and lower parts to lead to capillary

behavior within them. The upper part is filled with residual liquid located on the bottom. The capillary-induced pressure drops in the lower part results in wet adhesion. (Figure 1.10b) Due to these unique properties of the octopus-inspired structure, they would be useful in a variety of biomedical applications.

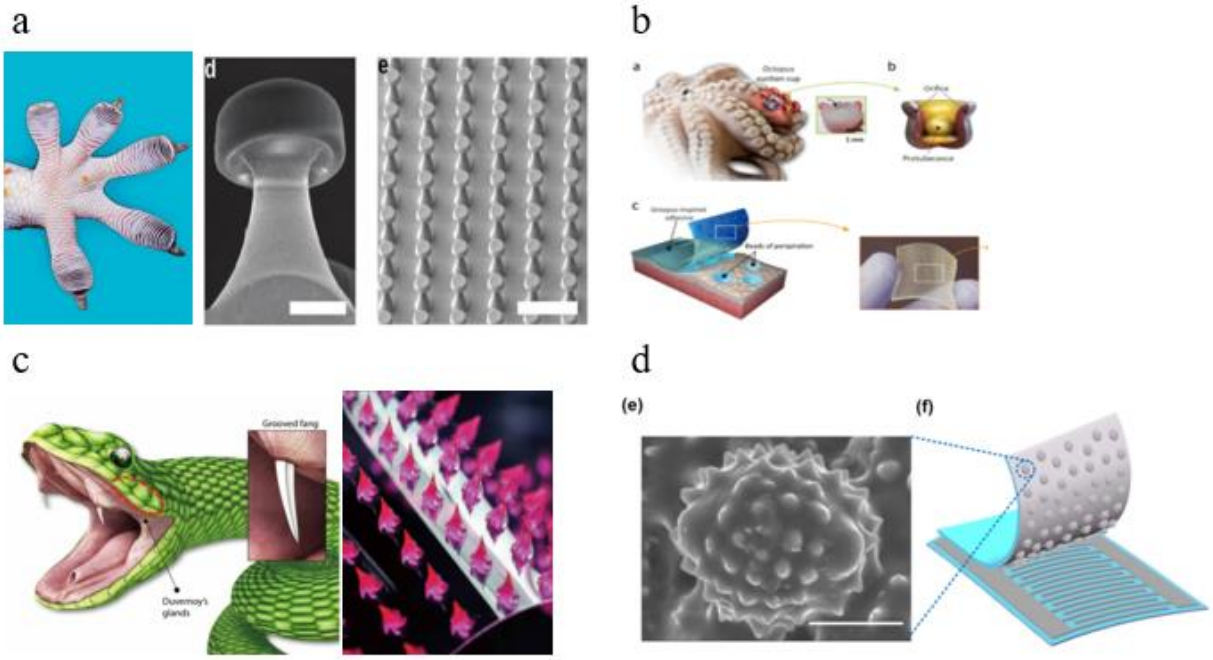

Figure 1.9 Different design of microstructure inspired by nature (a) gecko-inspired microfibers for improvement of dry adhesion performance. Reproduced from reference[67]. (b) Octopus-inspired micro sucker structure for wet adhesive structure. Reproduced from reference [68]. (c) Snake-inspired microneedle for controlled drug delivery. Reproduced from reference [69]. (d) Pressure sensor based on pollen grain-inspired structures. Reproduced from reference [70].

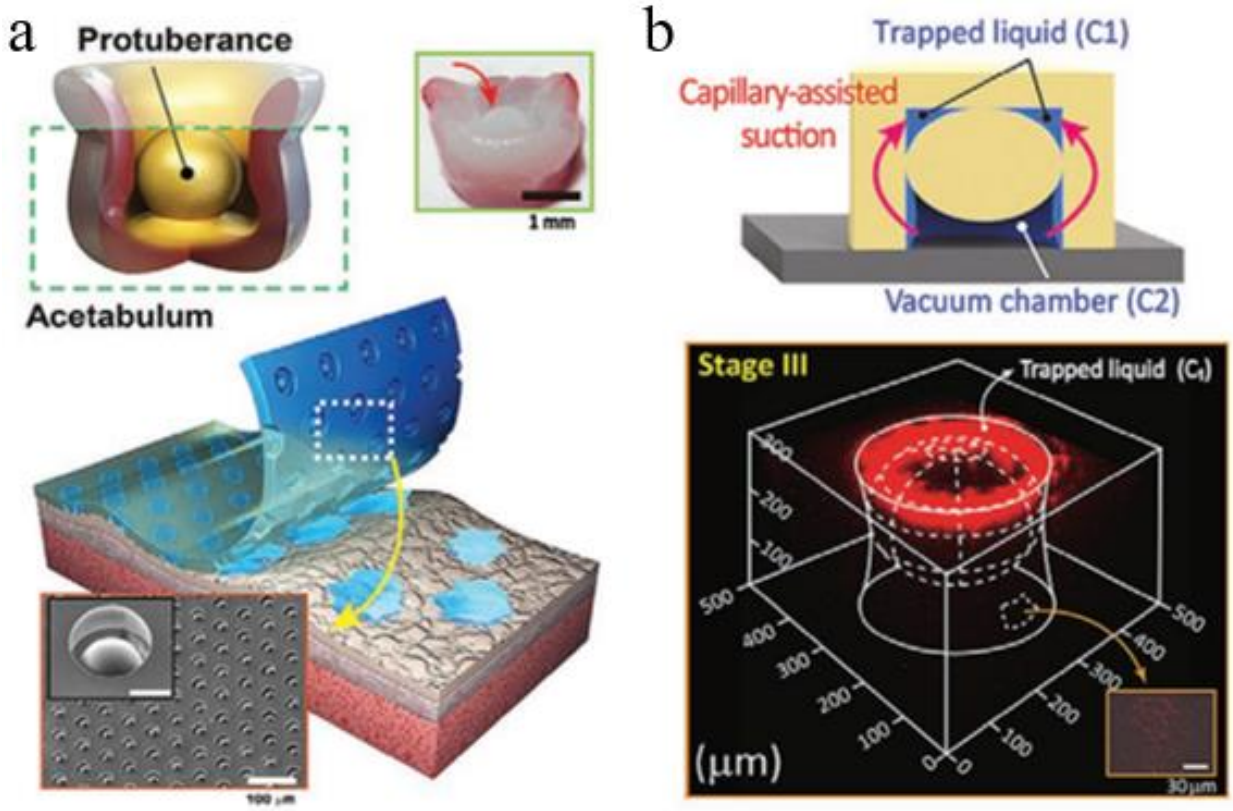

Figure 1.10 Octopus-inspired adhesive structure composed of suction cup structure and the protuberance structure (a) Illustrations of the sucker structure of octopus (top image). Schematic illustration of an octopus-inspired structure attached to a wet surface (bottom image). Inset SEM image of the array of an octopus-inspired structure. Reproduced from reference [68]. b) Adhesion mechanism of the octopus-inspired structure under wet environments (top). Confocal fluorescence image of the trapped residual liquid in the upper structure (bottom). Reproduced from reference [68].

1.9 Pollen grain-inspired spiky structure

On the other hand, nature also provides remarkable examples of microscale biological particles for effective adhesion to a variety of natural surfaces. One of the most important examples of these particles is pollen grain which has unique morphology allowing adhere well to insects or other animals.[78-80] These pollen grain has various size and shape of spiky structures called exine which plays a major role in adhesion to animals and plants.[81] (Figure 1.11 a) In addition, it offers the large inner cavity which is ideal for cargo encapsulation. Therefore, researchers demonstrated various applications including cell recognition[82], drug delivery[83], pressure sensor[70], etc. (Figure 1.11 b-d). Transforming the pollen grain-like structure into microrobots will optimally serve the unique properties of pollen grain for targeted drug delivery application.

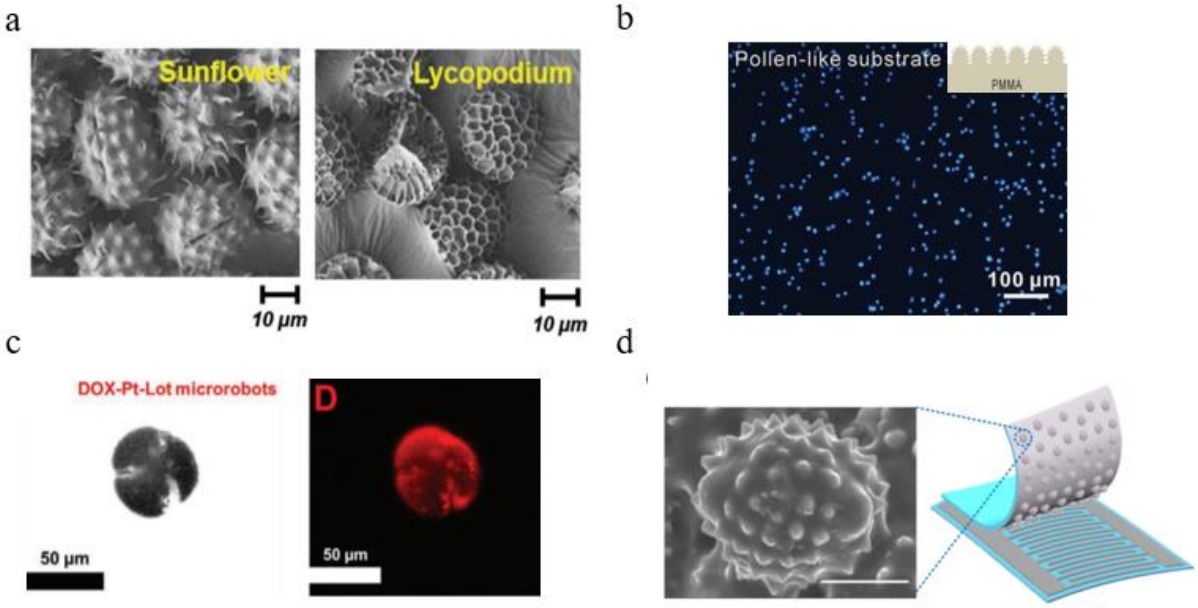

Figure 1.11 (a) SEM image of different species of pollen grain. Reproduced from reference [81]. (b) Efficient and specific recognition to target cancer cell using pollen grain like surface. Reproduced from reference.[82] (c) Drug encapsulation inside the pollen grain. Reproduced from reference [83]. (d) Pressure sensor based on pollen grain like structure. Reproduced from reference [70].

1.10 Methodology

1.10.1 Setup for fabrication of microrobot using 3D laser lithography

To prepare the microrobots in which I used for the experiment, 3D laser lithography is the main approach to obtain the samples throughout this thesis. I focus here on the more technical aspects. A commercial Direct Laser Writing setup (Photonic Professional GT, Nanoscribe GmbH) with a 25X, NA = 0.8 oil immersion objective was used to fabricate all the micro robots in Figure 1.12. Immersion oil is casted on the bottom of the glass substrate for focusing the resist which casted on top of the glass substrate. The system is equipped with femtosecond laser source at a center

wavelength of 780nm. Placement of the x-y-stage includes a motorized coarse positioning stage and a piezo stage for fine positioning. The x-y-stage automatically address writing positions on the substrate. Laser power and galvanometric mirror x- and y-scanning speeds for printing were optimized to obtain 3D geometry sample structure.

1.10.2 Magnetization of the 3D-printed sample

In order to magnetize the 3D-printed microrobot samples demonstrated in this thesis, custom-made microchannel setup was utilized for two-photon-based 3D printing of microrobot (Figure 1.13) Permanent magnets were used to align magnetic nanoparticles inside the prepolymer resist to obtain the optimum magnetic actuation efficiency during the locomotion experiments. The microrobots were fabricated longitudinally perpendicular to the magnetic field.

1.10.3 Sample preparation

In order to prepare the all microrobot samples demonstrated in this thesis, circular glass slides with a thickness of 170 μm were used. The cleaning of all the glass substrates includes ultra-sonication in acetone, isopropyl alcohol, and drying by nitrogen gas flow. Afterward, The photoresist mixture was dropped on a trichloro(1H,1H,2H,2H-perfluorooctyl)silane-treated glass slide for preventing detachment.[84] The printing procedure was performed with a commercial Direct Laser Writing setup (Photonic Professional GT, Nanoscribe GmbH) with a 25X, NA= 0.8 oil immersion objective. Photo-polymerization of the solution in predefined structures was performed. After the printing process, the sample is immersed in isopropyl alcohol for 30 min to remove the uncured photoresist using custom-made syringe pump setup for injecting photoresist. (Figure 1.14) The developed microrobots were immersed in water to store before characterization or use in experiments.

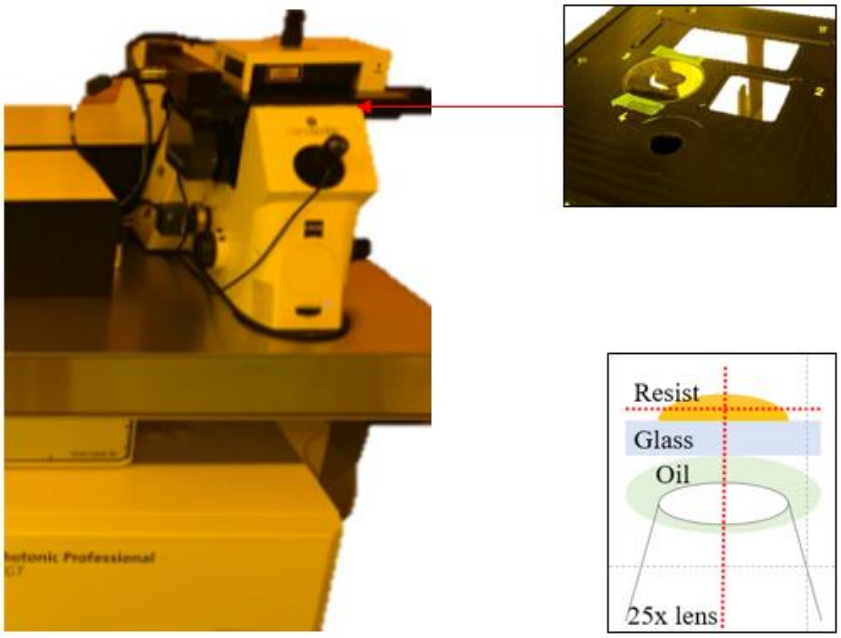

Figure 1.12 Photograph of the direct 3D laser lithography setup for the fabrication of stimuli-responsive microrobots and schematic illustration of conventional writing method for the fabrication.

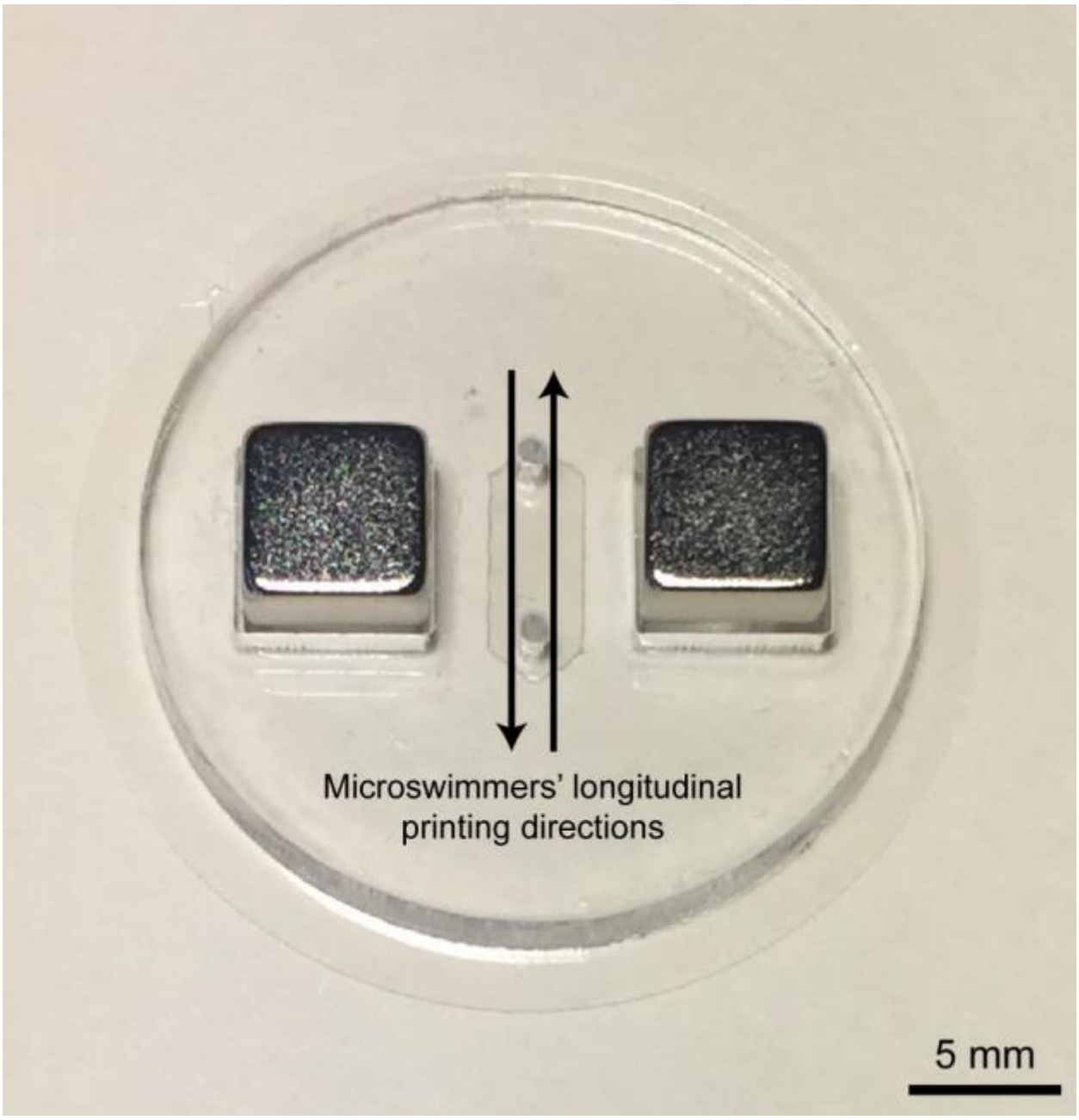

Figure 1.13 Microchannel setup utilized for two-photon polymerization-based 3D-printed microrobots.

Figure 1.14 Photograph of injecting photoresist setup utilized for multi-responsive materials.

1.11 Photoresist compositions

I used both passive and stimuli-responsive photoresists in this thesis. I list all the photo-sensitive materials for fabrication preparation.

1.11.1 PETA photoresist

For preparation of the pentaerythritol triacrylate (PETA), It was mixed by 20 mg of the photoinitiator Irgacure 819 to 980 mg of the pentaerythritol triacrylate (PETA). The mixture was stirred using magnetic bar until the initiator was completely dissolved.

1.11.2 PEGDA photoresist

In order to prepare polyethylene glycol diacrylate (PEG-DA, Mn 575, Sigma), it is mixed with 3% (w/w) of Irgacure 819 (BASF). The mixture was stirred overnight until the photoinitiator was completely dissolved. 20 µL of droplet of the resist was dropped on the cover glass for the 3D laser lithography.

1.11.3 pNIPAM photoresist

The pNIPAM photoresist contains A 3 g of NIPAM monomer, 0.4 g pNIPAM, and 0.2 g BIS were dissolved overnight in 10 mL of ethylene glycol under stirring thoroughly using a magnetic bar (600 rpm). To this pre-mixture solution, 3% (w/w) of the water-soluble photoinitiator lithium phenyl(2,4,6-trimethyl-benzoyl)phosphinate (LAP) was added. The mixture was stirred using a magnetic bar (600 rpm) thoroughly until all the components were mixed thoroughly.

1.11.4 pNIPAM-AAc photoresist

The pNIPAM-AAc solution was synthesized with the following recipe. A 3 g of NIPAM monomer, 0.4 g pNIPAM, and 0.2 g BIS were dissolved for 12 hours in 10 mL of ethylene glycol under stirring using a magnetic bar (500 rpm) at 50 °C. To this mixture solution, 310 µL of AAc (w/w) was added followed by adding 3% (w/w) photoinitiator. The mixture was stirred thoroughly (500 rpm) at 50 °C until all the components were mixed thoroughly.

1.11.5 Synthesis of FePt nanoparticles

FePt nanoparticles were synthesized with the following protocol. 0.2 mmol Pt(acac)2, 0.2 mmol Fe(acac)2, 0.8 mmol CTAC and 0.5 ml oleic acid, were mixed with and 10 ml oleylamine. The mixture was stirred under Argon gas for 1 h at room temperature. Afterward, the solution was heated to 350 ºCat ~5 ºC min-1. The mixture's temperature was kept constant at 350 ºC for 3 hours.

Subsequently, the reaction mixture was cooled down to room temperature. FePt nanoparticles were precipitated by adding ethanol and centrifuged at 8000 rpm for 3 min. The particles were redispersed in hexane and again precipitated in ethanol, followed by centrifugation. This process was repeated at least five times to ensure the removal of the unreacted species and excess surfactants. The particles were then dispersed in hexane for storage and future use.

1.11.6 Imaging setup for stimuli-responsive hydrogel structures

The fabricated stimuli-responsive hydrogels were immersed in the water. To analyze the responsive characteristics of the fabricated hydrogels to changes in temperature, pH, an ion concentration, we acquired time-lapse images using a NIKON Eclipse Ti-E microscope at 10x and 20x magnification in the DIC mode.

1.11.7 Adhesion characterization setup

A custom-built adhesion experiment setup was mounted on an inverted optical microscope (Axio Observer A1, Zeiss) with a video camera (Grasshopper3, Point Gray Research Inc.) for visualizing and recording the contact interface. (Figure 1.15) A high-resolution load cell (GSO-25, Transducer Techniques) was used to measure the force between the sample and substrate. The load cell was built on a computer-aided high-precision piezo motion stage (LPS-65 2″, Physik Instrumente GmbH & Co. KG) moving in the vertical *z* direction, with a resolution of 5 nm and maximum velocity of 10 $mm \cdot s^{-1}$. Another high precision motorized piezo stage (M-605 2DD, Physik Instrumente GmbH & Co. KG) was used in x and y direction with 1-μm resolution and high maximum velocity up to 50 $mm \cdot s^{-1}$. Custom-built software running on Ubuntu Linux is used for moving piezo stages and data acquisition.

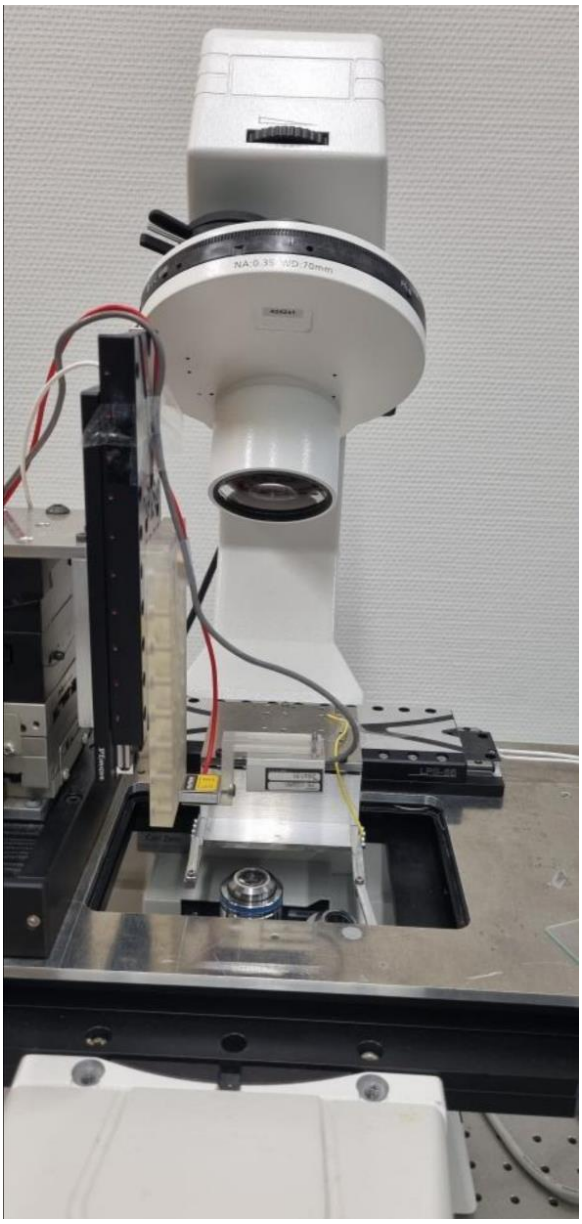

Figure 1.15 Photograph of the custom-built experimental setup for characterization of adhesion and friction force.

1.12 Overview of the Thesis

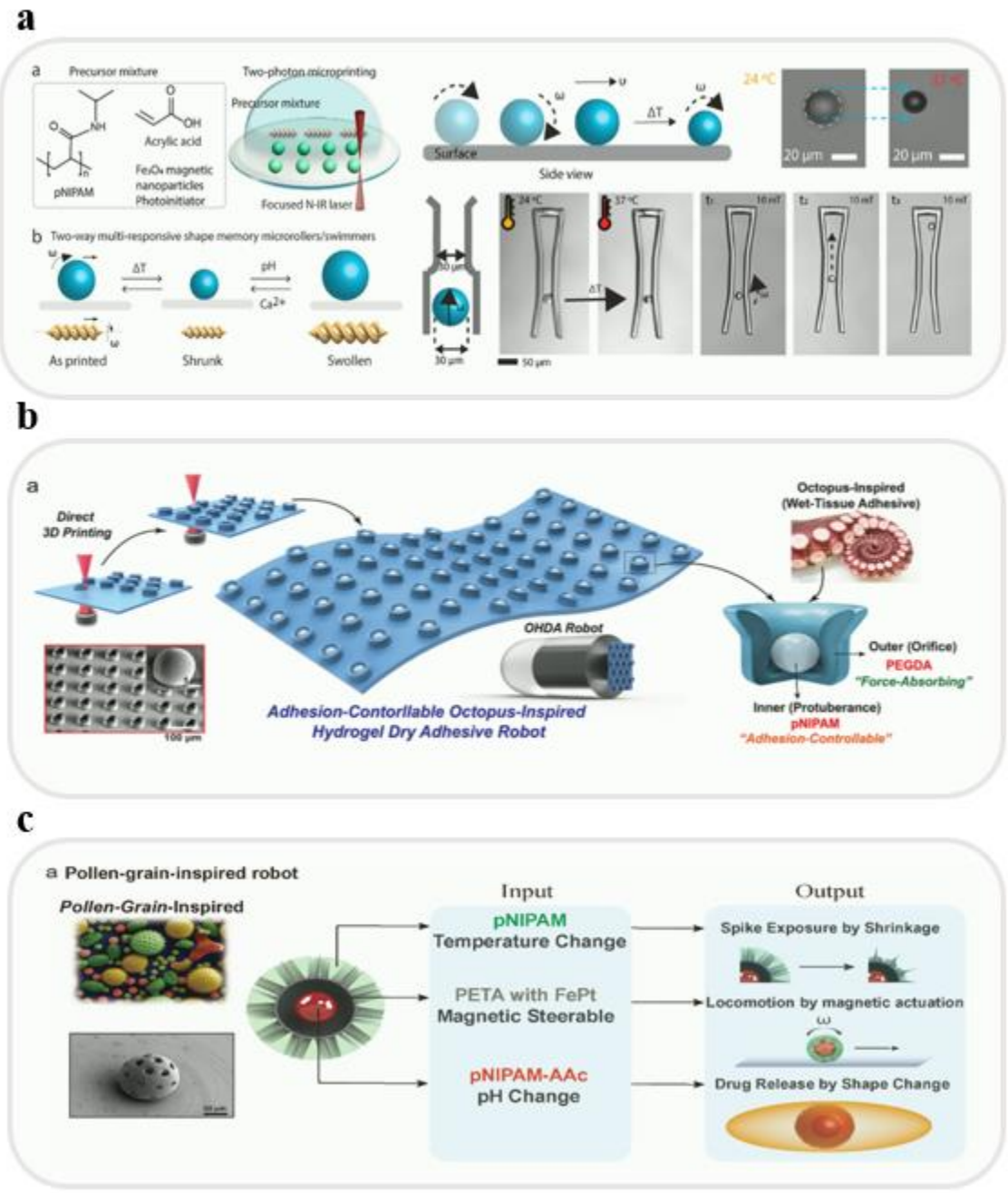

Figure 1.16 Overview of proposed untethered micro-robots combined with stimuli-responsive materials. (a) 3D-printed multi-stimuli-responsive microrobots. (b) Octopus-inspired adhesion-controllable robot. (c) Multifunctional 3D-printed pollen grain-inspired microrobots.

In recent years, the field of microrobots has been developing the promising system for targeted and minimally invasive therapeutic delivery at a hard-to-access human body. Despite the development of active locomotion and control capability of microrobots, a majority of reported microrobots so far have been fabricated from passive backbone materials, which limits functional diversity. In this thesis, I consist of three parts to overcome those problems.

In chapter 2, I present the combination of magnetic actuation with shape-memory materials in the design of independently controlled mobile and multi-functional microrobots. Mobile microrobots can be precisely steered by magnetic fields while at the same time the shape change (swelling and shrinking) is independently controlled by temperature, pH and divalent calcium ions. It is a powerful approach to decouple the control inputs of magnetic propulsion/steering and shape change behaviors. I demonstrate that the shape-change control with multiple inputs (temperature, pH and divalent calcium ions) increase the control versatility where logically controlled patterns can enhance the adaptability of the functional task to various unstructured environments. Mobile micromachines can be steered to penetrate narrow channels (with a diameter of 30 μm). Inside these channels, they can be reversibly swelled to clog the channel. This demonstration can inspire for controlled occlusion of small capillaries in future chemoembolization applications.

In chapter 3, small-scale octopus-inspired temperature-responsive soft robot was explored for controlling wet tissue adhesion in human body, which facilitates medical functions on biological tissues while exploring the target location in a minimally invasive manner. The 3D-printed untethered octopus-inspired hydrogel adhesive (OHA) that exhibits the heterogeneous volume changes of internal mechanical structures in response to temperature stimuli, leads adjusting adhesion strength in a controlled manner. I demonstrate this with a small-scale wireless magnetic medical robot to deliver drug locally with attachment and successful detachment by

remote heating method, which suggests an alternative way to the current medical technology for delivering drug. Introduction of hydrogels with different Young's moduli and temperature responsive behaviours (Polyethylene glycol diacrylate, PEGDA, and poly N-isopropylacrylamide, pNIPAM) were adapted to achieve biocompatible dry adhesion with strong wet adhesion due to octopus-inspired pattern (OP) yet controllable via temperature change. Adjustment of adhesion by controlling the volume in response to temperature which induced by the external alternating magnetic field. Proof-of-the-concept demonstration of magnetically actuated wet-adhesive robot which can reach a desired target position via magnetic guidance and enables controllable adhesion on wet tissue. Our research can inspire future applications of 3D-printed adhesive robot for precisely targeted adhesion on tissues.

In chapter 4, I demonstrate a micro-scale multifunctional pollen-grain-inspired hydrogel robot that could conduct multiple functions in response to independent input stimuli, which enables targeted therapeutic delivery function in complex physiological environments with a minimally invasive approach. The 3D-printed wireless pollen-grain-inspired robot (PHA) with controllable attachment demonstrates the diverse functionalities in response to three different stimuli, which are temperature-responsive controllable attachment, magnetically actuated locomotion, and pH-responsive on-demand drug delivery. I exhibit micro-scale wireless multifunctional robots to deliver a drug in a local region with controllable attachment and on-demand drug delivery, which suggests a novel way to micro-scale robotics for biomedical technology. Integration of three different hydrogels with temperature-responsive, magnetic, and pH-responsive behaviors (pNIPAM, PETA-FePt, and pNIPAM-AAc) facilitating three different actuation capabilities independently, which are locomotion, controllable attachment, and on-demand drug delivery. Controllability of attachment by manipulating the volume of outer crust in response to temperature.

Proof-of-the-concept demonstration for magnetically actuated microrobot, which can steer to reach a targeted biological environment via a customized coil setup. On-demand drug delivery via swelling of spherical hydrogel structure in response to pH change. Our research can inspire future applications of 3D-printed adhesive robots for precisely targeted cargo delivery inside biological environments.

Finally, the last chapter summarizes the results of our work and demonstrates an outlook for 3D laser lithography with stimuli-responsive materials and its potential applications.

1.13 List of Published Papers from this Thesis Work:

Part of this thesis has already been published in peer-reviewed scientific journals. All publication data in Chapters 2, 3 and 4 are reproduced with permission of the publishers.

P1. **Lee, Y. W.**, Ceylan, H., Yasa, I. C., Kilic, U., & Sitti, M. 3D-printed multi-stimuli-responsive mobile micromachines. ***ACS Applied Materials & Interfaces***, *13*, 11, 12759-12766, 2020.

P2. **Lee, Y. W**., Chun, S., Son, D., Hu, X., Schneider, M., & Sitti, M. A Tissue Adhesion-Controllable and Biocompatible Small-Scale Hydrogel Adhesive Robot. ***Advanced Materials***, *34*, 13, 2109325, 2022.

P3. **Lee, Y.W.**, Kim, J.K., Bozuyuk, U., Dogan, N., Khan, M.,Shiva, A., Wild, A., & Sitti, M. Multifunctional 3D-Printed Pollen Grain-Inspired Hydrogel Microrobots for On-Demand Anchoring and Cargo Delivery, ***Advanced Materials***, 2209812, 2022.

Chapter 2. 3D-Printed Multi-Stimuli-Responsive Mobile Micromachines

Reprint from reference.[85]

ACS Appl. Mater. Interfaces 2021, 13, 11, 12759–12766

DOI: 10.1021/acsami.0c18221

2.1 Introduction

Magnetic mobile micromachines have become promising tools that could empower wireless lab-on-a-chip manipulations and minimally invasive targeted therapies by providing spatially precise and temporally on-demand manipulation control in small and hard-to-access spaces.[86-88] To realize such potential, various mobile magnetic micromachines have been proposed for different biomedical applications, such as targeted cargo delivery[37, 89-90], cell manipulation[90-92], and tissue engineering[93] . Despite the sheer progress in the magnetic actuation, locomotion and control capabilities[61-63], a majority of the reported micromachines so far have been made from passive backbone material[64, 67, 92], which limits their functional capabilities. To overcome this limitation and increase the capabilities of the magnetic micromachines to execute multiple tasks that are controlled from independent inputs, integration of stimuli-responsive materials can be a key enabler.

Four-dimensional (4D) printing has recently unleashed a potential for the programming of stimuli-responsive materials that exhibit various size-controlling and shape-morphing behaviors.[94] 4D-printed materials can morph their shape through one-way (irreversible) or two-way (reversible) body deformations under mild and biologically favorable environmental conditions.[95] The mechanism underlying these material deformations entails controlled expansion and contraction of three-dimensional (3D)-printed structures in response to a wide variety of external chemical or physical stimuli, such as magnetic fields[96], temperature[97-98], pH[99], and light[100].

Motivated by the integration of magnetic micromachines with size-controllable soft materials at the smaller length scales, two magnetic milli-swimmer designs were demonstrated by using a thermo-responsive two-way size-controllable polymer in the backbone.[101-102] The

swimmer could adapt its swimming properties to the changes in the environmental temperature. Another very recent untethered magnetic microgripper has exhibited a one-way thermo-responsive size-controllable behavior for a potential single-cell-size biopsy application.[103] Apart from these 2D-to-3D folding material fabrication approaches, to the best of our knowledge, there has been so far no report on the use of 3D-printed untethered multifunctional micromachines made from size-controllable polymers that would enable the execution of new functional capabilities in addition to and independent from its magnetic steering and propulsion control.

Here, we design and 3D print untethered microscrews and microrollers that exhibit one-way and two-way size-controllable behaviors by responding to four different stimuli: magnetic fields, temperature, pH, and calcium ions. We show alternative size-control strategies that may inspire more customized future designs. For example, we show that two-way size-controllable microscrews can reversibly swell and shrink with temperature, pH, and divalent cations for multiple cycles. It is a powerful approach to decouple the control inputs of magnetic propulsion/steering and shape change behaviors, while introducing redundancy in the shape change control by temperature, pH, and divalent cations in logically controlled patterns can enhance the adaptability of the functional task to various unstructured environments. We further show one-way size-controllable microscrews that can swell with temperature up to 65% of its initial length. These microscrews, however, can only be degraded enzymatically for removal, once swollen. Finally, we present a proof-of-the-concept potential of two-way size-controllable microrollers for penetration through narrow channels and their potential for controlled occlusion of small capillaries with 30 μm diameter. Our results can inspire future applications of 3D- and 4D-printed multifunctional microrobots for precisely targeted obstructive interventions and lab/organ-on-a-chip manipulations.

2.2 Materials and Methods

2.2.1 Synthesis of pNIPAM-AAc solution.

To prepare precursor pNIPAM-AAc solution, a 3000 mg of NIPAM monomer (Scientific Polymer Products Inc), 400 mg pNIPAM(Scientific Polymer Products Inc), and 180 mg BIS (Sigma-Aldrich) were dissolved overnight in 10 mL of ethylene glycol under constant stirring (600 rpm) at room temperature. To this solution, 300 µL of solution AAc (w/w) (Sigma-Aldrich) was added followed by 3.5% (w/w) Lithium phenyl-2,4,6-trimethylben zoylphosphinate (LAP, Tokyo Chemical Industry Co. Ltd.) photoinitiator addition. The resultant mixture was stirred again (600 rpm) at room temperature until all the components were dissolved. Then, iron oxide nanoparticles (4.2 mg mL^{-1}) (Cehmicell GmbH, Germany) and the resultant precursor solution were mixed by vortex mixing and ultrasound sonication. The resulting precursors was preserved in yellow light conditions to avoid unnecessary exposure.

2.2.2 Fabrication of the microrollers and microscrews

The prepolymer mixture was dropped on a trichloro(1H,1H,2H,2H-perfluorooctyl)silane-treated glass slide. Printing was performed with a commercial Direct Laser Writing setup (Photonic Professional GT, Nanoscribe GmbH) with a 25X, NA= 0.8 oil immersion objective. Polymerization of the solution in predefines structures was performed in a closed channel, which had two sites to place permanent magnets for the alignment of magnetic particles. After the fabrication, the sample is immersed in isopropyl alcohol for 30 min to remove the uncured precursor. The developed microscrews were placed in water.

2.2.3 Characterization

To analyze the response of the samples to changes in temperature, pH and ion concentration we acquired time-lapse images using a Nikon Eclipse Ti-E microscope at 10X and 20X magnification in the DIC mode. We used 2-(N-morpholino)ethanesulfonic acid (MES) buffer at pH value of 3 and 6 for the pH response experiments.

2.2.4 Magnetic actuation and control of the microscrews and microrollers

Both microscrews and microrollers were actuated and steered using a custom-made Helmholtz five-coiled electromagnetic setup, which can be mounted on an inverted optical Zeiss microscope. (Zeiss Axio Observer A1) The experiments were performed under a 10 mT uniform rotating magnetic field. The step-out frequencies were determined by gradually increasing the frequency of rotating magnetic field from 0.5 to 2 Hz. For the mobility characterizations, an in-house particle tracking software developed in MATLAB (MathWorks, Natick, MA) was used.

2.3 Results

2.3.1 3D printing of size-controllable microrollers and microscrews using external stimuli

We selected microroller[104] and helical microscrew[105] models as two representative designs for the proof-of-concept demonstration of the multi stimuli-responsive magnetic micromachines. We 3D-printed these designs from one-way and two-way shape memory polymers that respond differently to external stimuli **(Figure 2.1a).**

For two-way shape memory effect, we formulated a magnetic and thermo-responsive precursor mixture by utilizing poly N-isopropylacrylamide (pNIPAM) as shown on **Figure 2.1b**. Hydrogels of pNIPAM typically exhibit low critical solution temperature (LCST) behavior.[106] Below its LCST, the polymer chains of pNIPAM are hydrophilic and form hydrogen bonds with water molecules when immersed in aqueous solution. Hence, the hydrogel network of pNIPAM expands with the water absorption below its LCST. As temperature increases above the LCST, the polymer chains of pNIPAM undergoes a transition that result in expulsion of water out of its network and shrinkage. To date, microactuators with complex 3D geometries and from various polymeric materials, such as N-isopropylacrylamide, acrylic acid, β-cyclodextrin acrylamide (βCD-AAm) and adamantane acrylamide (Ad-AAm), have been reported.[24, 65, 107]

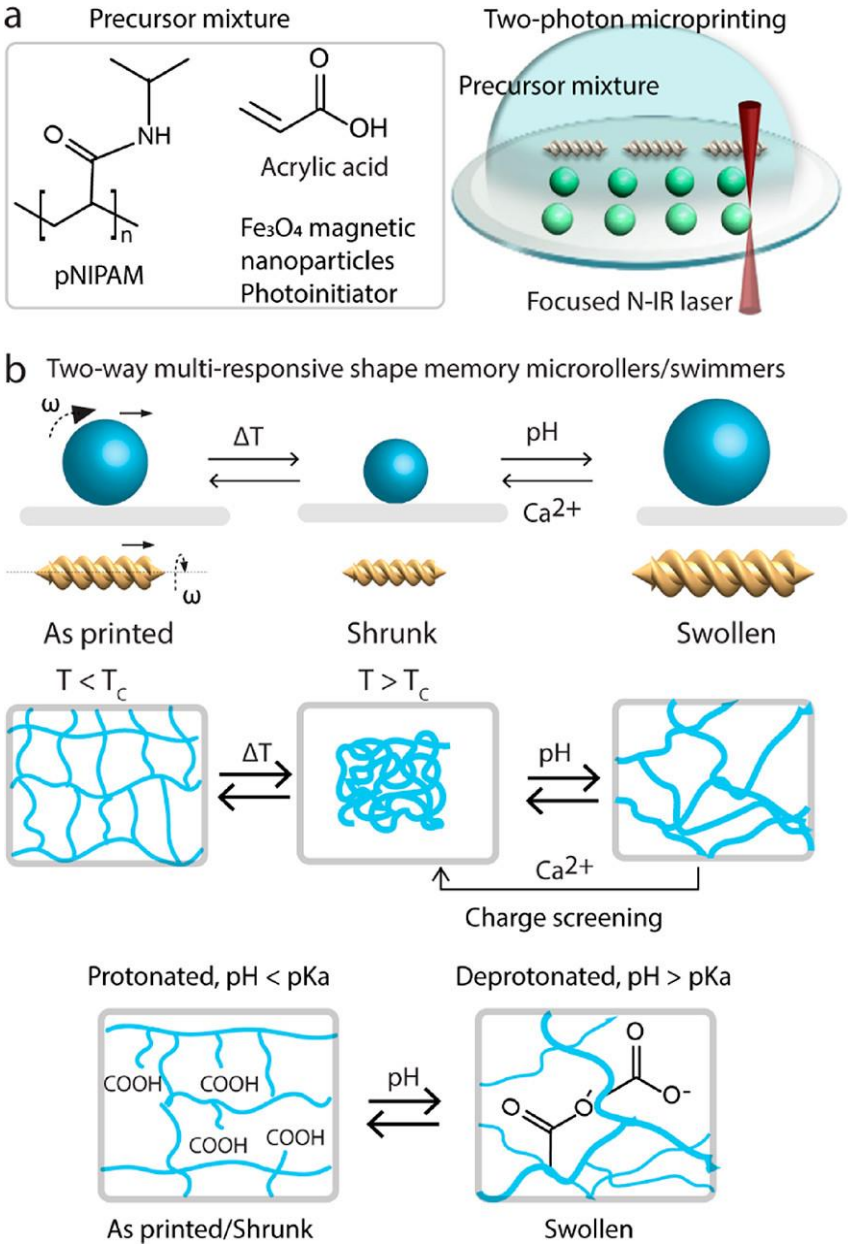

Figure 2.1 Schematic illustration of 4D printing of size-controllable microrollers and microscrews using external stimuli. (a) Schematic illustration of the components of stimuli-responsive material-based photoresists and printing process using a direct laser writing (two-photon polymerization) system. (b) Schematic representation of the two-way size-controllable microrollers/microscrews mechanism when induced by multiple stimuli, such as temperature, pH, and Ca2+ ions.In addition to thermo-responsiveness, we introduced pH and ion responsiveness by formulating the precursor

mixture N-isopropylacrylamide with acrylic acid (pNIPAM-AAc) in the form of a co-polymer. Carboxylic acid groups on the acrylic acid can respond to pH and the presence of divalent ions due to the transition in its protonated/deprotonated states and charge screening, respectively. Upon exposure to an aqueous solution with a pH value above its acidity constant (pKa), -COOH group on the polymer chains deprotonates and creates the negatively charged $-COO^-$ group. The negatively charged molecular chains absorb more water, driving a significant expansion of the network size. Reversely, the carboxylate groups will be protonated when the pH value is lower than its pKa, driving off the water molecules and hence shrunk network size. We also sought to control the swelling properties with charge screening, depending on the presence or absence of Ca^{2+} ions in solution. When the hydrogel is exposed to divalent Ca^{2+} ions, the carboxylate groups are screened via by means of Ca^{2+} ions. On the contrary, removing Ca^{2+} ions within the network leads to swelling of the micromachines.

For 3D printing, we fabricated microrollers and microscrews using two-photon-polymerization-based 3D printing. Briefly, the interaction of focused femtosecond laser irradiation with the photoinitiator in a tight focal volume, called voxel, results in the initiation of a free-radical polymerization with the electrons of pi bonds within the precursor monomers. Computer controlled scanning of the laser within the bulk volume of the precursor mixture solution thus facilitates the formation of complex 3D microstructures with submicron (as low as 100 nm) features.[108-111]

2.3.2 Temperature responsiveness of two-way size-controllable spherical microrollers and double-helical microscrews

In order to realize a fully reversible two-way response with the microrollers and microscrews, a photo-curable resin containing pNIPAM-AAc was prepared. We first optimized the fabrication process by applying different laser doses for the maximized structural fidelity of microscrews in three different dimensions. Figure 2.2a demonstrates the 3D-printed illustrations of microrollers with different laser powers. Between 15 mW and 35 mW with 20×10^3 μms^{-1} scanning speed, it shows acceptable dose and the structural fidelity of the printed microrollers was in agreement with the design.

In order to investigate the reversible swelling and shrinking characteristics of the pNIPAM-AAc-based spherical microrollers, fabricated microrollers were immersed in water at room temperature and the temperature was then elevated to 37°C as shown in Figure 2.2b. When the temperature is only slightly over the LCST of pNIPAM (around 32 °C), the hydrogel microrollers exhibited de-swelling behavior due to the hydrophilic-to-hydrophobic phase change. The body length of the microrollers was changed 34% of their original length when they were exposed to the temperature change. Upon cooling the microrollers back to the room temperature, the structures became hydrophilic again and restored to their initial state by swelling with water. In addition, to investigate the effect if the crosslinking density on the temperature-responsive behavior of pNIPAM microrollers, we utilized different laser parameters during printing process of the microrollers and observed the change in their swelling characteristics. We defined a swelling rate of microrollers as the ratio of the length change to the initial length as

$$\varepsilon(\%) = -\frac{l_0 - l}{l_0} \times 100. \quad (2)$$

where l and l_0 are the length of the expanded and original microrollers, respectively. Figure 2.2c demonstrates how the printing laser parameters change the swelling property of the microrollers in response to temperature. As laser power increases from 10 mW to 50 mW, the shrinkage rate decreases by 20%. This result indicates the effect of the crosslinking density of the printed microrollers on their swelling kinetics. Slower scanning speed and higher laser power provided the higher crosslinking density of the material, which limits the swelling performance of the pNIPAM-AAC microrollers. The swelling and shrinkage of microrollers were performed multiple times by sequential heating and cooling cycles without observing any plastic deformation on the structures (Figure 2.2d).

In addition to microrollers, we also demonstrated the printing of our previous double-helical geometry[37], which is more complex in shape compared to microrollers. Such microscrews design aims to maximize the volume of the body for potential high-volume cargo delivery applications. Figure 2.2e demonstrates that we were able to print different size (36, 48, 60 μm body length) of helical microscrews from stimuli-responsive material formulation. The structural fidelity of the resulting microscrews was in agreement with the proposed computer-aided design. In order to study the temperature responsiveness of the resulting pNIPAM-based microscrews, the temperature was raised to 37°C which is above the phase volume transition, the fabricated microscrews exhibited length shrinkage by 30% (Figure 2.2e). At low temperatures, they showed swelling back to their initial length. We also investigated the robustness of the structures and reversibility of the length change by performing multiple cycles of heating and cooling (Figure 2.2f). Similar to the spherical microrollers, we were able to demonstrate multiple cycles of swelling and deswelling without any noticeable damage in the double-helical microscrews shape.

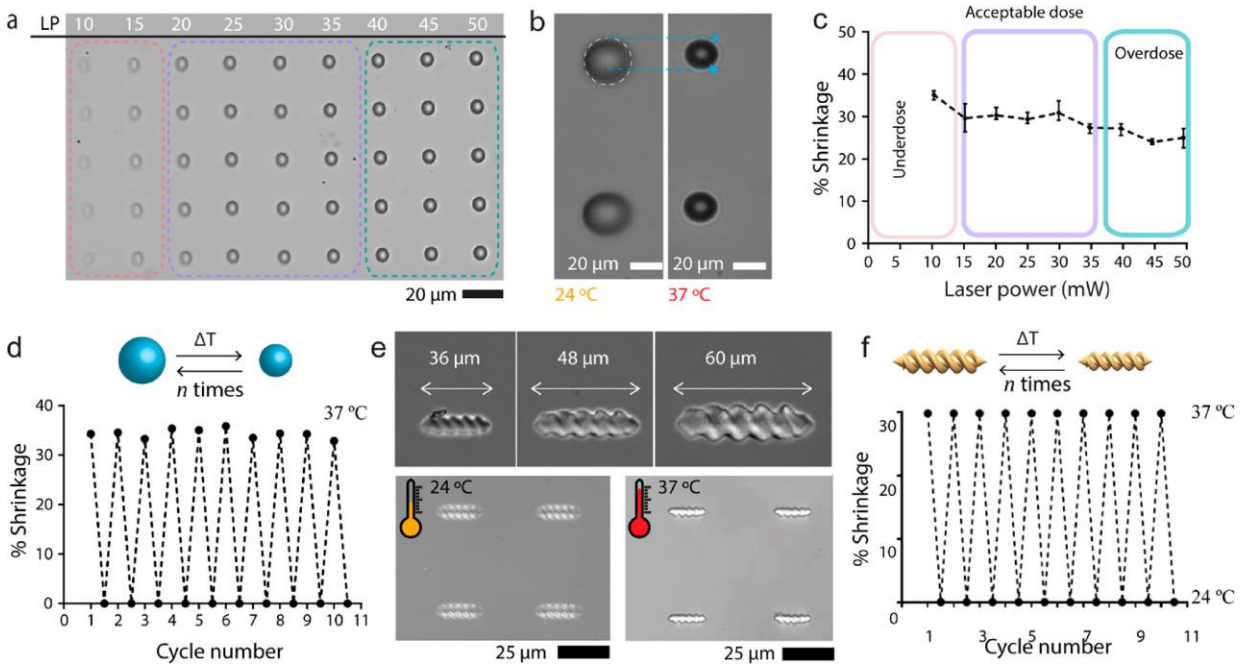

Figure 2.2 Temperature responsiveness of two-way size-controllable spherical microrollers and double-helical microscrews. (a) Optical microscopy images of the 3D-printed pNIPAM-AAc microrollers (the unit of laser power (LP) is mW). (b) Optical microscopy images of shrinkage of the microrollers in response to change in temperature. (c) Plot showing the relationship between the laser power for printing the material and resulting shrinkage properties due to the change in the cross-linking density. Different laser powers ranging from 0 to 50 mW were exposed to microrollers composed of pNIPAM-AAc. (d) The repetition test of the pNIPAM-AAc microrollers shrinking/deshrinking cycles without any deterioration. (e) Optical microscopy images of three different microscrews printed in different sizes and representative swelling/deswelling of a 4 × 4 microscrews array in response to temperature change. (f) Repetition test of the pNIPAM-AAc microscrews during temperature-dependent shrinking/deshrinking cycles.

2.3.3 pH and ion responsiveness of two-way size-controllable microrobot

Concerning the pH-responsive characteristics of the pNIPAM-AAc hydrogels, microrollers and microscrews were printed and initially placed in water (Figure 2.3a). Due to a large number of carboxy groups in the polymer chain, we expect to observe the deprotonation of carboxylic acid groups and electrostatic repulsion between the ionized chains which leads to a significant expansion of the network by absorbing water upon treatment with high pH solutions. Therefore, the addition of ammonia solution with a pH value of 11 led to the expansion of the microrollers and microscrews up to 40% in body length. The response of the microstructures was within seconds because of the fast diffusion rate of ions. On the contrary, by dropping inside a low pH solution, the microroller and microscrews lengths shrunk rapidly by 22% with the protonation of carboxylic acid groups. The swelling and shrinking process were fully reversible and can be repeated many times as shown in Figure 2.3b.

We also investigated the ion-responsive properties of the pNIPAM-AAc hydrogels. Upon adding a chemical such as ethylenediaminetetraacetic acid (EDTA) into the hydrogels in water, their size became expanded since it contains carboxyl groups in the hydrogel. The carboxylic groups in acrylic acid (AAc) can release protons and thus be ionized. The repulsive forces of carboxylate ions repel other molecular chains to expand size of hydrogel. When exposed to Ca^{2+} solutions, the carboxyl groups accept protons and thus be deionized and shrunk their structure. The swelling and shrinking process were fully reversible and can be repeated for multiple cycles. By dropping a sufficient amount of EDTA solution, the structures could swell up quickly to 140% of its size, and the whole process completed in a few seconds. When $CaCl_2$ solution was injected, the original state is recovered within seconds. In order to achieve a high swelling/deswelling ratio, we

adopted multi-responsiveness to temperature and Ca^{2+} ions as shown in Figure 2.3c. By exploiting this synergistic property, single hydrogel can be actuated to have capability of responsive direction which they can shrink in response to heat and swell in response to Ca^{2+} ions. The body length of the microscrews was changed 36% of their original length in response to temperature and they became swollen up to 80% of their length compared to the shrunk state of the microscrews. In addition, to confirm the reversibility of the actuation process, we conducted the same process 10 times and there was no deterioration as shown in Figure 2.3d.

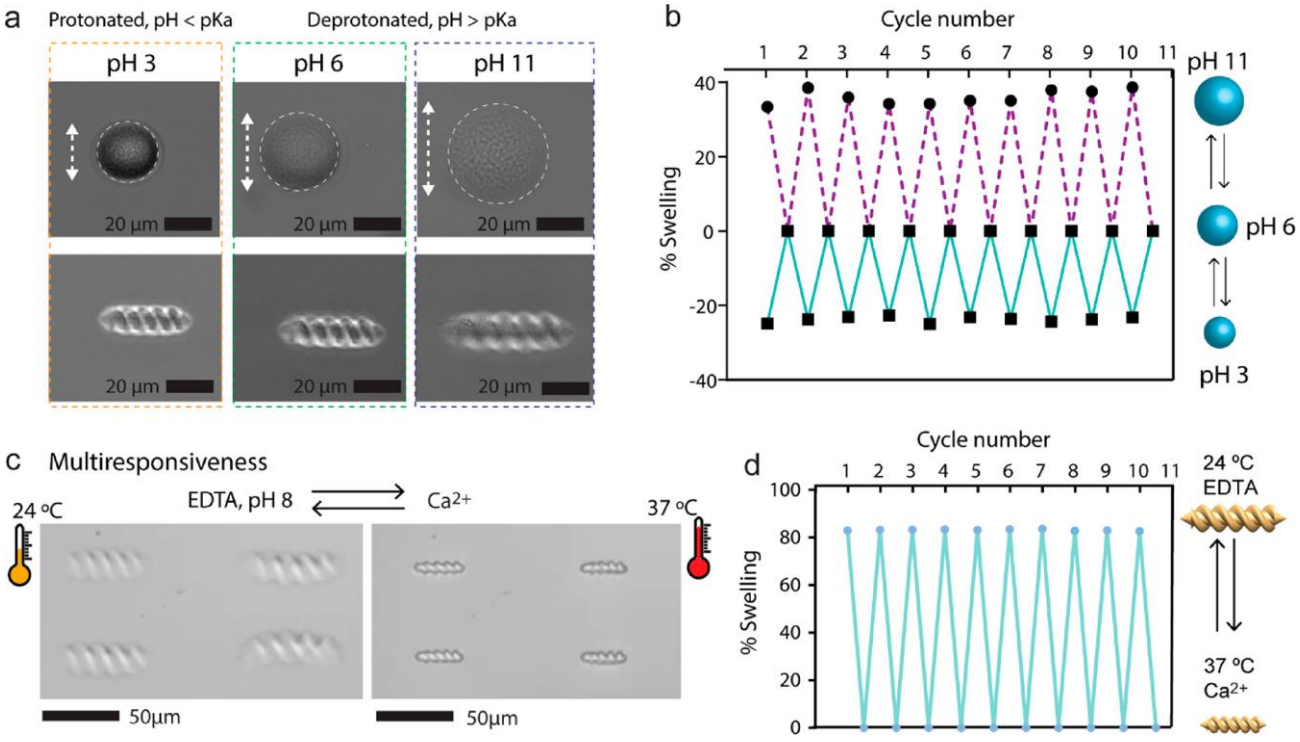

Figure 2.3 pH and ion responsiveness of two-way size-controllable microrollers and microscrews. (a) Optical images of swelling/deswelling microrollers and microscrews in response to pH value. (b) The repetition test of the pNIPAM-AAc microrollers swelling cycles in response to pH. (c) Optical images of multiresponsiveness of microscrews in response to temperature and Ca2+ ion

concentration change. (d) Repetition test of the pNIPAM-AAc microscrews shrinking/swelling cycles in response to temperature and Ca2+ ion change.

2.3.4 Temperature responsiveness of one-way size-controllable double-helical microrobot

We previously introduced gelatin-based magnetic nanocomposites as two-photon-based 3D printable and biodegradable materials. In order to further study one-way size-controllable polymer, we utilized this material due to its inherent temperature-responsive behavior as shown on Figure 2.4a. Gelatin, derived from the hydrolysis of collagen is a temperature-sensitive material. Its crosslinked form exhibits swelling behavior in response to an increase in temperature and its network is enzymatically degradable.[112] To investigate the one-way size-controllable behavior of gelatin-based microscrews, we microscopically monitored the shape transformation by increasing the room temperature, where microscrews were in their printed size, to 37 °C. We observed the swelling of the microscrews body by 23.4% upon increasing temperature to 37 °C (Figure 2.4b). Also, the diameter of 24 μm length microscrews increased to 9.7 ± 0.7 μm from 6.6 ± 0.4 μm in 4 hours (Figure 2.4c). In order to study the size-dependence of gelatin-based microscrews swelling, we 3D printed the microscrews in different dimensions (24, 48, and 72 μm length) and increased the temperature to 37 °C. From the study, we observed that increasing the dimensions of the microscrews resulted in decreased overall swelling degree as shown in Figure 2.4d. Further, we investigated the impact of the laser power on the swelling property of the one-way size-controllable microscrews in response to temperature as shown in Figure 2.4e. As the laser power increased from 22.5 to 25 mW, the swelling rate followed a sharp increase due to the formation of new network chains to absorb additional water. After reaching the optimal crosslinking density at

25 mW, over-crosslinking resulted in another sharp drop in the swelling. High degree of crosslinking led to decrease in the pore size of the gelatin, so that water molecules are expelled.

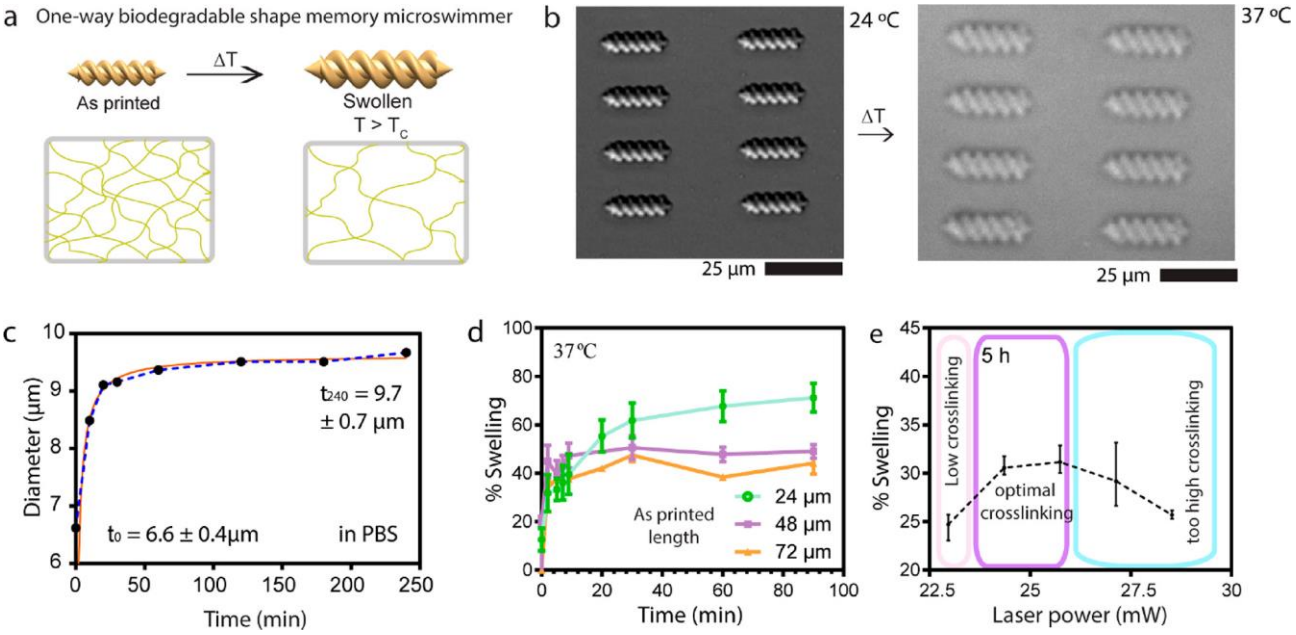

Figure 2.4 Temperature responsiveness of one-way size-controllable double-helical microscrews. (a) Schematic representation of one-way size-control mechanism by temperature change. (b) Optical microscopy images of gelatin-based microscrews swelling in response to temperature change. (c) Swelling kinetics of gelatin-based microscrews in PBS. (d) Swelling kinetics of different sizes of gelatin microscrews in response to temperature. (e) Effect of the laser power on the cross-linking and swelling of gelatin-based microscrews.

2.3.5 Magnetic actuation and steering demonstrations of the microrobot

As shown in Figure 2.5a, we present the magnetically steerable 3D-printed microroller. For the mobility of the micromachines, we encapsulated superparamagnetic iron oxide nanoparticles (SPIONs) inside the pNIPAM-AAc. The total amount of SPIONs loaded in the mesh network of the micromachine body is crucial for their swelling ratio. Increasing the amount would result in a lower shrinking ratio. Increased volume fraction of SPIONs from 0 to 0.33 shrunk from 36% to 27%. Over 0.33 of volume fraction, 3D printing was not possible, likely due to the reduced degree of percolation of the crosslinked network.[113] Introduction of SPIONs could induce steric hindrances inside the pNIPAM polymer network, which changes their swelling kinetics. For magnetic mobilization, we utilized a custom five-coil electromagnetic setup to create rotating uniform magnetic fields that rotate/propel and steer microrollers and microscrews along designated trajectories (Figure 2.5b and d). We characterized the frequency-dependent behavior of the microrollers and microscrews loaded with 4.2 mg mL^{-1} SPIONs at 10 mT. As increasing the input frequency starting from 0.5 to 2 Hz, the speed of the microroller increased up to 1.96 μm s^{-1} and optimally controlled microrollers at 1.5 Hz (Figure 2.5c). Additionally, we characterized the speed of microroller in response to temperature. Speed of microller decreased as temperature increase to 37 °C. We also investigated the step-out frequency of the microscrews by gradually increasing the frequency of the applied rotating magnetic field from 0.5 Hz to 1 Hz. It was demonstrated that the fabricated microrollers were actuated and steered optimally at 0.8 Hz under a 10 mT rotating magnetic field (Figure 2.5e). The velocity of the microscrews at optimum actuation frequency was measured to be 2.7 μm s^{-1}.

To further test the spatial adaptability and motion capability of stimuli-responsive microrollers, we prepared a microfluidic channel with the same body length of initial microrollers (30-μm channel diameter), so that the microrollers could not pass through the channel unless they changed their size. We steered the microrollers to the beginning of the channel and changed the temperature to induce temperature-dependent shrinkage. After microrollers shrunk to the size smaller than 30 μm, they could pass through the channel. Then, we actuated the microrollers with a frequency of 2 Hz to steer them within the channels in a controlled manner (Figure 2.5f). Such capability can inspire to use this method for controlled chemoembolization of tumor tissues at distal arteries and arterioles. Currently, embolization methods are available only for large arteries by using passive particles. This limits the potential of clinically used embolization methods to target tumors in a more precise and the method also damages healthy organ sites. Our method has the potential to leverage the capability of the chemoembolization by specifically reaching out to smaller vessels in a steerable way. The swollen-state microrollers can be moved through the cannels, and as the channel size narrows down, the externally heated shrinking microllers can go further in until it efficiently clogs the vessel at a distal location. The shrinkage can also be accompanied with the release of chemotherapeutics that can be sequestered within the hydrogel body of the microrollers. Both 1-way and 2-way micromachines are alternative design strategies that can provide unique advantageous depending on the context. 2-way shape-memory micromachines can reversibly go through smaller channels. However, these are not biodegradable, therefore, in cases where shrinking the size might be needed without an environmental stimulus, it might be difficult to retrieve them. 1-way shape memory irreversible micromachines can swell and clog the channels that are bigger than their size. These micromachines are biodegradable, so they can be dissolved in the case of emergency. While 2-way reversible micromachines can go

through smaller channels, 1-way irreversible micromachines can clog the channels that are bigger than their size. Additionally, 1-way micromachines are biodegradable, so they can be remodeled later in a realistic in vivo environment. While this is the end goal, there are still a number of challenges that need to be addressed in the future.

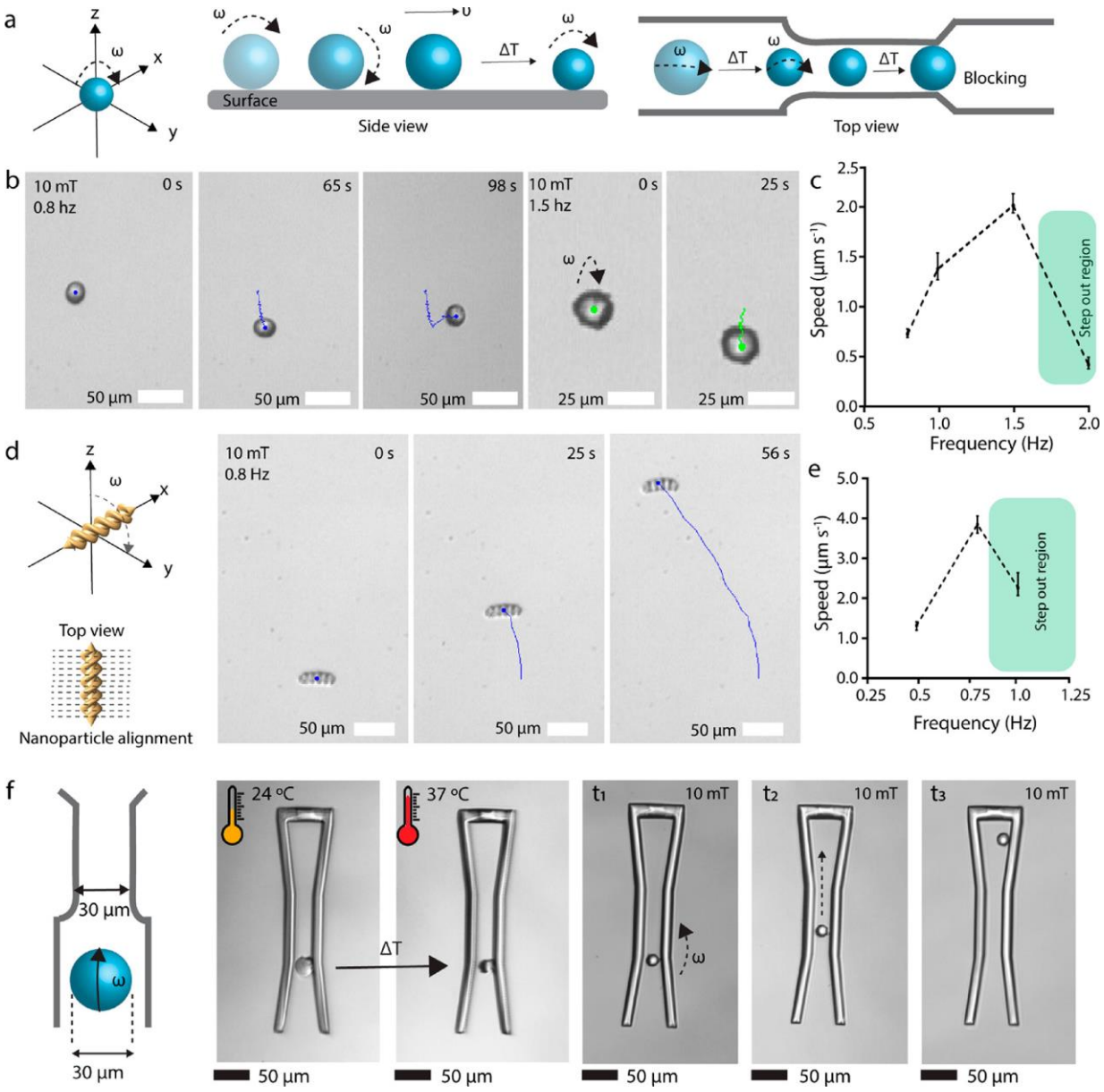

Figure 2.5 Actuation and steering demonstrations of the microrollers and microscrews using a rotating magnetic field, and demonstration of their spatial adaptability by their temperature-dependent size control. (a) Schematic illustration of magnetic actuation and steering of the microrollers. (b) Controlled surface rolling trajectory snapshots (blue lines) of a microroller at a 10 mT rotating magnetic field at 0.8 and 1.5 Hz on a smooth glass substrate inside deionized water. (c) Mean motion speed of the microrollers as a function of magnetic rotation frequency. (d)

Magnetic steering control snapshots of the double-helical microscrews at 10 mT rotating magnetic field at 0.8 Hz. (e) Mean speed of microscrews with different rotation frequencies. (f) Schematic diagram and optical images of the microroller showing the spatial adaptability (shrinkage) by temperature control to pass through a channel smaller than its initial diameter.

2.4 Summary

We present the combination of magnetically steerable 3D-printed microroller and microscrews designs with stimuli-responsive hydrogel materials to develop size-controllable micromachines. These wirelessly controlled micromachines gained the ability to respond to multiple stimuli, including magnetic fields, temperature, pH, and cations. We show the multi-responsive behavior as a powerful approach to decouple the control inputs of magnetic propulsion/steering and shape change behaviors and to introduce redundancy in the shape change control by temperature, pH, and divalent cations in logically controlled patterns, which can enhance the adaptability of the micromachines to various unstructured environments. While 2-way reversible micromachines can go through smaller channels, 1-way irreversible micromachines can clog the channels that are bigger than their size. Additionally, we introduced gelatin-based magnetic nanocomposites as 3D printable and biodegradable materials with temperature-responsive properties. They observed a 23.4% increase in microscrew size when heated to 37°C, and larger microscrews had lower overall swelling. Laser power influenced swelling, with higher power initially increasing it until an optimal crosslinking density was reached. Our results can inspire future applications of 3D- and 4D-printed multifunctional microrobots for precisely targeted obstructive interventions and lab/organ-on-a-chip manipulations.

Chapter 3. A Tissue-Adhesion-Controllable and Biocompatible Small-scale Hydrogel Adhesive Robot

Reprint from reference.[85]

Adv. Mater. 2022 34, 13, 2109325

DOI: 10.1002/adma.202109325

3.1 Introduction

Small-scale wireless medical robots have been recently proposed to carry out a targeted and minimally invasive drug delivery and treatment of diseases in the given local site of the body, without a surgical operation[32, 87, 114-119], which would have a disruptive positive impact on healthcare. They can navigate within the body in a controlled way using medical imaging feedback, and conduct medical tasks, such a drug delivery, hyperthermia and embolization, at the target location. [120-121] Recently, also soft-bodied wireless medical robots have become possible, where soft body enables programmable shape change, multifunctionality and reconfiguration and safe operation inside the body.[32, 85, 122-124] Efforts have been made to development and implement such robots, including fabrication of microscale soft robotic devices, and synthesis of biocompatible or biodegradable materials and strategies for locomotion inside the body. [60, 88, 92, 125] However, applying these approaches have many limitations to operate safely and robustly in such complicated environments.

Among various limitations, achieving strong adhesion to biological tissues whose surfaces are soft, rough, and wet is critical for the robots to efficiently implement various biomedical functions, including collecting bio-signals, bonding with unwanted derivatives and destroying them, healing wounds, and applying electrical impulses to nerves. [103, 126-128] Although there are already commercial adhesives for tissues, the lack of long-term durability causes the failure of adhesion on the tissue.[129-130] Tough adhesives made of double-layered hydrogels[131] and dry double-sided tapes[132] were recently suggested for biological adhesives. These tissue adhesives are capable of strong adhesion to wet tissues, it is very difficult to detach them, indicating that surgical operation is required for the detachment process. In addition, uncontrolled detachment can cause not only a problem of leaving an undesirable residue in the body but also damage to the

tissue.[133-136] On top of that, implementing the controllable adhesion and deadhesion functions on a small medical robot is extremely challenging due to the limited space to embed a mechanism to regulate the adhesion. It would be very effective to achieve adhesion-controllable small-scale robots using the combination of suitable materials and structures.

Here, we propose a small-scale robot that has controlled wet tissue adhesion in the body, which enables the robot to perform biomedical functions on tissues at the target location with remote magnetic actuation. Hydrogels of different Young's modulus were adapted for biocompatible and strong wet suction-based adhesion due to octopus-inspired pattern (OP), in which the outer wall made of high-modulus polyethylene glycol diacrylate (PEGDA) structure prevents hydrogel-based OP from fully collapsing during the suction, while the inner protuberance structure made of temperature-responsive volume-changeable low-modulus poly N-isopropylacrylamide (pNIPAM) supports the outer wall from inside. By modulating the volume of the inner pNIPAM with the heat transferred from the remotely heated adjacent magnet, the adhesion is controllable. We demonstrate the wet-adhesive robot approaches the target by remotely actuated magnetic guidance and subsequently performs controllable adhesion on the wet tissue ex vivo, to be able to implement local biomedical functions.

3.2 Materials and methods

3.2.1 Synthesis of pNIPAM and PEGDA hydrogels

pNIPAM-AAc (Scientific Polymer Products Inc.) solution was synthesized with the following recipe. A 3 g of NIPAM monomer (Scientific Polymer Products Inc.), 0.4 g pNIPAM, and 0.2 g BIS (Sigama-Aldrich) were dissolved 12 hours in 10 mL of ethylene glycol under stirring using

magnetic bar (500 rpm) at 50 °C. To this mixture solution, 310 µL of AAc (Sigma-Aldrich) (w/w) was added followed by adding of 3% (w/w) Lithium phenyl-2,4,6-trimethylben zoylphosphinate (LAP, Tokyo Chemical Industry Co. Ltd.) photoinitiator. The mixture was stirred throughly (500 rpm) at 50 °C until all the components were mixed thoroughly. In order to prepare polyethylene glycol diacrylate (PEG-DA, Mn 575, Sigma), it is mixed with 3% (w/w) of Irgacure 819 (BASF). [137]

3.2.2 Fabrication of the octopus-inspired patterns

The cleaning of glass substrate includes ultra-sonication in acetone, and isopropyl alcohol, and drying by nitrogen gas flow. The PEGDA precursor mixture solution was dropped on a trichloro(1H,1H,2H,2H-perfluorooctyl)silane-modified glass substrate for fabricating sucker structure. A commercial Direct Laser Writing setup (Photonic Professional GT, Nanoscribe GmbH) with a 25X, NA= 0.8 oil immersion objective was used for the printing the octopus-inspired patterns. Laser power and galvanometric mirror x- and y-scanning speeds were optimized for printing at 40mW and 50,000 µm/s, respectively. After the 1st step printing, the sucker structures are developed with isopropyl alcohol for 20 min to remove the residue of PEGDA. Then, pNIPAM-AAc prepolymer mixture droplet was dropped on the structure. Laser power and galvanometric mirror x- and y-scanning speeds were optimized for printing at 32.5mW and 20,000 µm/s, respectively. The development was performed using isopropyl alcohol for 20 mins to have fine development. The geometry of octopus includes sphere like protuberance inside the sucker structure, The diameter and height of sucker is 44 µm and 32 µm, respectively. The whole pattern composed of 10 × 10 structures in an array with a width of 880 µm.

3.2.3 Adhesion measurement setup

The custom-made adhesion setup was built on an inverted optical microscope (Axio Observer A1, Carl Zeiss AG, Oberkochen, Germany) assembled with a video setup (Grasshopper 3, FLIR Systems Inc., Wilsonville, OR, USA) for visualizing the contact interface. A load cell (GSO-25, Transducer Techniques LLC, Temecula, CA, USA) built on a computer controlled motorized piezo stage (LPS-65 2", Physik Instrumente GmbH & Co. KG, Karlsruhe, Germany) moving in the z-axis direction with 5 nm resolution was used for recording the adhesion forces. Y-direction is controlled by another high precision motorized piezo stage. x- and y-direction are adjusted by a manual *xy*-stage and tilting adjustment was made by two goniometers. Movement of the piezo stages and data acquisition were done by custom software running on Ubuntu Linux. The load cell was connected to the computer using a signal conditioner (BNC-2110, National Instruments, Austin, TX, USA) and a data acquisition board (PCLe-6259, National Instruments, Austin, TX, USA).

3.2.4 Characterization

To analyze the response of the samples to changes in temperature, a Nikon Eclipse Ti-E microscope at 10X and 20X magnification in the DIC mode used for acquiring time-lapse images. Nano-indentation analysis was performed by an atomic force microscope (AFM, NanoWizard4, JPK Instruments). We used the AFM cantilever which has a cylindrical tip with 5 µm end radius (SAA-SPH-5UM, Bruker), and the spring constant is 0.191 N/m. The averaged Young's modulus was obtained from 64 points within 10 µm × 10 µm region on a hydrogel block.

3.2.5 Biocompatibility tests

Cell culture and viability assay Human umbilical vein endothelial cells (HUVECs), were obtained from Lonza, Germany. For cell culture maintenance, Endothelial-cell growth medium (EGM™-2)

(500ml) with supplements (Human epidermal growth factor(hEGF) 0.5 ml, Vascular endothelial growth factor (VEGF) 0.5 ml, R3 insulin like growth factor-1 (R3-IGF-1) 0.5 ml, ascorbic acid 0.5 ml, hydrocortisone 0.2 ml, Human fibroblastic growth factor (hFGF-β) 2.0 ml, heparin 0.5 ml, FBS 10.0 ml, GA 0.5 ml) was used. All dishes and cell culture flasks were coated with sterile 0.1% gelatine solution in Dulbecco's balanced salt solution (DPBS) before use. For material exposure (3D printed PEGDA and pNIPAM structures), the HUVECs were seeded at a concentration of 3 x 10^5 cells/ml into cell culture dishes (35 x 10 mm^2) with or without sterilized glass coverslips which had the incorporated 3D printed PEGDA and pNIPAM structures on top. Cells were grown on the 3D-printed PEGDA and pNIPAM structure (including untreated controls) for 48h at 37°C and then analyzed by microscopy studies using the Live/Dead™ Cell Imaging Kit (Invitrogen, Thermo Fisher Scientific). The kit was prepared according to the manufactures protocol.

3.2.6 Finite element method (FEM) simulation for adhesion mechanism

The adhesion of the OHA robot was simulated in a commercial finite element simulation software (COMSOL Multiphysics 5.4, COMSOL Inc., Burlington, MA, USA) where a single structure was modeled and tested. The structure was modeled as a full three-dimensional structure rather than a symmetrical structure because of the non-symmetrical shape change during the process of adhesion. The structure was tessellated by total 13198 triangular meshes. The two different materials were used to represent the cylindrical wall and the protuberance structure due to the inhomogeneous material composition. Because of the strong adhesion and the elasticity of the hydrogel materials, the large deformation occurs during the adhesion. Thus, the hyperelastic material model is used to represent the nonlinear behavior of the materials. Specifically, the Mooney-Rivlin five parameter model is employed to represent the pNIPAM and PEGDA materials, [138] where the five parameters are achieved by fitting the stress-strain curves. The stress-strain

curves were measured by a commercial atomic force microscope (NanoWizard4, JPK Instruments). Due to the difficulty to achieve the full stress-strain curve via an AFM machine (the machine cannot apply high stress), partial regimes of the stress-strain curves of the materials are utilized (up to 0.15 strain). The rest of the material behavior is assumed to be similar to a conventional rubber material (ISO 37:2005).[46] With this process, the achieved values for the PEGDA are C_{10} = -0.372 MPa, C_{01} = 0.474 MPa, C_{20} = 1.15 MPa, C_{02} = -0.609 MPa, and C_{11} = 1.69 MPa, and pNIPAM are C_{10} = -25.9 kPa, C_{01}= 33.0 kPa, C_{20} = 80.1 kPa, C_{02} = -42.4 kPa, and C_{11} = 118 kPa. The adhesion was simulated by applying the negative pressure differential between the inside and the outside of the structure. The pressure differential was calculated by dividing the adhesion of a single structure (3 mN from the experiments divided by 10 × 10 structures in an array) by the estimated adhesion area (the inner diameter of the pore of the OHA, 32 μm), which results in 30 kPa. When the pressure differential is applied, the cylindrical wall collapses by the external positive pressure until the wall is stopped by the protuberance structure with mechanical contact, which is modeled as contact condition in the simulation environment. Additionally, the structure is allowed to slip at the interface by applying roller constraints. To enhance the convergence for solving the simulation problem, an iterative solver is employed in the simulation environment (100 steps to 30 kPa). Finally, the adhesion is calculated by the surface integral of the pressure differential along the internal area enclosed by the top edge of the deformed wall.

3.2.7 Fabrication of the OHA robot

The OHA robot prototypes were stereolithography printed (Form 2, Formlabs, Somerville, MA, USA) with an elastic resin (Clear resin V4). After printing, the structure was cleaned thoroughly with isopropyl alcohol for 20mins and then it is cured with ultraviolet in the FormCure (Formlabs Inc.) at 60°C for 20mins. Later, the adhesive structure was assembled with the robot. The body

was a hemisphere mounted on a cuboid structure, with width of 4mm, a height of 15 mm and a wall thickness of 1mm. There was an inlet hole for assembling cuboid magnet inside with a width of 4 mm, a depth of 2 mm and a height of 2 mm.

3.2.8 Remote heating system

The remote heating system consisted of a 24-turn transmitter coil with a 6-cm diameter. The coil was powered by a broadband amplifier (BBA 150, Rohde & Schwarz). Temperature change by alternative electric current were optimized for remote heating system. Here, the alternating electric current in the coil generates alternating magnetic field, which in return creates alternating electric field on the surface of the targeted magnetic material. Although it is impossible to measure the generated electric current on the targeted magnetic material, the heating effect could be indirectly measured by the steady-state temperature on the surface of the magnetic material. The magnetic material (NdFeB, 2 x 2 x 2 mm^3 as the same material used in OHA) is placed on the 24-turn transmitter coil's axis with 12 mm displacement from the center. The coil runs 440 kHz alternating electric current with specified electric current and the steady-state temperature is measured by the optical temperature measurement system (FLIR ETS320).

3.3 Results and discussion

3.3.1 A tissue adhesion-controllable octopus-inspired hydrogel adhesive robot

For obtaining a small-scale adhesion-controllable robot, we introduce an adhesive pattern inspired by an octopus architecture composed of biocompatible hydrogels (Figure 3.1a). Two-photon-polymerization-based 3D microprinting[48, 65, 94] was used to fabricate octopus-inspired hydrogel heterostructures of different Young's moduli. First, PEGDA hydrogel was printed to form an outer wall inspired by the orifice of octopi. A pNIPAM hydrogel was printed with a precise alignment to complete an inner dome-like structure mimicking the protuberance of octopi that enhances wet adhesion as well as dry adhesion due to its structural property.[139] The temperature-dependence of the volume of the pNIPAM in the OP enables controlled adhesion on biological wet tissues, where the temperature is controlled by the external magnetic field-based heating on the adjacent magnetic material. Note that the outer hydrogel does not respond to temperature change by having a higher Young's modulus than the inner hydrogel, to prevent the OP architecture from collapsing under vertical preload (Figure 3.1b), thus operating as force-absorbing structure. Figure 3.1c shows the biocompatibility results of the used hydrogels for the OP. Biological cells grew well without any significant problems in solution as well as in patterned environments of both pNIPAM and PEGDA hydrogels. Based on the controllability of the adhesion on the tissue as well as the biocompatibility, the tissue-adhesion-controllable octopus-inspired hydrogel adhesive (OHA) robot can be used to move freely in the body and effectively implement local biomedical functions such as drug delivery (Figure 3.1d).

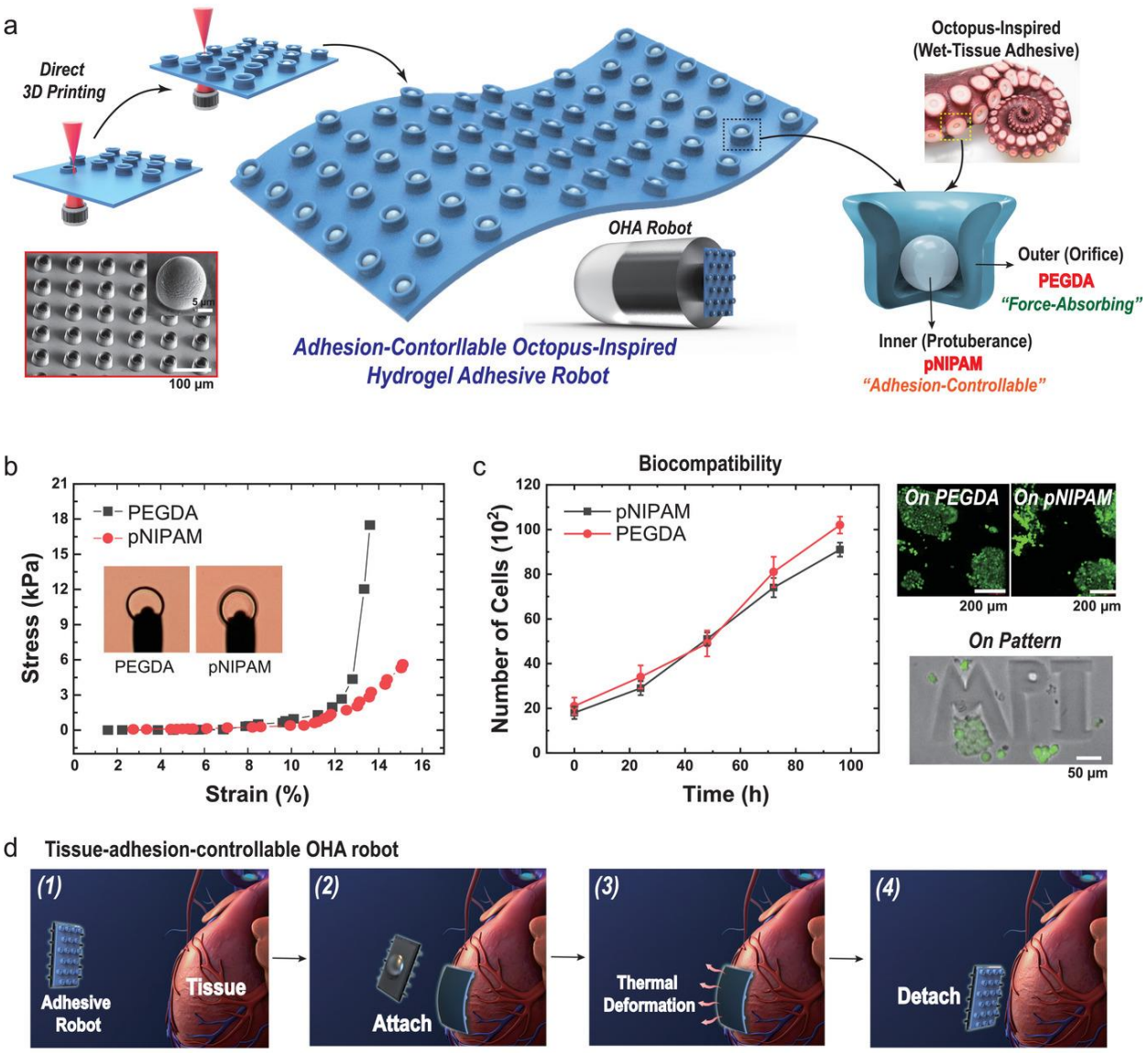

Figure 3.1 A tissue adhesion-controllable and biocompatible small-scale octopus-inspired hydrogel adhesive (OHA) robot. a) Fabrication process of an OHA robots. The OHA robots are inspired by the octopus sucker architecture using a direct 3D microprinting technique, where the outer sucker wall patterns are first printed using PEGDA hydrogel, and then the inner protuberance structures are printed with alignment using pNIPAM hydrogel. The OHA robots are made of a bullet shape, which has a built-in permanent magnet inside. b) Indentation stress–strain curves for the PEDGA and pNIPAM sucker patterns. Insets show the still-cut optical microscope images of

the moments that stress is applied to the patterns of PEGDA and pNIPAM with an atomic force microscopy probe. c) Biocompatibility test of the used PEGDA and pNIPAM hydrogels using HUVECs. The growth of biological cells is observed every 24 h in solution (upper right) and pattern (lower right) of PEGDA and pNIPAM, respectively. d) Scenarios where the OHA robot attaches and detaches from a tissue surface with a controllable wet adhesion for future minimally invasive biomedical functions.

3.3.2 Adhesion performance of the OHA patches

The adhesion performances of the OHA patches were investigated in Figure 3.2. The dome-like protuberance structure of the OP was capable of achieving strong wet adhesion under an external preload by generating a cohesive force among liquid molecules on interacting wet surface. [68] To verify the adhesion mechanism of the OHA patch, we conducted a finite element method (FEM) simulation (Figure 3.2a). The OHA employed suction-based adhesion, where the pressure differential between the inside and the outside of the wall of the hollow cylindrical structure created the adhesion. Here, the adhesion was proportional to the area of the suction and the applied pressure differential. Specifically, the negative pressure depended on the preload applied to the OP structure creating the negative vacuum. Due to the low stiffness of the wall structure based on hydrogels, the negative pressure deformed the wall to collapse the structure without inner protuberance structure, thus shrinking the effective suction area (left of Figure 3.2a). However, the collapse of the wall was alleviated by the protuberance structure which supported the wall when a collapse occurred (right of Figure 3.2a). This suggests an important design factor for developing a OHA patch, in which the outer wall must show a high modulus to prevent the OP structure from collapsing due to preload, and the inner protuberance must be volume-changeable to modulate the mechanical supporting point of the wall.

To better understand the adhesion behavior in wet condition, we fabricated the OHA patches in various combinations of materials (pNIPAM and PEGDA) and structural patterns (flat, sucker only, octopus). The adhesion was measured in a uniaxial adhesion setup. A smooth hemispherical glass tip (radius of curvature 4 mm) was used to apply controlled preloads on the OHA patches that were fully immersed in deionized (DI) water. The contact area between the tip and the OP structure depends on the applied preloads due to the softness of the materials. For all measurements, the approach and retraction speeds were fixed to 10 and 50 μm/s, respectively and the relaxation time was 10 sec. As shown in Figure 3.2c, our measurement setup provided reliable adhesion data in underwater conditions. The representative time-dependent profiles of the adhesion indicate that there were no adhesive artifacts, such as viscoelastic effect. First, the adhesion forces were investigated in three-different patterns consisting only of the PEGDA hydrogel (Figure 3.2c). The preloads were applied from 0.3 to 30 mN. Although wet adhesion is governed by parameters such as surface tension of the fluid, Laplace pressure, and viscous forces, the PEGDA hydrogel without patterns had little wet adhesion because of its low surface energy. The formation of the sucker structure created higher wet adhesion. The sucker with dome-like protuberance structure inside (named here as the octopus structure) was a more effective architecture to enhance adhesion in wet environments because of the enhancement of the suction stress. Next, the pNIPAM hydrogel was used to test wet adhesion in the patterns. The adhesive patches based on pNIPAM exhibit higher wet adhesion than of the ones based on PEGDA (Figure 3.2d and e). However, they showed low reliability in repetitive attachment-detachment cycles because of the collapse of the sucker structure driven by low mechanical strength under repeatedly applied preloads. In addition, the adhesive patch with the PEGDA wall exhibited wet adhesion strength at a preload much lower than it with the pNIPAM wall, thus indicating low preload threshold of adhesion. It means that the

stiff PEGDA wall was advantageous to induce adhesion at low preload. As a result, the use of a heterogeneous structure of a hard hydrogel wall on the outside and a soft hydrogel inside would be very effective for making the OHA patches. As shown in Figure 3.2f, the heterostructure of hydrogels (inner pNIPAM and outer PEGDA) displayed low preload threshold of adhesion as well as high adhesion strength under low preload range (< 5 mN), thus suitable for application to biological adhesive robots that operate with micro-Newton forces. Since the contact areas between the glass tip and the pNIPAM or PEGDA material are measured to be increased as the preloads increased, the adhesion strengths in pressure (force per unit area) unit are replotted. As the PEGDA wall keeps the OP structure stable under preload (2 mN), the OHA patch with inner pNIPAM and outer PEGDA showed that the adhesion performance was highly robust to 1,000 attachment-detachment cycles (Figure 3.2g). In addition, the OHA patches exhibited reliable adhesion performances even in an underwater environment after experiencing a dry condition (30 min). The OHA patches showed different adhesion strengths depending on the volume ratio of the internal protuberance structure. As the ratio of the protuberance structure to the volume of suction increases, the adhesion strength tended to increase, but it depended on the extent of the preload applied (Figure 3.2h).

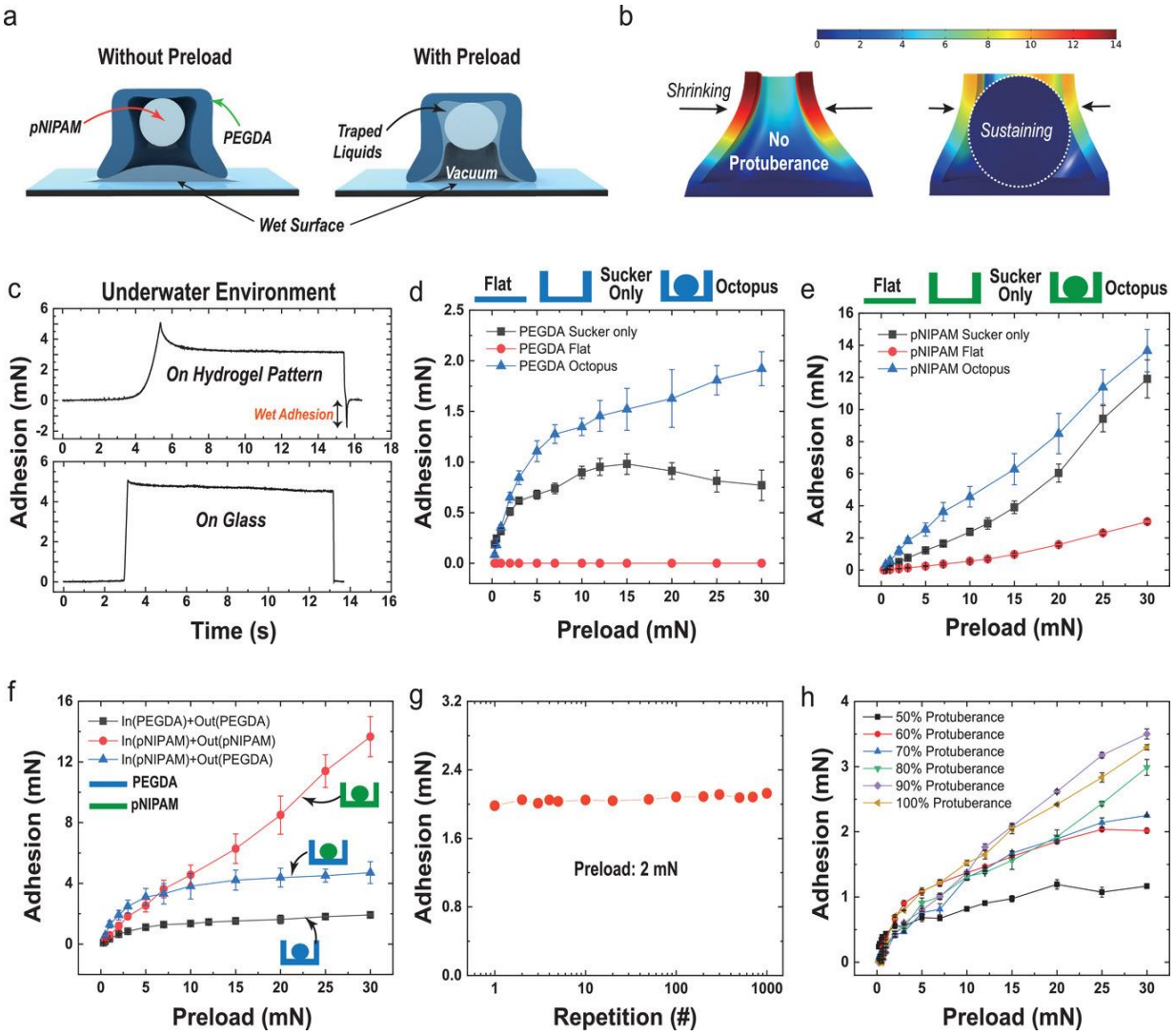

Figure 3.2 Adhesion performance of the OHA patches. a) Schematic illustration with finite element method simulation showing the adhesion mechanism of the sucker architecture with and without the inner protuberance structure. The inner protuberance structure prevents collapse of the hydrogel-based suction structure during preloading. b) Representative time-dependent profiles of adhesion results for the hydrogel patterns and flat glass for comparison, with a preload of 5 mN in underwater conditions. Adhesion forces for different preloads (0.3–30 mN) in the samples of c) the inner PEGDA and outer PEGDA, d) the inner pNIPAM and outer pNIPAM, and e) the inner pNIPAM and outer PEGDA. To confirm the effect of sucker and protuberance structures,

measurements are performed on each of the three structures (flat, sucker only, and octopus). f) Repeatable adhesion of the inner pNIPAM and outer PEGDA octopus sample after more than 1000 cycles of attachment and detachment with a preload of 2 mN. g) The adhesion as a function of the occupancy ratio (50%–100%) of the internal protuberance structure for the inner pNIPAM and outer PEGDA octopus sample. Here, the occupancy ratio is the ratio of the diameter of the protuberance to the width of the sucker. For all measurements, error bars represent standard deviations [N = 5 for (d)–(f) and N = 3 for (h)].

3.3.3 Controllability of adhesion using heating by external magnetic field

The ability to control the adhesion of the OHA was confirmed in Figure 3.3. The temperature dependence of the volume of pNIPAM and PEGDA hydrogels was investigated in Figure 3.3a and **3**b. The hydrogel spherical patterns were fabricated by the 3D microprinting technique, which were then immersed in DI water at room temperature. As a result of measuring the volume change while raising the temperature from 27 °C to 45 °C, the pNIPAM showed a volume reduction about 32%, but the PEGDA showed less than 1% change. This is because the pNIPAM typically exhibit a phenomenon known as the low critical solution temperature (LCST) behavior. [140-145] In the temperature range below LCST, the polymer chains of pNIPAM become hydrophilic and form hydrogen bonds with water molecules in aqueous conditions. Hence, the hydrogel network of pNIPAM swells below its LCST due to water absorption. As temperature elevates above the LCST, the polymer chains of pNIPAM transit into hydrophobic state and expels water out of its network to demonstrate shrinkage of the material. We defined a shrinkage rate of thermal dependent hydrogel as the proportion of the length change to the initial length as

$$\varepsilon = -\frac{l_0 - l}{l_0}, \tag{3}$$

where l and l_0 are the length of the contracted and original protuberances, respectively. Upon decreasing the temperature, the structures became hydrophilic again and restored their initial length by swelling with water. The temperature-dependent volume changes exhibited a similar tendency for cooling and heating of the pNIPAM and PEGDA, respectively. By applying the temperature-responsive pNIPAM to the protuberance structure in the OP, we could construct an adhesion-controllable adhesive. As shown in Figure 3.3c, the OHA with 90% occupancy of the protuberance exhibited higher adhesion in at 27 ℃ than at 45 ℃ because of the controlled effective suction area by the volume change of the protuberance structure, which is subject to the temperature change of the environment. Thus, we could adjust the adhesion by modulating the temperature of the protuberance structure. The relationship between the size of the protuberance structure and adhesion is explained in **Figures 3**d,e are based on our finite element analysis (FEA) simulations (see Experimental section for the simulation details). When the negative pressure was applied inside the OHA for suction, the external positive pressure deformed the wall of the OHA until the deformation stopped due to the mechanical support from the dome-like protuberance structure (Figure 3.3d). Here the mechanical contact point between the OHA wall and the protuberance structure was modulated by controlling the volume of the protuberance structure, where the higher volume of the protuberance structure could secure the larger effective suction area at the top of the OHA than the smaller volume of the protuberance structure. This relationship is quantitatively shown in Figure 3.3e where the large diameter of the protuberance structure secured the high effective suction area resulting in higher adhesion compared to the smaller protuberance structure. Because the volume of the protuberance structure is directly controlled by the environmental temperature, the adhesion is modulated by the temperature change.

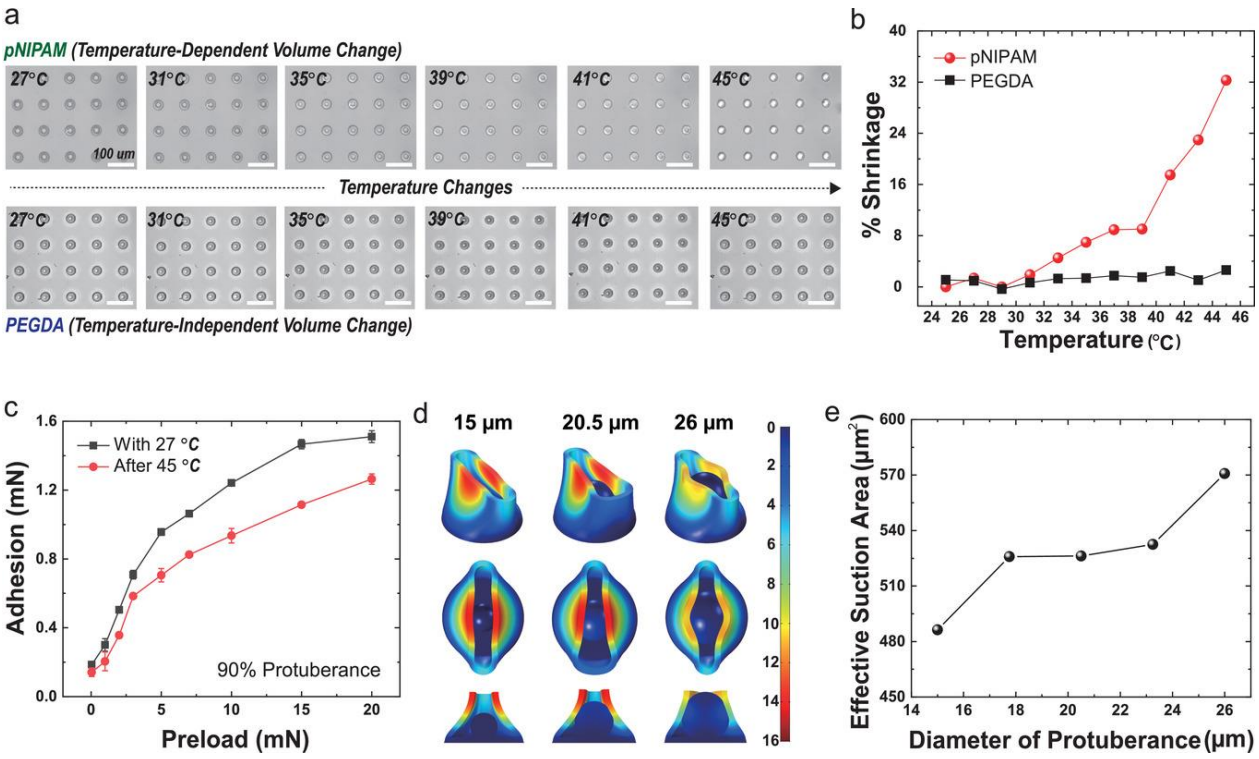

Figure 3.3 Controllability of adhesion using external heating generated by the applied external magnetic field. a) Optical images showing real-time volume changes for spherical patterns of pNIPAM and PEGDA hydrogels with temperature changes (27–45 °C). b) The actuation strain, defined as $(l-l_0)/l_0$, with increasing temperatures for the pNIPAM and PEGDA hydrogels. c) Adhesion results for different preloads (0.5–20 mN) in the OHA samples with 90% protuberance for 27 and 45 °C DI water environments. d) Deformation of the OHA structures when the pressure differential is applied for suction (30 kPa). The larger the protuberance structure is, the larger the effective suction area is preserved by the mechanical supports on the OHA wall from the protuberance structure. The color bar represents the mesh displacements from the non-deformed OHA in μm. e) The effective suction area for different protuberance diameters. The positive correlation between the diameter of protuberance and the effective suction area is found, where the larger suction area results in higher adhesion.

3.3.4 Proof-of-concept of the tissue adhesion-controllable OHA robot

The Proof-of-concept operation of the tissue-adhesion-controllable small-scale OHA robot with a biomedical function while exploring the inside of the body is demonstrated in Figure 3.4. For effective implementation, the OHA robot should be able to attach strongly to the target tissue and separate on demand when the operation is over. The OHA robot prototypes were fabricated with a bullet shape for easy locomotion in the body (Figure 3.4a). Three 8 mm^3 (2 mm × 2 mm × 2 mm in volume) magnets were embedded inside to control the locomotion of the robot by an external magnetic field and the OP patch sample was attached to the magnet tip. As shown in Figure 3.4b, heat delivered by the alternating external magnetic field on the magnetic material was uniformly transferred throughout the sample (8 mm^3). It is also possible to embed the magnetic nanoparticles inside pNIPAM to directly address the remote magnetic heating, which would make the system compact and open up possibilities for other applications. However, this can affect the adhesion performance by stiffening the pNIPAM material and by reducing the bulk material to induce heat (the volume of nanoparticles included in the pNIPAM would be significantly smaller than the bulk magnet used here), which needs further investigation.

Our OHA robot showed strong adhesion on a pig skin replica surface. The adhesion was measured with the preload ranging from 0.5 to 30 mN on a skin replica surface, which is similar to human skin, completely submerged in DI water. The adhesion measured on the pig skin decreased by about 3 times or more due to the roughness of the pig skin surface than that measured on the smooth glass surface (Figure 3.4c). However, it showed more abrupt changes in adhesion with temperature change because of the decrease in adhesion of local parts due to the roughness of the skin surface, meaning that the tissue adhesion can be controlled with the temperature change (Figure 3.4d). The OHA robot showed strong adhesion on the pig skin at room temperature (25 °C),

but with a temperature change to 45 °C, the adhesion decreased by about three times, so it could easily detached. Moreover, this attachment-detachment behavior was reversible in response to temperature change cycles.

Finally, the application of the OHA robot to reach a target position in the body and realize a biomedical function was demonstrated. The small-scale OHA robot responded to an external magnetic field and moved even well in an underwater environment with fine resolution (Figure 3.4e). Here, the actuation and tracking of the OHA using the magnetic field were performed in a custom-designed nine-coil electromagnetic setup. The magnetic field is dynamically changed by the electromagnetic setup in a way that the robot performs rolling locomotion on the surface of the in-vitro stomach model to approach the target. The position of the robot is tracked by a magnetic localization setup associated with the actuation setup. When the robot is on the target tissue, the magnetic field gradient on the magnet of the OHA robot increases to induce magnetic force towards the target. The magnetic field gradient strength is calculated to match the desired preload based the position and the magnetic moment of the robot. The robot adhered to the desired target tissue, and after realizing the function like target drug delivery, it is detached with externally controlled heat generation (Figure 3.4f). The strong tissue adhesion ability helped to effectively implement the biomedical function. In addition, owing to detachment without secondary damage on the pig skin, the robot could explore stomach and intestines of the body and implement various future biomedical functions. We also demonstrated a rhodamine encapsulated pNIPAM-based protuberance to inspire applicability of the OHA robot for drug delivery.

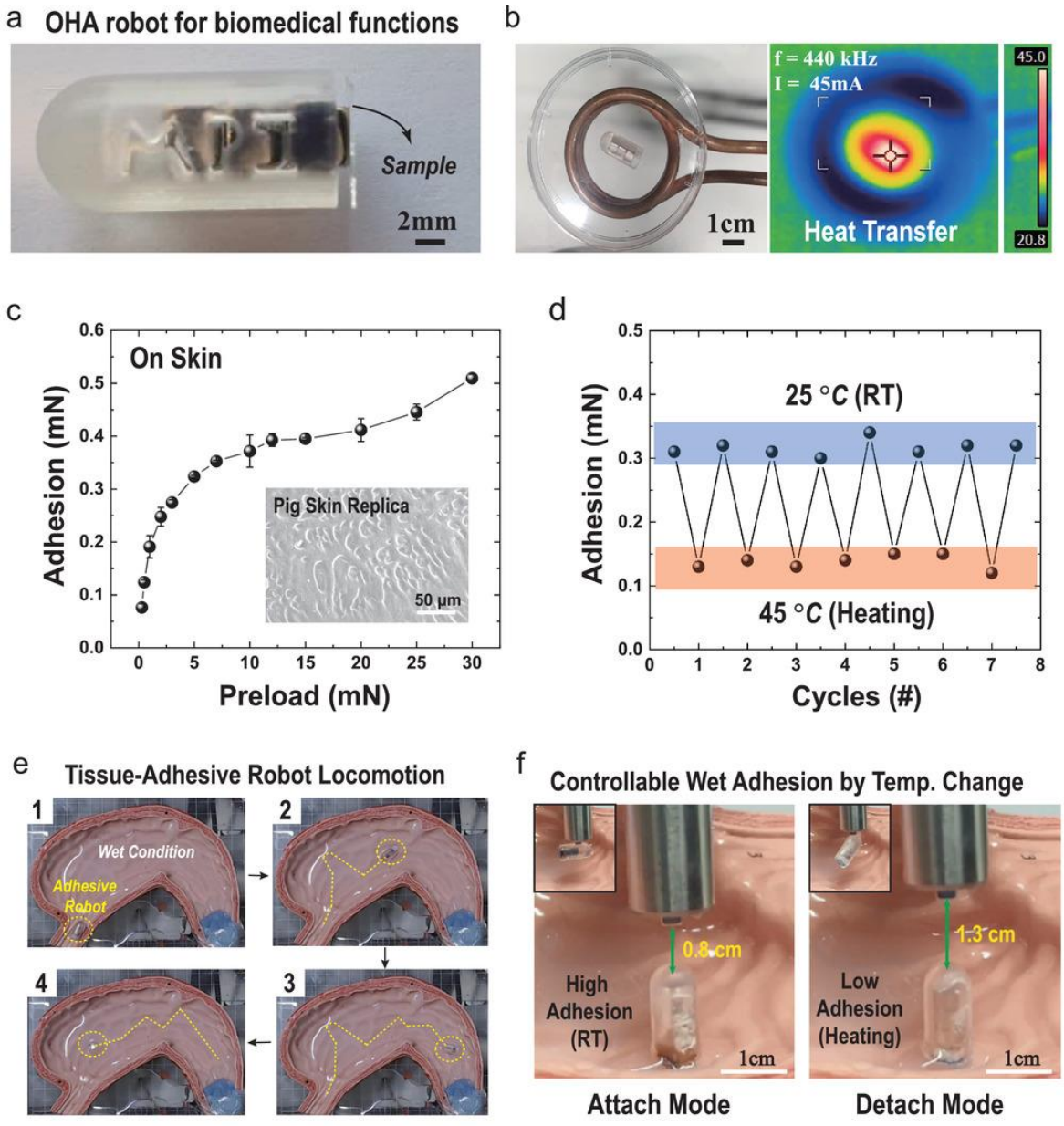

Figure 3.4 Proof-of-concept demonstration of the tissue adhesion-controllable small-scale OHA robot. a) Photography of the OHA robot that is made by attaching the OHA sample to a bullet-shaped polymeric shell with a built-in magnet. b) Photography and thermal images showing heat transfer induced by the external magnetic field throughout the sample. c) Adhesion results for different preloads (0.3–30 mN) in underwater conditions measured on the pig skin replica shown in inset. d) Controllable adhesion results on a pig skin replica during 25 and 45 °C under DI water.

The OHA samples with 90% protuberance are used and the applied preload is 5 mN. e) In vitro test showing sophisticated locomotion of the OHA robot to find the target tissue in the body environment. f) Tissue adhesion test at different temperatures. The OHA robot maintains the attach mode with high adhesion at low temperatures, but switches to the detach mode on demand due to the heat generated by the external magnetic field. The different adhesion on the tissue is measured as the distance at which the attractive force with the approaching magnet occurs.

3.4 Summary

As a method to enhance the efficiency of implementing biomedical functions of small-scale robots operating in the body, we propose a strategy to control the tissue adhesion where biocompatible hydrogel materials were used due to their harmless biocompatible nature in the body, and the octopus-inspired architectures were introduced by the direct 3D microprinting technique for strong wet adhesion in the internal environment of body. In particular, introduction of pNIPAM hydrogel that had temperature-dependent volume change property enabled controllable tissue adhesion by using externally applied magnetic fields. The small-scale robots with controllable and strong wet adhesion on tissues enhances the adhesion at the interface between the tissues and the robot. In addition, by repeating attachment and detachment operations freely by the externally applied magnetic fields, it is possible to implement various biomedical functions repeatedly without any damage to tissues.

Chapter 4. Multifunctional 3D-Printed Pollen Grain-Inspired Hydrogel Robots for On-Demand Anchoring and Cargo Delivery

Reprint from reference. [146]

Adv. Mater. 2022, 2209812

DOI: 10.1002/adma.202209812

4.1 Introduction

Magnetic mobile micro-scale robots have become promising systems for targeted, controlled, and minimally invasive drug delivery and therapeutic treatment of disease at hard-to-access local human body sites, due to their active navigation.[32, 87, 114, 116-119, 147-149] Efforts have been made to the development and implementation of such mobile micro-scale robots, including fabrication of micro-scale soft robotic devices[108, 122], synthesis of biocompatible or responsive (adaptable) materials[123, 150-151], and strategies for locomotion inside the body. [92, 125, 152-156]A myriad of remotely controlled mobile micro-scale robots has been proposed to enable shape change, multi-functionality, and reconfiguration in response to different stimuli, such as magnetic fields[104, 157-160], temperature[161-162], chemical[163-164], light[165], and ultrasound[166-167], for diverse medical applications, such as target drug delivery, minimally invasive surgery, and remote sensing.[168-169] However, untethered micro-scale robot interaction with harsh biological tissues, complex biofluidic environments, and overlap of multiple stimuli is one of the major challenges for their future medical applications.[170]

The operation of the untethered micro-scale robots is limited in the human body composed of complex physiological environments with a myriad of stimuli, which might trigger unwanted actuation with unwanted function.[80, 171] Without decoupled multifunctionality (multifunctional structure), multi-input stimuli of the robot's responsive structures overlap each other, resulting in a partial loss of substantial functional capabilities.[48] In order to avoid the interrupted actuation, decoupling the multiple stimuli inputs is crucial by making each stimulus respond for a single function only. In addition to decoupling multifunctionality, achieving controllable attachment to soft biological tissue is essential for the target implementation, such as collecting bio-signals,

applying electrical signals to nerves, and delivering drugs at targeted locations.[85, 172-174] However, current designs of micro-scale robots have put more weight on steering and locomotion, so they possess relatively simple surface morphology and lack certain functions, such as attachment ability.[175-176] Inspired by nature, there has been a wide range of biological materials with a variety of morphological structures which have given us solutions to numerous engineering challenges.[67-69, 177] Among them, pollen grain is emerging as an alternative to adhesive structure for targeted drug delivery applications due to their unique nanospike-like morphology and large inner cavity structure.[81, 83, 178] Despite the development of the pollen-grain-inspired application, a majority of suggested structures have been made from natural pollen grain composed of passive materials or single responsive material, which limits their functional diversity.[70, 78-79, 179] Decoupling the functions is crucial for achieving successful targeted drug delivery. If the robot has neither mobility nor the ability to control the attachment, the drug delivery cannot be targeted. If the drug release is passive rather than active, the drug encapsulated in the robot loses concentration due to leakage during locomotion. Thus, the three functions (locomotion, attachment, and drug release) should be decoupled for successful targeted drug delivery.

Here, we report a multifunctional pollen-grain-inspired hydrogel (MPH) robot for targeted active drug delivery and controllable attachment for biological tissues. We printed the 3D MPH robots (120 μm in diameter), composed of a temperature-actuated spherical-shaped shell for controllable attachment, a pH-responsive cargo releasing sphere structure, and a magnetic-actuated layer with spikes. The ferromagnetic FePt nanoparticles encapsulated with microrobots were actuated and steered by external rotating magnetic fields, reaching up to a translational speed of 532 $\mu m.s^{-1}$. Furthermore, the robot was designed to allow the outer shell of Poly N-isopropylacrylamide (pNIPAM) to shrink down to 49% by increasing the temperature of the outer

shell through a temperature-responsive approach, which enables controllable attachment by spike exposure. Finally, Poly N-isopropylacrylamide Acrylic acid (pNIPAM-AAc) was introduced to perform pH-responsive on-demand cargo release applications. The MPH robot design conceptualized here establishes the proof of concept for executing multiple tasks within a single microrobot structure for various future medical robots for their improved intelligent functionality.

4.2 Materials and Methods

4.2.1 Synthesis of pNIPAM and pNIPAM-AAc

pNIPAM (Scientific Polymer Products Inc) and pNIPAM-AAc (Scientific Polymer Products Inc.) solution was synthesized with the following recipe. A 3 g of NIPAM monomer, 0.4 g pNIPAM, and 0.17 g BIS (Sigma-Aldrich) were dissolved in 10 mL of ethylene glycol under stirring overnight (600 rpm) at 40 °C.

To this mixture solution, 310 µL of AAc (w/w) was added, followed by a 3% (w/w) Lithium phenyl-2,4,6-trimethylben zoylphosphinate (LAP, Tokyo Chemical Industry Co. Ltd.) photoinitiator. The mixture was stirred (500 rpm) at 50 °C until all the components were mixed thoroughly.

4.2.2 Synthesis of L_{10} Phase FePt Nanoparticles

FePt nanoparticles were synthesized as reported by Yu, Y. et al. with slight modification to the protocol. [180] Briefly, 0.2 mmol Pt(acac)2, 0.2 mmol Fe(acac)2, 0.8 mmol CTAC and 0.5 ml oleic acid, were mixed with and 10 ml oleylamine. The mixture was stirred under Argon gas for 1 h at room temperature. Afterward, the solution was heated to 350 ºC at ~5 ºC min^{-1}. The mixture's

temperature was kept constant at 350 ºC for 3 hours. Subsequently, the reaction mixture was cooled down to room temperature. FePt nanoparticles were precipitated by adding ethanol and centrifuged at 8000 rpm for 3 min. The particles were redispersed in hexane and again precipitated in ethanol, followed by centrifugation. This process was repeated at least five times to ensure the removal of the unreacted species and excess surfactants. The particles were then dispersed in hexane for storage and future use.

4.2.3 Dispersion of Particles in PETA

2 mg of dried FePt nanoparticles were mixed with 1 ml of PETA (Sigma-Aldrich) and the photoinitiator mixture. A uniform dispersion is obtained using probe sonication for 1 min.

4.2.4 Fabrication of the Multifunctional Pollen-Grain-Inspired Hydrogel Robot

The cleaning process of glass substrates includes immersion in acetone and isopropyl alcohol and drying by nitrogen gas flow. The pNIPAM-AAc precursor mixture solution was dropped on a glass substrate for fabricating a pH-responsive sphere structure. A commercial Direct Laser Writing setup (Photonic Professional GT, Nanoscribe GmbH) with a 25X, NA= 0.8 oil immersion objective was used to print the pH-responsive sphere structures. The printing parameters are 50 mW of laser power and 50,000 µm s^{-1} of scanning speed, respectively. After the 1st step of the printing, the spherical structures were developed with isopropyl alcohol for 30 min to remove the residue of pNIPAM-AAc. Then, FePt-loaded PETA prepolymer mixture droplet was dropped on the 1st printed structure. Laser power and galvanometric mirror x- and y-scanning speeds for FePt-loaded Peta structure were optimized to 80 mW and 50,000 µm s^{-1}, respectively. The 2nd development was performed using isopropyl alcohol for 30 min to get high-quality 3D-printed submicron structures. To print the outer crust, we dropped the pNIPAM mixture solution on the spike structure. Printing parameters for the outer crust were optimized to a laser power of 60 mW

and scanning speed of 50,000 μm s^{-1}. The design of MPH consists spherical structure, spike, and an outer crust (120 μm in diameter).

4.2.5 Characterization

To analyze the samples in response to temperature and pH, a Nikon Eclipse Ti-E microscope at 10X and 20X magnification in the DIC mode was used for acquiring time-lapse images.

4.2.6 COMSOL Simulations

COMSOL Multiphysics 6.0 simulation software (COMSOL, Inc.) was used to estimate the drag and lift forces exerted on the robot in the bloodstream in a blood vessel. A pipe with an inner diameter of 1 mm and a length of 5 mm was modeled and used as the blood vessel in the simulations. The robot model was directly imported from the 3D model for printing the robot in Nanoscribe. The bloodstream was designed to have an average velocity of 5 cm s^{-1}, a viscosity of 6 cP, and a density of 1060 kg m^{-3}. The flow conditions were determined based on the study of human blood. [181]

4.2.7 Pull-Off Force and Frictional Force Measurement

A custom-built adhesion test setup was used to measure the pull-off force and frictional force. First, the 7-by-7 spikes and shells were prepared by using a two-photon polymerization 3D printer (Photonic Professional GT, Nanoscribe GmbH). Only the upper half of the spikes and shells with the 100-μm base were printed for the test. The spikes and shells were densely packed with a hexagonal pattern with a 200-μm interval. Second, a silicone sample (Ecoflex 00-30, Smooth-On Inc) or a porcine intestine sample were attached to a spherical tip and used as a counterface. After the sample was fixed in the test setup, the Load-Pull test for pull-off force and the Load-Drag test for frictional force were carried out. The counterface was moved to the spikes or shells until the normal load of 1 mN was achieved. Next, the counterface was pulled off with a 10 μm s^{-1} retracting

speed after 5 sec of relaxation time for measuring pull-off force or was sheared to 500 µm at a shear rate of 10 µm s^{-1} for measuring the maximum tangential force. For the wet condition with the silicone surface, several drops of deionized water were applied at the contact interface until the contact region was fully immersed in water.

4.2.8 Cell Viability Studies

The BJ fibroblast cell line (ATCC, CRL-2522™) originating from healthy human foreskin tissue was used as the model cell line for cell viability studies. BJ fibroblasts were expanded in T-75 cell culture flasks containing Dulbecco's Modified Eagle's Medium (DMEM; Gibco) supplemented with 10% fetal bovine serum (Gibco) and 1% penicillin/streptomycin (Gibco). The detachment of cells was performed using trypsin (0.25 wt %)/EDTA solution (Gibco) upon reaching 70% confluency.

For the biocompatibility assay, the cells were collected and seeded with a concentration of $1.5x10^5$/dish into 35 mm Petri dishes containing 9 MPH robot structures printed onto a glass slide. The positive control was treated with 20% DMSO (Sigma-Aldrich), and the negative control was kept untreated. All sample groups were performed in triplicates. The cells were incubated in an incubator at 37 °C in a humidified atmosphere of 5% CO_2 for 24, 48, and 72 h. The cell viability after exposure to the Pollen material was assessed using the LIVE/DEAD Cell Imaging Kit (Thermo Fisher Scientific, #R37601), which was performed according to the manufacturer's instruction. Fluorescence microscopy images were recorded using a Keyence BZ-X800E microscope. Live and dead cells were counted using the integrated hybrid cell count analysis module.

4.2.9 Magnetic Actuation and Steering of MPH Robot

MPH robot is actuated and steered using our custom-made five-coiled electromagnetic setup, which can be mounted on an inverted optical Zeiss microscope. (Zeiss Axio Observer A1) The experiments were performed under a varied magnitude of rotating magnetic field. The step-out frequency was acquired by increasing the frequency of the rotating magnetic field from 0 to 10 Hz. The velocities of the MPH robot were calculated using an in-house open-access MATLAB code. The velocity was calculated by every frame of MPH robot's position. For the experiments on biologically relevant cell surfaces, HT-29 colon epithelial cells were obtained from American Type Culture Collection (Rockville, MD, USA). The cells were cultured in Dulbecco's modified Eagle's medium supplemented with 10% (v/v) FBS, penicillin (50 UI ml^{-1}), and streptomycin (50 μg ml^{-1}) in a humidified, 37°C, 5% CO2 environment. For the experiments, the cells were seeded on glass slides coated with fibronectin and waited for 3 days to reach confluence.

4.2.10 pH-responsive on-demand cargo release

For on-demand pH-responsive drug release experiments, we first checked the pH-responsive behavior of the robots by using only the inner sphere structure (Figure 5 a-d). After ensuring the pH responsive ability, we performed the real drug release experiments using the fully assembled structure of the robot. The sphere structures printed on a glass substrate were loaded with a 1 mM drug analog molecule (CellTracker Deep Red Dye, Invitrogen) overnight at 4 °C. After overnight incubation, sphere structures loaded with drug analogs were washed several times with DPBS before the drug release experiments. We conducted the pH-responsive drug release experiments at pH 7.4 and pH 11. Briefly, the drug analog-loaded sphere structures were treated with different pH buffer solutions for 5 min. The time-lapse fluorescence intensities (bandpass emission: 670 nm)

over at least three sphere structures were measured using the Nikon software for each pH value. Background fluorescence was subtracted from the measured values.

4.3 Results and Discussion

4.3.1 Multifunctional pollen-grain-inspired hydrogel (MPH) robot for target drug delivery and controlled attachment

For the realization of multifunctional microrobots for controllable attachment, we selected pollen grain as a model with different stimuli-responsive materials for the proof-of-concept demonstration. By mimicking the special morphology of the contact elements from pollen grains, the MPH robots were generated using two-photon polymerization-based 3D microprinting.[65, 94, 182] As shown in Figure 4.1a, the MPH robot developed here consists of three main components: inner cargo carrier sphere, inner pollen-grain-inspired spike structure, and outer shell. In order to fabricate the robot with the three layers (Figure 4.1b), pNIPAM-AAc was firstly printed to form an inner cargo carrier sphere structure that takes part in on-demand cargo based on pH stimulus. Secondly, Pentaerythritol Triacrylate (PETA) with iron platinum particles (FePt) was printed with an accurate and precise alignment to generate spike-like structures inspired by the pollen spike. Lastly, pNIPAM without the AAc unit was printed to form the outer shell that covers the spikes for the temperature-dependent response behavior. The shrinkage of the pNIPAM outer shell in response to temperature increase enables controlled attachment by revealing the PETA spike. On the other hand, PETA with iron platinum particles only responds to magnetic fields, enabling rolling on biological surfaces with steering capability. Based on this decoupled actuation ability, the MPH robot can implement three different functionalities within a single microrobot structure: locomotion, attachment, and active cargo release in response to various independent inputs.

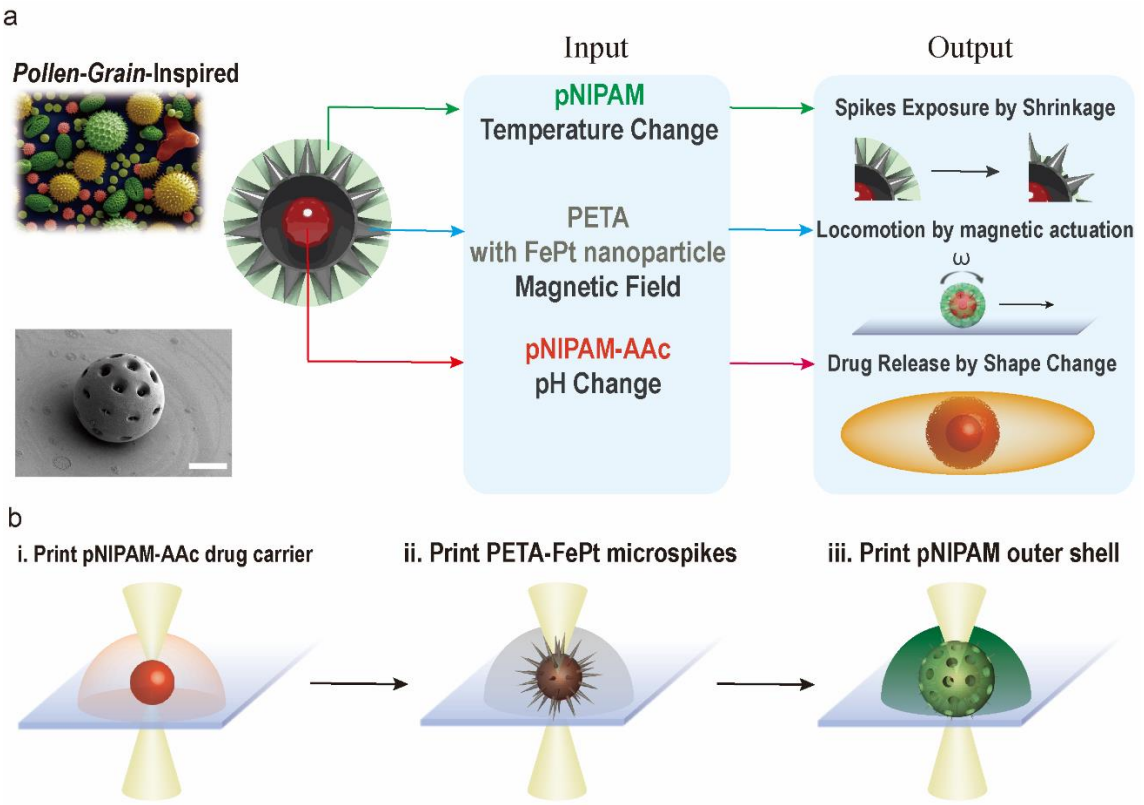

Figure 4.1 Multifunctional pollen-grain-inspired hydrogel (MPH) robot for target drug delivery and controlled attachment. (a) Schematic illustration of composition and operational principle of the MPH robot. 3D printed MPH robots were composed of a temperature-actuated crust shell for controllable attachment, a pH-responsive cargo releasing sphere structure, and a magnetic actuated spike structure with pollen-grain-inspired spikes. The integrated three different stimuli-responsive structures were actuated independently for their own functions. Scale bar: 50 μm. (b) Schematic illustrations of the fabrication process of an MPH robot. The MPH robots are fabricated using a direct 3D micro-printing technique. The active drug sphere is first printed with pNIPAM-AAc. After development, magnetically actuated pollen-grain-inspired spike structures are printed using PETA with FePt, and then the active outer crust shells are printed with alignment using pNIPAM hydrogel.

4.3.2 Temperature responsiveness of size-controllable outer shell of MPH

Depending on the temperature of the outer shell, the MPH robot can select two different modes as shown in Figure 2a: 1. Attachment mode by revealing the spikes over the outer shell, which enables the robot to attach to the target position, 2. Locomotion mode by keeping the spikes under the outer shell, which enables the robot to roll on the surface. Until now, existing microrobots were unable to alternate attachment to the surface. However, the MPH robot presented in this work could attach to the surface thanks to the shape-morphing ability of the MPH robot in a controlled manner. To explore the controllable attachment of the MPH robot, we investigated the temperature responsiveness of the outer crust shell made of pNIPAM hydrogel. We defined the shrinkage ratio (ε) of temperature-responsive crust structure as the ratio of the diameter change to the initial diameter of the crust structure as

$$\varepsilon(\%) = -\frac{l_0 - l}{l_0} \quad (4)$$

where l and l_0 are the diameter of the shrunk and initial outer crust, respectively. The outer crust structures were fabricated by 3D direct laser printing, which was then transferred into the deionized water at room temperature. As a result of measuring the shrinkage ratio of the shells with respect to temperature from 25 to 45 °C, the pNIPAM showed a diameter shrinkage of about 49% (Figure 4.2b-d). Hence, by integrating the spike with the pNIPAM crust, the MPH robot can select either locomotion mode or attachment mode to construct controllable attachment. The temperature responsiveness of the outer crust of the robot can be explained by the unique behavior of pNIPAM. Hydrogels of pNIPAM typically undergo changes in their state by low critical solution temperature (LCST) behavior.[141, 183-186] The pNIPAM structure expands with the water absorption below its LCST because the polymer network of pNIPAM is in a hydrophilic state and it formulates

hydrogen bonding with water molecules when they are immersed in an aqueous solution. When the pNIPAM is heated above its LCST, the polymer network of pNIPAM becomes hydrophobic, expelling the water out of its network and thus shrinkage of the structure. This shrinking and unshrinking process could be repeated without deterioration as shown in Figure 4.2e. Nevertheless, the response time of the MPH robot to reveal the spikes was relatively long (about 20 mins) due to the heat transfer method of hot air in this study. This might be further improved by alternating electric current using a coil setup.

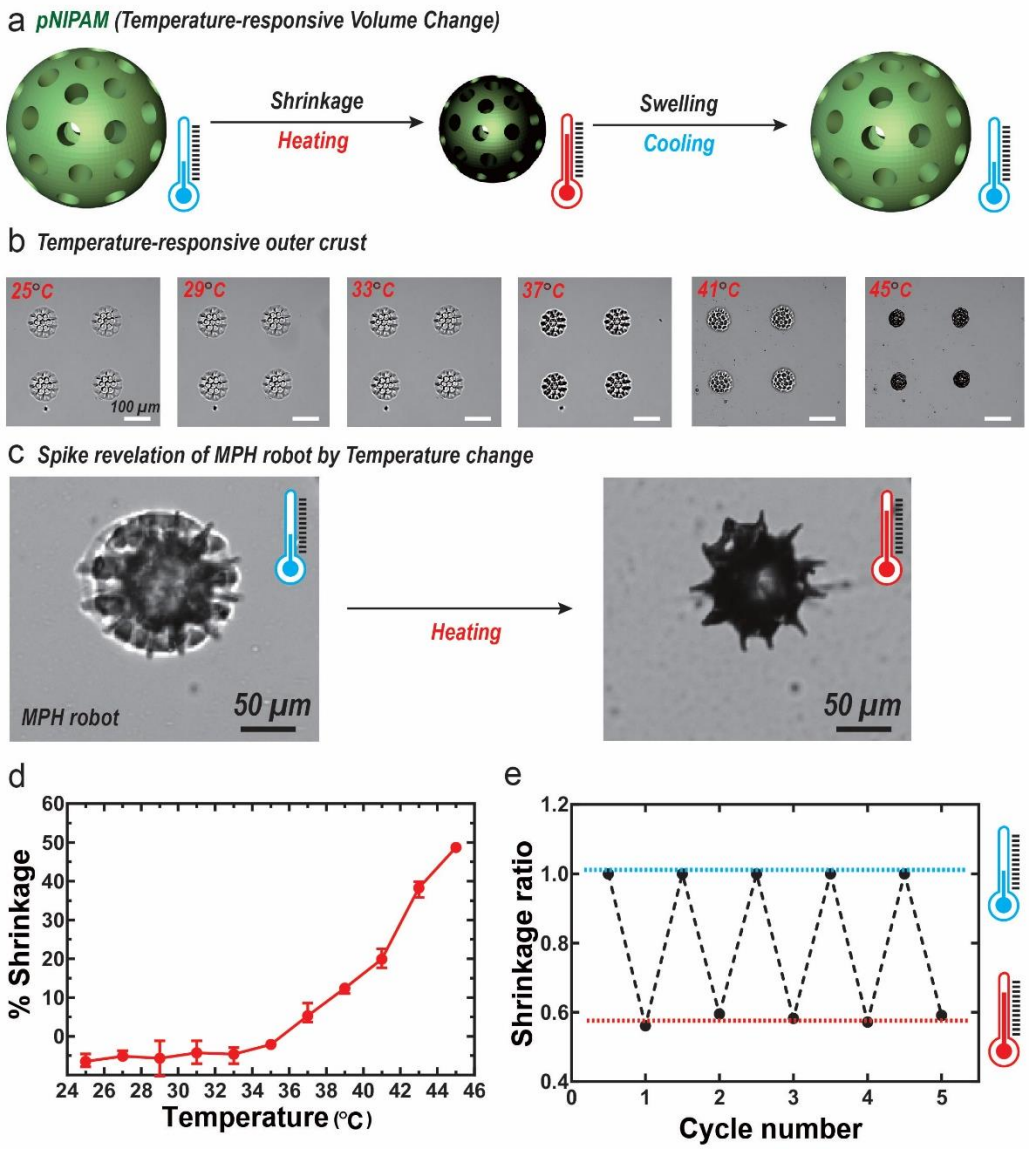

Figure 4.2 Temperature responsiveness of size-controllable outer shell of MPH robot (a) Schematic illustrations of temperature-induced shrinkage of the outer crust of MPH robot. (b) Microscopic images showing real-time size changes for outer crust structures of pNIPAM hydrogels with temperature changes (25-45 °C). (c) Optical images of the MPH robot with the controlled revelation of spike structure in response to temperature. (d) Shrinkage ratio, defined as $-(l-l_0)/l_0$, with increasing temperatures for the pNIPAM hydrogels. (e) The repetition test of the pNIPAM outer crust shrinking/unshrinking cycles without any deterioration.

4.3.3 COMSOL simulation of the drag and lift forces exerted on the MPH robot

When the MPH robot is attached to a biological surface for carrying out a task such as on-demand cargo delivery, the robot must remain on the surface despite external disturbances such as flow. Hence, it is crucial to verify if the attachment performance of the robot is good enough to withstand the disruptions in various conditions. Firstly, the drag and lift forces that the robot must resist in biofluid to remain on the surface of the biological channel were estimated by the COMSOL simulation. As fluid flows around the microrobot, it imparts a force upon the robot. The lift force is the component of this force that acts perpendicular to the incoming flow direction. This differs from the drag force, which is the component of the force that aligns with the flow direction. Under the fully-developed laminar flow condition with an average velocity of 5 cm s^{-1} in a biological confined channel with a 1-mm inner diameter, the velocity magnitude around the MPH robot was much lower than the velocity at the center of the biological channel thanks to the small size of the robot (radius: 60 μm) compared to the diameter of the biological channel (Figure 4.3a-c).

Thus, when the robot was attached to the channel, the lift and drag forces were only 0.008 μN and 0.204 μN, respectively (Figure 3d). Thanks to the lower drag force, it is postulated that the MPH robot can readily roll on the surface and anchor at the target spot even with flows against movement. However, depending on the robot's location, the drag force could be lower and the lift force could be even negative (Figure 3e-f). When the robot was located at the center of the biological channel, the lift force was zero while the drag force was the highest. As the robot approached the inner wall of the channel, the drag force decreased. However, the lift force increased until the robot reached a distance of 250 μm from the center line and then decreased beyond the distance. Furthermore, the lift force became negative when some part of the robot penetrated the inner wall of the biological channel, which means that the robot was pushed down

to the inner wall of the channel. This is attributed to the fact that some part of the lower half of the robot doesn't experience the forces from the flow. Hence, the drag torque could contribute to a greater penetration force and allow for more successful attachment to the surface. Based on these results, it could be concluded that the robot must resist the forces of at least sub-μN in both normal and tangential directions to remain on the surface in fluid environments, and the attachment force of the robot in the tangential direction is more important than the attachment force in the normal direction to stay still on the attached spot.

4.3.4 Adhesion performance of MPH robot

To analyze whether the robot can generate enough attachment performance and how effective the spike is in the attachment of the robot, the pull-off force and frictional force of the MPH robot were tested against engineering surfaces such as silicone or biological tissue. As shown in Figure 4.3g, the 7-by-7 printed spikes and outer shells of the MPH robot were prepared for the pull-off force and frictional force measurements, and the counterface sample (either Ecoflex 00-30 or porcine intestine) was used as a tip. When the spikes and outer shells were tested against the engineering silicone surface, the spikes didn't help to increase the pull-off force although they were marginally helpful to increase the frictional force regardless of the surface condition. In dry conditions, the spike sample showed ~0.4 mN of pull-off force and ~3.7 mN of frictional force while the shell sample showed ~0.9 mN of pull-off force and ~3.3 mN of frictional force in dry conditions (Figure 4.3h). Also, in wet conditions, the pull-off and frictional behaviors were the same, but the forces were significantly reduced to almost one-tenth of the measured forces in dry conditions. However, the spikes showed clear improvements in pull-off and friction against the porcine intestine as shown in Figure 4.3i. The outer crust shell sample showed ~0.5 mN of pull-off force and ~0.7 mN of frictional force, which were lower than the measured force values against

the silicone sample in dry conditions. On the contrary, the spike sample showed ~1.2 mN of pull-off force and ~2.8 mN of frictional force, which were much higher than those from the shells. These results can be explained by the difference in mechanical properties between the engineering silicone surface and the porcine intestine tissue surface as shown in Figure 4.3j. Since the silicone has high toughness and does not have any penetrable mucus on the surface, the spikes cannot penetrate the surface, which results in less contact area than the shells. Thus, the spikes could not demonstrate a higher pull-off force than the shells. However, the spikes can generate a higher frictional force from the mechanical interlocking between the silicone surface and the spikes while the shells just slide on the surface. Nevertheless, the engineering surfaces are easily lubricated by applying water droplets at the interface, which results in the reduction of pull-off and frictional forces of both the shells and the spikes. On the other hand, since the spikes can penetrate soft biological tissue surfaces, [187] the spikes could generate high pull-off and frictional forces compared to the shells, which cannot be explained without mechanical interlocking from penetration of the spikes. As for the attachment performance under the flow disturbance, the spikes can provide strong attachment since the pull-off and frictional force values are tens of μN (49 robots with spikes can generate over 1 mN), which are much higher than the values obtained from the simulation (sub-μN). Although the high adhesive and frictional forces might decrease with a lower preload, the capillary force between the mucus layer and the robot surface or an external magnetic gradient provided by a strong permanent magnet could help to provide sufficient preload for attachment. In addition, Figure S1 clearly showed the effect of spikes on attachment without maintaining an external normal load by demonstrating strong attachment to a biological tissue in a flow compared to the robot without the spikes. Hence, it can be concluded that the spikes of the

robot can help to attach to the surfaces in the human body by providing enough attachment performance despite external disturbances, especially against penetrable soft tissue surfaces.

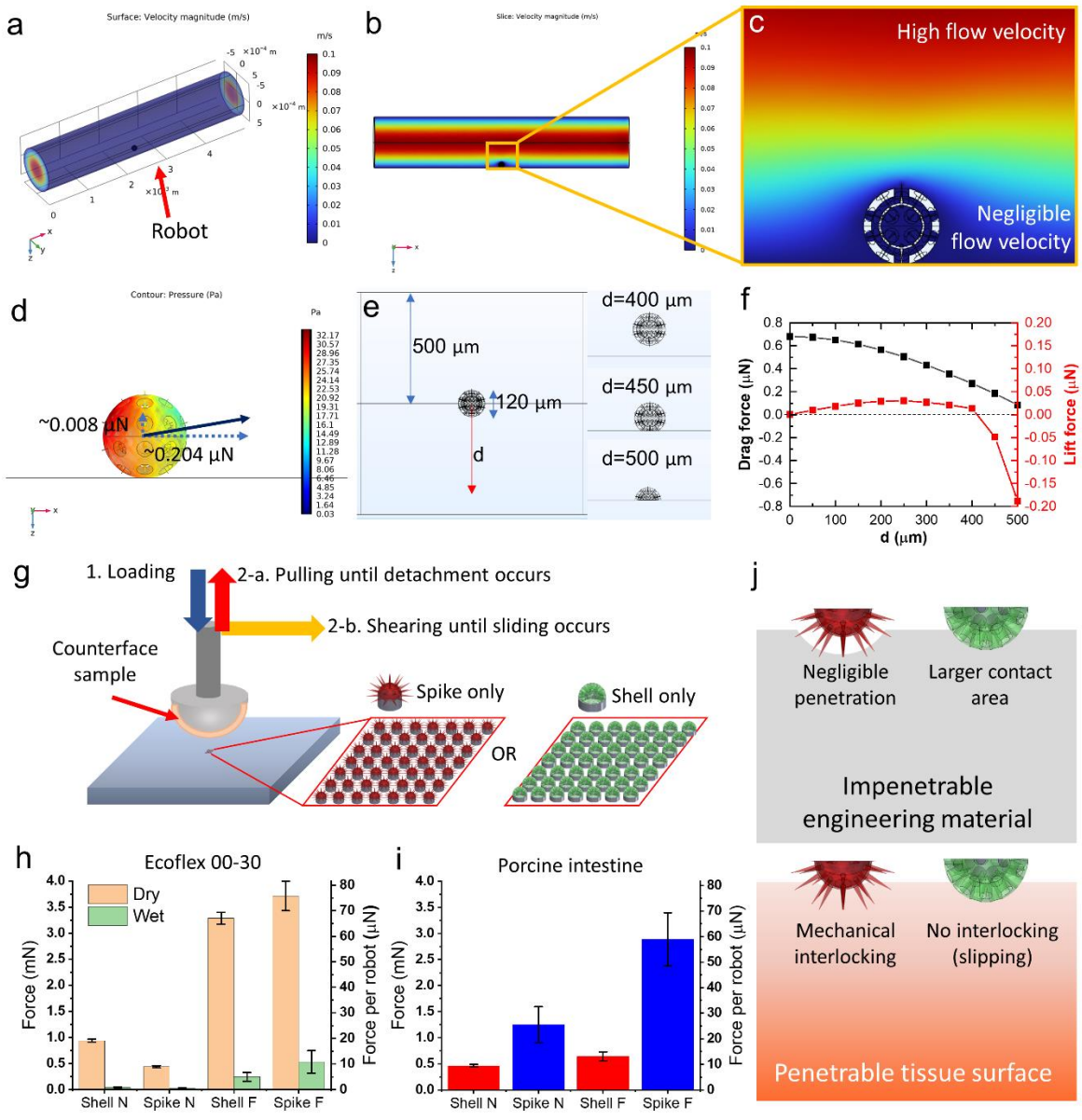

Figure 4.3 (a) COMSOL simulation for estimation of the drag and lift forces exerted on the MPH robot in a bloodstream (tube inner diameter: 1 mm, length: 5 mm). (b, c) Velocity magnitude nearby the robot and its magnified image, when the robot is attached to the surface of the vessel.

(d) Pressure distribution along the surface of the MPH robot, and the drag and lift forces acting on the robot. (e) Images of the robot located at the distance, d, from the center line of the vessel. (f) Drag and lift forces acting on the robot with respect to the distance from the center line to the robot. (g) Schematic of pull-off force and frictional force measurement of the spikes and outer crusts from the robot. (h) Pull-off force and frictional force measured from 49 spike-only robots and shell-only robots against Ecoflex 00-30 silicone surface in dry and wet conditions (Shell N and Shell F: Pull-off force and frictional force of the shell-only sample, respectively. Spike N and Spike F: Pull-off force and frictional force of the spike-only sample, respectively). Force per robot was obtained by dividing the measured force value by 49. (i) Pull-off force and frictional force of 49 spike-only robots and shell-only robots against porcine intestine. (j) Schematic image of the attachment behavior of the spike and shell against silicone and soft tissue.

4.3.5 Magnetically guided locomotion of the FePt-encapsulated MPH robot

In Figure 4.4a, we demonstrated the steering capability of the 3D-printed MPH robot to locomote by magnetic actuation. For the locomotion of the MPH robot, we encapsulated FePt nanoparticles inside the PETA. The transmission electron microscopy revealed that the FePt nanoparticles had a sub-100-nm size in diameter (Figure 4.4b). The vibrating sample magnetometer (VSM) analysis has shown that the FePt nanoparticles had hard ferromagnetic characteristics with 36 emu g^{-1} remanence magnetization, which is suitable for magnetic actuation. (Figure 4.4c)

Furthermore, we assessed the biocompatibility of the MPH robots to perform biomedical applications. We allowed human fibroblast cells to interact with the MPH robots for 48 h. At 48 h of incubation, we analyzed the biocompatibility of the structures with live/dead staining and

metabolic activity measurements. The results indicated that the fibroblasts did not exhibit any toxicity-induced change (Figure 4.4d-e).

We analyzed the rolling locomotion behavior of structures further. We applied rotational magnetic fields with a custom-made electromagnetic setup mounted on an inverted microscope for these experiments. [188] The rotational magnetic fields actuated and steered the MPH robot by exerting torque in the direction perpendicular to their rotational axis (Figure 4.4f-g). The roller-shape MPH robots converted the rotational behavior to translational movement due to the non-slip contact with the surface. [188] We also increased the applied frequencies stepwise, gradually increasing 1 to 10 Hz to investigate the MPH robot's step-out frequency which can be described as the point at which the robot starts to decrease its velocity. It was shown that the maximum forward velocity was 532 μm $s^{-1,}$ and the optimum actuation frequency (step-out frequency) was found at 5 Hz due to low encapsulation of FePt. Next, we investigated the motion of the MPH robot on the cellular substrate to confirm whether or not the robot possesses the capability to actuate and steer in the biological environment. As shown in Figure 4.4h, the MPH robot can freely roll on the colon epithelial, HT-29 cells without any disruption of the movement. Although the maximum velocity of 532 μm s^{-1} at 5 Hz might be high enough to successfully approach target spots, the translational speed is expected to be further improved by reducing the slip between the MPH robot and counterfaces or by improving the magnetic response of the embedded FePt particles. Other than that, closed-loop imaging-guided feedback mechanisms could also be implemented for improving controllability of the MPH robot. Each experiment is conducted three times.

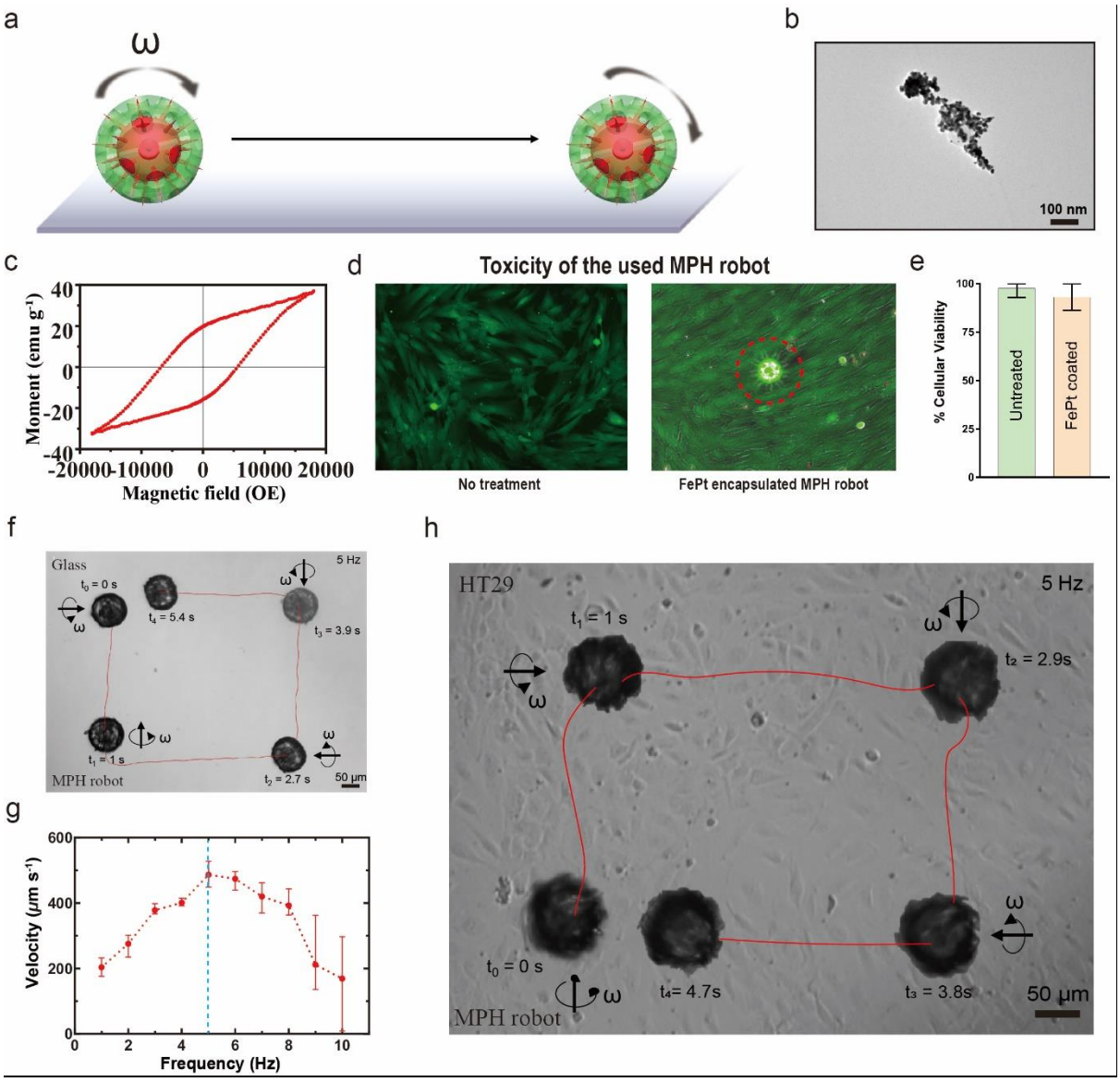

Figure 4.4 Magnetically guided locomotion of the FePt-encapsulated MPH robot (a) Schematic illustration of magnetic actuation and locomotion of the MPH robot (b) TEM image of the FePt (c) Magnetic hysteresis curve of the FePt-encapsulated MPH robot. (d) The biocompatibility of the MPH robot assessed with human fibroblast cells at 48 hours using live/dead staining. Green-live cells red-dead cells. (e) The quantified amount of the cell viability of pollen robot compared to no treatment. (f) Rolling trajectory of MPH robot on the glass substrate (g) Step-out frequencies of

MPH robot. (h) Demonstration of MPH robot rolling locomotion on the cellular (HT-29) surface without any interruption.

4.3.6 pH-responsive spherical structure of MPH robot using pNIPAM-AAc

To further improve the MPH robots by integrating the on-demand cargo release function, we introduced pH responsiveness by including acrylic acid (pNIPAM-AAc) in the precursor mixture before 3D direct laser printing. Carboxylic acid groups on the acrylic acid of pNIPAM-AAc can respond to pH stimulus by the transition in its protonated/deprotonated states. Hence, the spherical structure of the hydrogel network of pNIPAM-AAc changed its structure in response to the pH stimulus (Figure 4.5a). To further clarify this, we investigated pNIPAM-AAc spherical structures in different pH buffers from pH 3 to pH 11 (Figure 4.5b**)**. The addition of varying pH solutions led to swelling/shrinking of the spherical structure up to 300% in the volumetric ratio of the structure (Figure 4.5c). The repetition test for the swelling and the shrinking process was fully reversible at least during 5 cycles (Figure 4.5d), which demonstrates the superior repeatability of swelling/shrinking behavior of the MPH robot with high precision of the swelling ratio over cycles.

By utilizing the swelling of the pH-responsive pNIPAM-AAc inner drug carrier, the drug release test was carried out since on-demand therapeutic release is one of the challenges in medical microrobots for their targeted therapy. However, the drug releasing mechanism of the existed pollen grain-inspired microrobots are passive, while those presented in this work can perform drug release actively since the MPH robot can respond to pH changes. Due to their porous hydrogel network, the pollen-grain-inspired hydrogel adhesives presented here might serve pH. As a representative of this potential, we explored the impact of pH stimulus on pollen-grain-inspired

hydrogel adhesives. We first loaded a fluorescent small-molecule drug analog, CellTracker Deep Red Dye, into the porous network of the pollen-grain-inspired hydrogel attachment. To eliminate the effect of unstimulated stimulation, we first thoroughly washed the drug-loaded structures with Dulbecco's phosphate-buffered saline (DPBS) several times. Then, we introduced the pH 7.4 and pH 11 buffer solutions to the drug-loaded structures, where the release of the drug-analog molecule from the structures was measured by the fluorescent intensities inside the hydrogel network. When we exposed the structures to pH 11 buffer solution, we observed an immediate decrease in the fluorescent intensities due to the rapid swelling of the structures. As the structures swelled, the hydrogel size rapidly increased, and the encapsulated drug-analog molecules were released into the surrounding environment (Figure 4.5e-f). The response of the MPH robot was immediate to react within seconds, which is applicable for on-demand drug delivery functions. The release at pH 11 stopped, where 30% of the drug was still entrapped inside the hydrogel network. The uncompleted release could be explained by the molecular interactions between the drug molecules and the hydrogel network. [36] On the other hand, we observed no significant release at the pH 7.4 buffer solution since we did not observe swelling in this buffer solution (Figure 5e).

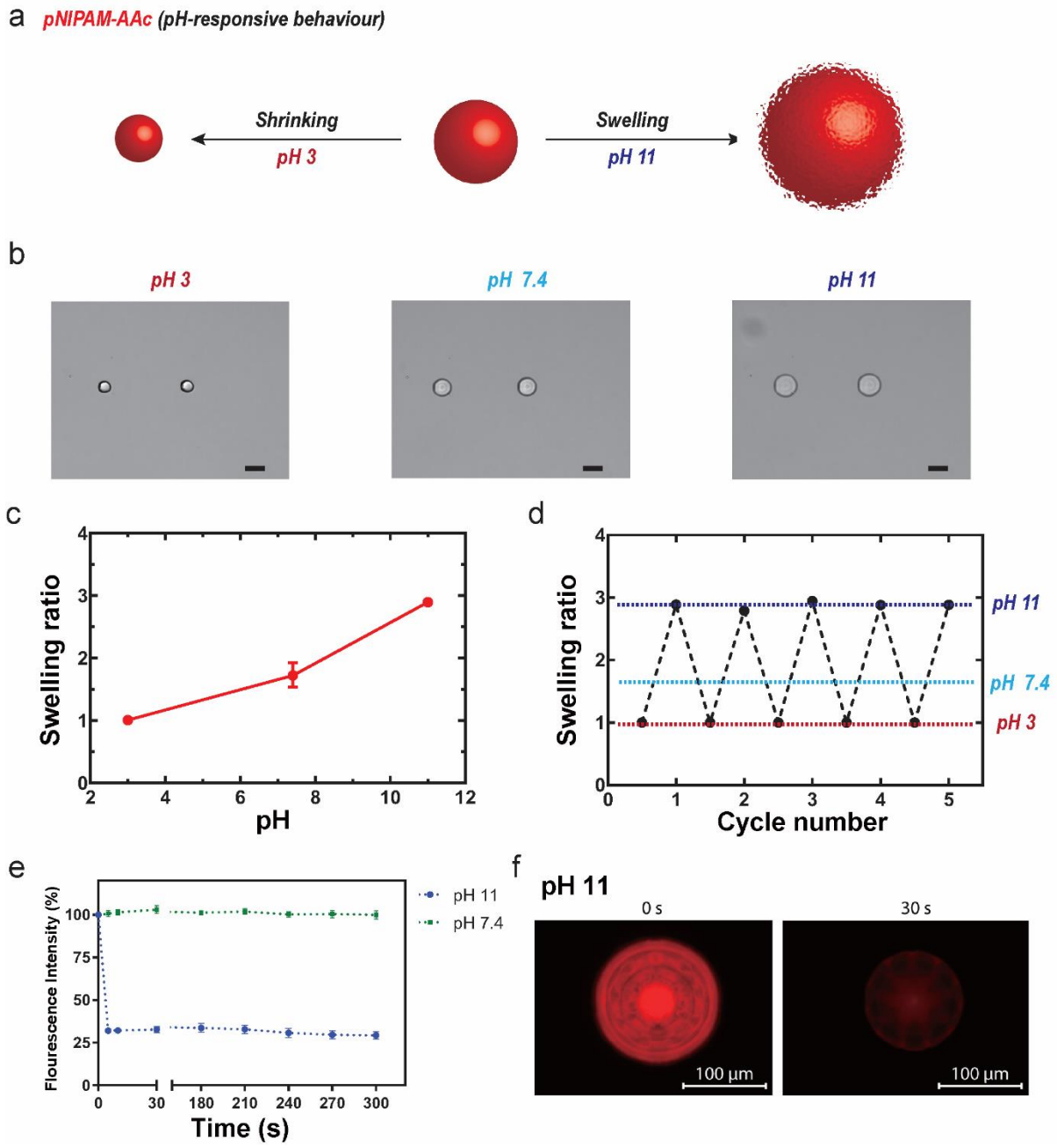

Figure 4.5 pH-responsive spherical structure of MPH robot using pNIPAM-AAc. (a) Schematic images of pH change-mediated drug release. (b) Optical images showing the pH-responsive spherical structures. (c) The swelling ratio for spherical patterns of pNIPAM-AAc hydrogels with pH change. (d) The repetition test of the pNIPAM-AAc inner cargo carrier sphere swelling cycles in response to pH change. (e) pH-mediated, structure swelling-driven drug release from the MPH

robot. (f) Fluorescence images of the drug-encapsulated MPH robot showing the drug release with pH-stimulated swelling behavior.

4.4 Summary

We have presented a novel strategy to fabricate the multifunctional pollen-grain-inspired hydrogel robot by 3D direct laser printing in order to enhance the functional diversity of microrobots in biological environments. Throughout the unique fabrication approach, we demonstrated multi-responsive hydrogel structures to decouple the stimuli inputs of magnetically actuated locomotion, temperature-responsive controllable attachment, and pH-responsive on-demand cargo release, respectively. The temperature-responsive outer crust shells made of pNIPAM enabled controlling the attachment of the microrobot by shrinking up to 49%, revealing the robot's spikes. In addition, the inner pollen-grain-inspired structure with spikes made of PETA with FePt nanoparticles demonstrated an improved attachment performance and magnetically guided locomotion along biological surfaces. The inner sphere made of pNIPAM-AAc successfully released drugs by pH-induced swelling. The proposed work here would be a groundwork to broaden the horizons of designing various medical robots and devices for implementing biomedical functions in the body.

Chapter 5. Conclusion and Outlook

5.1 Summary

In this thesis, we have explored how we can integrate stimuli-responsive materials, 3D laser lithography, and microrobotics effectively. Main objective of the thesis was to tackle the 3D-printed microrobots using stimuli-responsive materials for potential biomedical applications. In this chapter, the main findings and contributions of the thesis are summarized and an outlook on possible future applications is given.

5.1.1 3D-printed micro robot based on stimuli responsive materials

Firstly, it was proposed that 3D-printed spheres and double helical microrobots can be precisely steered by magnetic fields while at the same time the shape change (swelling and shrinking) is controlled by temperature, pH and divalent calcium ions. We demonstrate that the shape-change control with multiple inputs (temperature, pH, and divalent calcium ions) increases the control versatility where logically controlled patterns can enhance the adaptability of the functional task to various unstructured environments. As a proof of concept, the mobile microbots can be steered to penetrate narrow channels (with a diameter of 30 μm). Inside these channels, they can be reversibly swelled to clog the channel.

5.1.2 Octopus-inspired temperature-responsive soft robot

In order to avoid leaving unwanted secondary damage and a residue in the body, we design the 3D-printed untethered octopus-inspired hydrogel dry adhesive (OHA) that exhibits the heterogeneous volume changes of internal mechanical structures in response to temperature stimuli, leads adjusting adhesion strength in a controlled manner. We demonstrate this in concert with a small-scale wireless magnetic medical robot to deliver drug locally with attachment and successful

detachment by remote heating method, which suggests an alternative way to the current medical technology for delivering drug.

5.1.3 Multifunctional pollen-grain-inspired hydrogel robot

In order to conduct targeted therapeutic delivery in complex physiological environments with a minimally invasive approach, we exhibit a micro-scale multifunctional pollen-grain-inspired hydrogel robot that could conduct multiple functions in response to independent input stimuli. The 3D-printed wireless multifunctional pollen-grain-inspired robot (MPH) with controllable attachment demonstrates the diverse functionalities in response to three different stimuli, which are temperature-responsive controllable attachment, magnetically actuated locomotion, and pH-responsive on-demand drug delivery. We exhibit micro-scale wireless multifunctional robots to deliver a drug in a local region with controllable attachment and on-demand drug delivery, which suggests a novel way to micro-scale robotics for biomedical technology.

5.2 Future Outlook

Despite there has been considerable progress in 3D printed micro robotics with stimuli-responsive materials, a lot of critical challenges remain to be met for use in pragmatic applications. One of the most promising applications for the microrobot is in biomedical applications including target drug delivery, sensing, diagnosis, and gripper due to their micro size, low weight, high flexibility, and high sensitivity. As they develop, there is still numerous challenges regarding the toxicity of the material, method of stimuli excitation, and functionality of micro-robots for applying to the unstructured, untethered environment.

When it comes to use in biomedical application, biocompatibility and biodegradability of the 3D printed material are very crucial for operation inside the living organisms. Despite there

has been significant progress in toxicity, the photoinitiators used in fabrication process are still concerned for potential toxic effect on living systems. In addition, their property of biodegradation limits their use certain applications in real world. Hence, there is need for fabrication methods to reduce use of toxic photoinitator or minimization of photoinitiator residue after fabrication process.

Another dominant issue for use in biomedical or in vivo applications is mean of stimuli excitation. Functionality of stimuli-responsive material depends on their input based on external stimuli. However, external stimuli might be blocked by unstructured biological environment and their extent of the stimuli can be insufficient to function their roles in appropriate situations. Thus, finding the proper path that stimulus triggers the microrobot deeper inside the rough and unstructured environment like inside the human body is necessary for development of biomedical applications.

One promising route for the future would be the integration of multiple stimuli to a single microrobot. Combination of stimuli-responsive materials and their fabrications could make the microrobot operate different functions at a hard-to-reach sites like the human body. In this context, the introduction of novel stimuli responsive-materials with fabrication is necessary because it enables both remote-controlled functions and spatial localization in response to their stimuli. Like the one shown by the integration of different active structures with introduction of different stimuli-responsive materials in this dissertation, allow for independently active operation inside the unstructured environments.

Appendix A: Three-dimensional (3D) printing for microrobot fabrication using multi-stimuli-responsive materials

In this appendix, the fabrication of microrobot with different stimuli responsive materials was described. To realize such 3D geometries with a stimuli-responsive material, we fabricated microrobots using two-photon polymerization-based 3D printing. Briefly, the interaction of the focused femtosecond laser (wavelength of 780 nm) irradiation with the photoinitiator in a tight focal volume, called voxel, results in the initiation of a free-radical polymerization with the electrons within the precursor monomers. Computer-controlled scanning of the laser within the bulk volume of the precursor mixture solution thus facilitates the formation of complex 3D microstructures with submicrometer (as low as 100 nm) features. [40] To realize a fully reversible two-way response with the microrobot, we prepared a photocurable resin containing pNIPAM-AAc. We first optimized the fabrication process by applying different laser doses for the maximized structural fidelity of microrobot in three different dimensions (Figure A1).

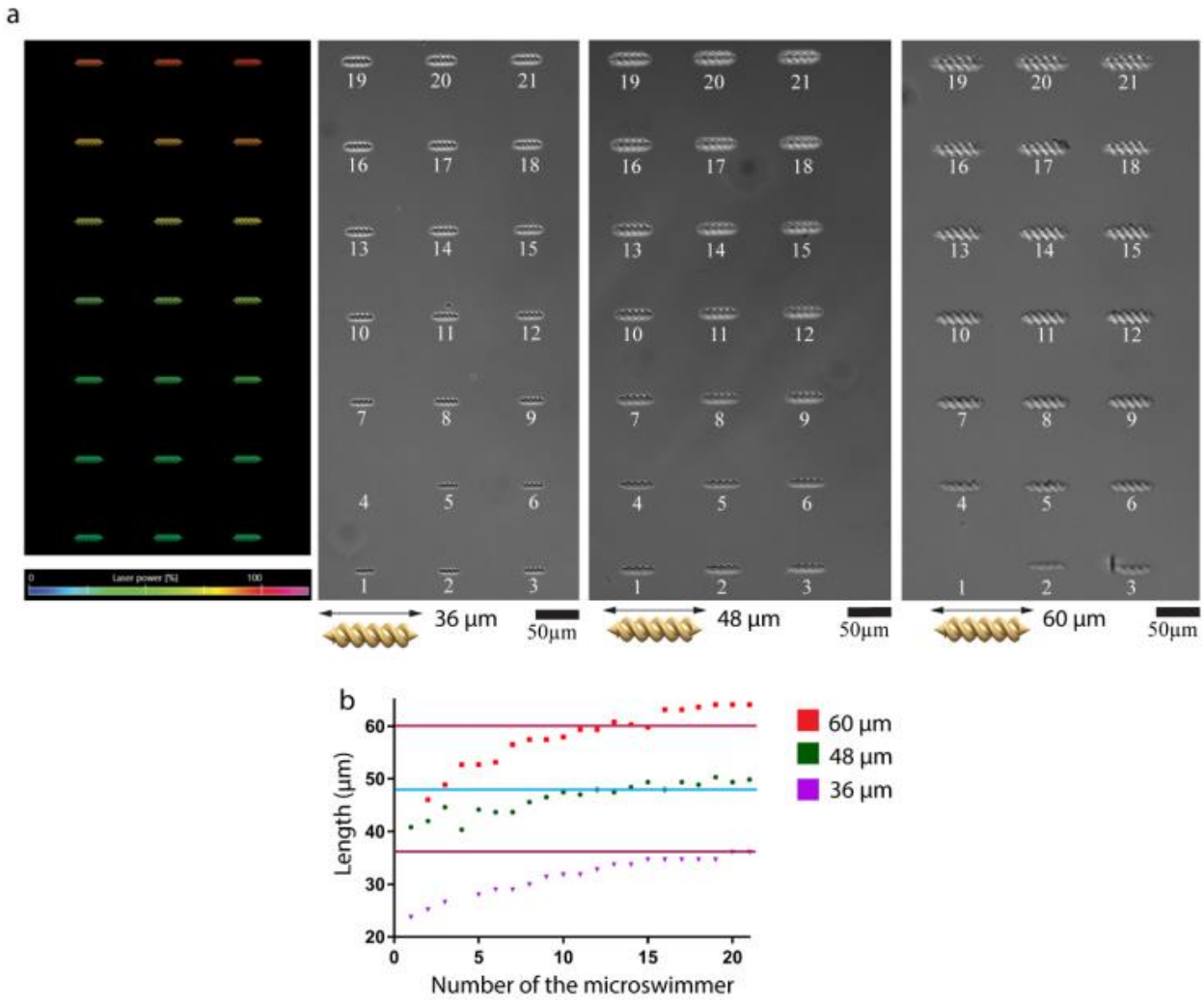

Figure A1. Optimization of the two-photon laser lithography fabrication for the maximized structural fidelity of microscrews in three different dimensions (36, 48, 60 µm lengths). (a) Color-coded description and microscopic images of a microscrews array design (36, 48, 60 µm) to be fabricated with varying laser powersin the range of 20-80 mW with 3 mW step size. (b) The structural quality was assessed under three classifications: underdose where microscrews were exposed to too low laser intensity so that the structures became smaller than their designated dimensions; overdose where the solution was exposed to too much laser intensity so that the structures became bigger than the design or were observed structural defects due to local overheating; acceptable dose where the

dimensions and features met their original design without any defects. The line in the graph indicates the dimension of design.

Throughout this thesis, two-photon laser lithography was used to fabricate the microrobots including stimuli-responsive materials. The cleaning of glass substrate includes ultrasonication in acetone, and isopropyl alcohol, and drying by nitrogen gas flow. The stimuli-responsive photo-resin mixture solution was dropped on a trichloro(1H,1H,2H,2H-perfluorooctyl)silane-modified glass substrate for avoiding detachment of the structures. A commercial Direct Laser Writing setup (Photonic Professional GT, Nanoscribe GmbH) with a 25×, NA = 0.8 oil immersion objective was used for the printing microrobot structures. Laser power and galvanometric mirror *x*- and *y*-scanning speeds were optimized for programmed stimuli-responsive functions. Depend on the robot designs, multiple steps of printing are required to possess multi-functionalities.

Appendix B: Optical images showing volume changes for pNIPAM and PEGDA hydrogels with temperature changes (27–45 °C)

In this appendix, the magnified optical images of pNIPAM and PEGDA hydrogels with different temperatures were described for better readability (Figure B1).

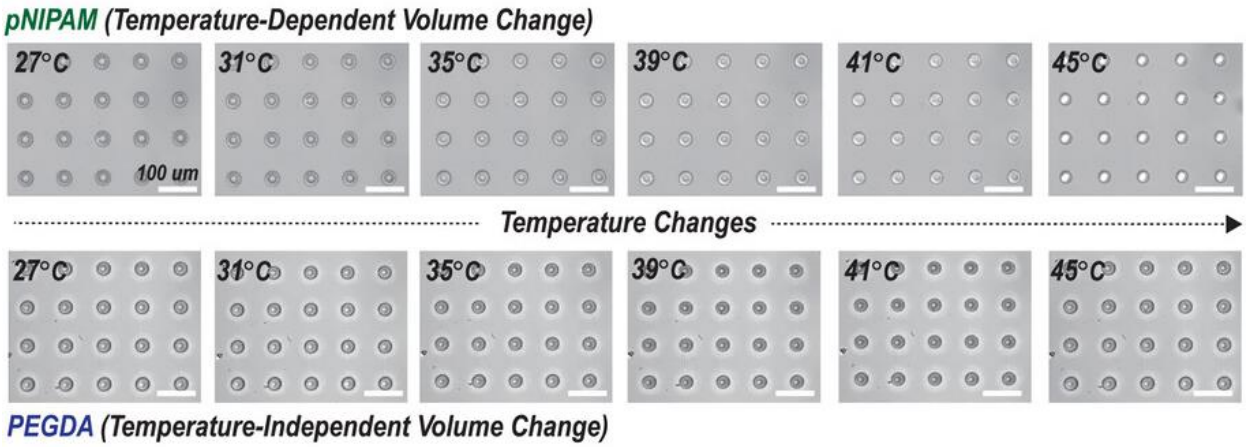

Figure B1. Magnified optical images showing real-time volume changes for spherical patterns of pNIPAM and PEGDA hydrogels with temperature changes (27–45 °C)

Appendix C: XRD spectrum data indicating the presence of FePt nanoparticles inside the PETA.

In this appendix, XRD spectrum data is shown to identify the presence of FePt nanoparticles inside the PETA (Figure C1).

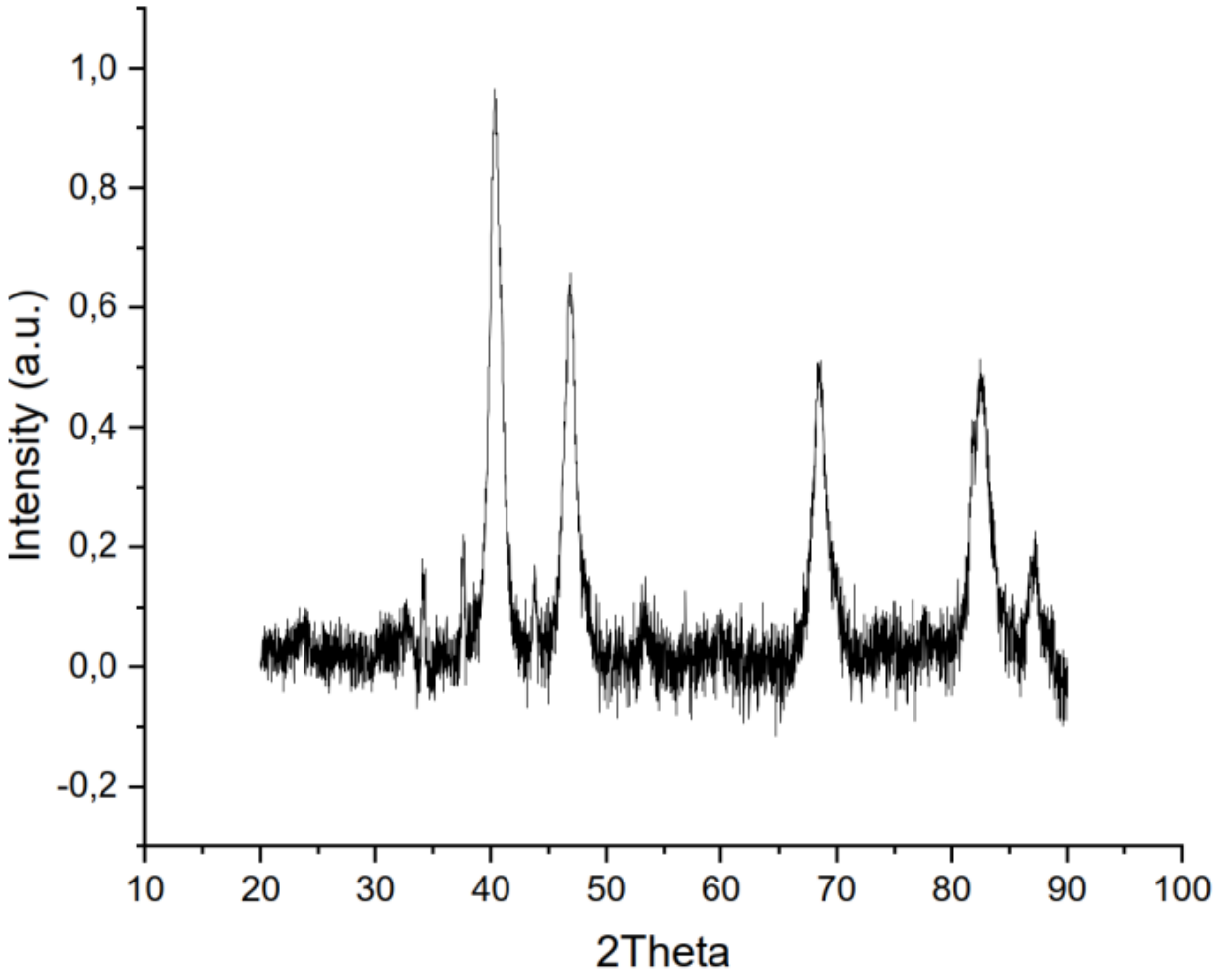

Figure C1. XRD spectrum data indicating the presence of FePt nanoparticles inside the PETA.

Bibliography

[1] S. H. Huang, P. Liu, A. Mokasdar, L. Hou, *The International Journal of Advanced Manufacturing Technology* **2013**, 67, 1191.

[2] W. E. Frazier, *Journal of Materials Engineering and Performance* **2014**, 23, 1917.

[3] D. Herzog, V. Seyda, E. Wycisk, C. Emmelmann, *Acta Materialia* **2016**, 117, 371.

[4] T. D. Ngo, A. Kashani, G. Imbalzano, K. T. Q. Nguyen, D. Hui, *Composites Part B: Engineering* **2018**, 143, 172.

[5] P. Parandoush, D. Lin, *Composite Structures* **2017**, 182, 36.

[6] S. C. Joshi, A. A. Sheikh, *Virtual and Physical Prototyping* **2015**, 10, 175.

[7] A. H. Espera, J. R. C. Dizon, Q. Chen, R. C. Advincula, *Progress in Additive Manufacturing* **2019**, 4, 245.

[8] E. Barnett, C. Gosselin, *Additive Manufacturing* **2015**, 7, 27.

[9] H. Dodziuk, *Kardiochirurgia i Torakochirurgia Polska/Polish Journal of Thoracic and Cardiovascular Surgery* **2016**, 13, 283.

[10] G. M. Paul, A. Rezaienia, P. Wen, S. Condoor, N. Parkar, W. King, T. Korakianitis, *Missouri medicine* **2018**, 115, 75.

[11] W. Xu, X. Wang, N. Sandler, S. Willför, C. Xu, *ACS Sustainable Chemistry & Engineering* **2018**, 6, 5663.

[12] S. Everton, P. Dickens, C. Tuck, B. Dutton, *Evaluation of laser ultrasonic testing for inspection of metal additive manufacturing*, SPIE, **2015**.

[13] H. Exner, M. Horn, A. Streek, F. Ullmann, L. Hartwig, P. Regenfuß, R. Ebert, *Virtual and Physical Prototyping* **2008**, 3, 3.

[14] N. Guo, M. C. Leu, *Frontiers of Mechanical Engineering* **2013**, 8, 215.

[15] K. S. Teh, *Frontiers of Mechanical Engineering* **2017**, 12, 490.

[16] C. M. González-Henríquez, F. E. Rodríguez-Umanzor, N. F. Acuña-Ruiz, G. E. Vera-Rojas, C. Terraza-Inostroza, N. A. Cohn-Inostroza, A. Utrera, M. A. Sarabia-Vallejos, J. Rodríguez-Hernández, *Polymers* **2022**, 14, 4041.

[17] A. Y. Lee, J. An, C. K. Chua, *Engineering* **2017**, 3, 663.

[18] F. Momeni, S. M.Mehdi Hassani.N, X. Liu, J. Ni, *Materials & Design* **2017**, 122, 42.

[19] Z. X. Khoo, J. E. M. Teoh, Y. Liu, C. K. Chua, S. Yang, J. An, K. F. Leong, W. Y. Yeong, *Virtual and Physical Prototyping* **2015**, 10, 103.

[20] T. Wang, J. Zhao, C. Weng, T. Wang, Y. Liu, Z. Han, Z. Zhang, *Journal of Materials Chemistry C* **2021**, 9, 7444.

[21] A. Concellón, P. Romero, M. Marcos, J. Barberá, C. Sánchez-Somolinos, M. Mizobata, T. Ogoshi, J. L. Serrano, J. del Barrio, *The Journal of Organic Chemistry* **2020**, 85, 8944.

[22] N. S. Awad, V. Paul, N. M. AlSawaftah, G. ter Haar, T. M. Allen, W. G. Pitt, G. A. Husseini, *ACS Pharmacology & Translational Science* **2021**, 4, 589.

[23] T.-Y. Huang, H.-W. Huang, D. D. Jin, Q. Y. Chen, J. Y. Huang, L. Zhang, H. L. Duan, *Science Advances* **2020**, 6, eaav8219.

[24] D. Jin, Q. Chen, T.-Y. Huang, J. Huang, L. Zhang, H. Duan, *Materials Today* **2020**, 32, 19.

[25] X. Huang, M. Ford, Z. J. Patterson, M. Zarepoor, C. Pan, C. Majidi, *Journal of Materials Chemistry B* **2020**, 8, 4539.

[26] S. Lim, R. A. Buswell, T. T. Le, S. A. Austin, A. G. F. Gibb, T. Thorpe, *Automation in Construction* **2012**, 21, 262.

[27] C. de Marco, C. C. J. Alcântara, S. Kim, F. Briatico, A. Kadioglu, G. de Bernardis, X. Chen, C. Marano, B. J. Nelson, S. Pané, *Advanced Materials Technologies* **2019**, 4, 1900332.
[28] M. Li, A. Pal, A. Aghakhani, A. Pena-Francesch, M. Sitti, *Nature Reviews Materials* **2022**, 7, 235.
[29] C. A. Spiegel, M. Hippler, A. Münchinger, M. Bastmeyer, C. Barner-Kowollik, M. Wegener, E. Blasco, *Advanced Functional Materials* **2020**, 30, 1907615.
[30] M. Guix, S. M. Weiz, O. G. Schmidt, M. Medina-Sánchez, *Particle & Particle Systems Characterization* **2018**, 35, 1700382.
[31] D. Martella, S. Nocentini, C. Parmeggiani, D. S. Wiersma, *Advanced Materials Technologies* **2019**, 4, 1800571.
[32] B. Wang, K. Kostarelos, B. J. Nelson, L. Zhang, *Advanced Materials* **2021**, 33, 2002047.
[33] K. E. Peyer, L. Zhang, B. J. Nelson, *Nanoscale* **2013**, 5, 1259.
[34] D. Schamel, A. G. Mark, J. G. Gibbs, C. Miksch, K. I. Morozov, A. M. Leshansky, P. Fischer, *ACS Nano* **2014**, 8, 8794.
[35] P. Cabanach, A. Pena-Francesch, D. Sheehan, U. Bozuyuk, O. Yasa, S. Borros, M. Sitti, *Advanced Materials* **2020**, 32, 2003013.
[36] H. Ceylan, N. O. Dogan, I. C. Yasa, M. N. Musaoglu, Z. U. Kulali, M. Sitti, *Science Advances* **2021**, 7, eabh0273.
[37] H. Ceylan, I. C. Yasa, O. Yasa, A. F. Tabak, J. Giltinan, M. Sitti, *ACS Nano* **2019**, 13, 3353.
[38] S. Binauld, M. H. Stenzel, *Chemical Communications* **2013**, 49, 2082.
[39] A. Abdollahi, H. Roghani-Mamaqani, B. Razavi, M. Salami-Kalajahi, *Polymer Chemistry* **2019**, 10, 5686.
[40] E. Diller, M. Sitti, *Advanced Functional Materials* **2014**, 24, 4397.
[41] A. Ryabchun, F. Lancia, A.-D. Nguindjel, N. Katsonis, *Soft Matter* **2017**, 13, 8070.
[42] S. Murdan, *Journal of Controlled Release* **2003**, 92, 1.
[43] H. Meng, J. Hu, *Journal of Intelligent Material Systems and Structures* **2010**, 21, 859.
[44] S. Hirotsu, Y. Hirokawa, T. Tanaka, *The Journal of Chemical Physics* **1987**, 87, 1392.
[45] D. Buenger, F. Topuz, J. Groll, *Progress in Polymer Science* **2012**, 37, 1678.
[46] M. Das, H. Zhang, E. Kumacheva, *Annual Review of Materials Research* **2006**, 36, 117.
[47] B. Jeong, A. Gutowska, *Trends in Biotechnology* **2002**, 20, 305.
[48] Y.-W. Lee, H. Ceylan, I. C. Yasa, U. Kilic, M. Sitti, *ACS Appl. Mater. Interfaces* **2021**, 13, 12759.
[49] D. H. Kang, S. M. Kim, B. Lee, H. Yoon, K.-Y. Suh, *Analyst* **2013**, 138, 6230.
[50] J. K. Oh, R. Drumright, D. J. Siegwart, K. Matyjaszewski, *Progress in Polymer Science* **2008**, 33, 448.
[51] C. Thanner, M. Eibelhuber, *Nanomaterials* **2021**, 11, 822.
[52] P. Erkoc, I. C. Yasa, H. Ceylan, O. Yasa, Y. Alapan, M. Sitti, *Advanced Therapeutics* **2019**, 2, 1800064.
[53] J. Fischer, M. Wegener, *Laser & Photonics Reviews* **2013**, 7, 22.
[54] A. Ovsianikov, B. N. Chichkov, in *Nanoelectronics and Photonics: From Atoms to Materials, Devices, and Architectures*, DOI: 10.1007/978-0-387-76499-3_12 (Eds: A. Korkin, F. Rosei), Springer New York, New York, NY **2008**, p. 427.
[55] M. Renner, G. von Freymann, *Advanced Optical Materials* **2014**, 2, 226.
[56] V. Hahn, P. Kiefer, T. Frenzel, J. Qu, E. Blasco, C. Barner-Kowollik, M. Wegener, *Advanced Functional Materials* **2020**, 30, 1907795.
[57] D. Iandolo, F. A. Pennacchio, V. Mollo, D. Rossi, D. Dannhauser, B. Cui, R. M. Owens, F. Santoro, *Advanced Biosystems* **2019**, 3, 1800103.
[58] C. Yeung, S. Chen, B. King, H. Lin, K. King, F. Akhtar, G. Diaz, B. Wang, J. Zhu, W. Sun, A. Khademhosseini, S. Emaminejad, *Biomicrofluidics* **2019**, 13, 064125.
[59] J. Bauer, A. Schroer, R. Schwaiger, O. Kraft, *Nature Materials* **2016**, 15, 438.
[60] G. Adam, A. Benouhiba, K. Rabenorosoa, C. Clévy, D. J. Cappelleri, *Advanced Intelligent Systems* **2021**, 3, 2000216.

[61] S. Jiang, Y. Hu, H. Wu, Y. Zhang, Y. Zhang, Y. Wang, Y. Zhang, W. Zhu, J. Li, D. Wu, J. Chu, *Advanced Materials* **2019**, 31, 1807507.
[62] C. Xin, L. Yang, J. Li, Y. Hu, D. Qian, S. Fan, K. Hu, Z. Cai, H. Wu, D. Wang, D. Wu, J. Chu, *Advanced Materials* **2019**, 31, 1808226.
[63] S. Zhu, Y. Bian, T. Wu, C. Chen, Y. Jiao, Z. Jiang, Z. Huang, E. Li, J. Li, J. Chu, Y. Hu, D. Wu, L. Jiang, *Nano Letters* **2020**, 20, 5513.
[64] M. Sitti, D. S. Wiersma, *Advanced Materials* **2020**, 32, 1906766.
[65] M. Hippler, E. Blasco, J. Qu, M. Tanaka, C. Barner-Kowollik, M. Wegener, M. Bastmeyer, *Nature Communications* **2019**, 10, 232.
[66] A. Nishiguchi, A. Mourran, H. Zhang, M. Möller, *Advanced Science* **2018**, 5, 1700038.
[67] V. Liimatainen, D.-M. Drotlef, D. Son, M. Sitti, *Advanced Materials* **2020**, 32, 2000497.
[68] S. Baik, D. W. Kim, Y. Park, T.-J. Lee, S. Ho Bhang, C. Pang, *Nature* **2017**, 546, 396.
[69] W.-G. Bae, H. Ko, J.-Y. So, H. Yi, C.-H. Lee, D.-H. Lee, Y. Ahn, S.-H. Lee, K. Lee, J. Jun, H.-H. Kim, N. L. Jeon, W. Jung, C.-S. Song, T. Kim, Y.-C. Kim, H. E. Jeong, *Science Translational Medicine* **2019**, 11, eaaw3329.
[70] T. Zhao, L. Yuan, T. Li, L. Chen, X. Li, J. Zhang, *ACS Appl. Mater. Interfaces* **2020**, 12, 55362.
[71] Y. Chen, J. Meng, Z. Gu, X. Wan, L. Jiang, S. Wang, *Advanced Functional Materials* **2020**, 30, 1905287.
[72] G. W. Hwang, H. J. Lee, D. W. Kim, T.-H. Yang, C. Pang, *Advanced Science* n/a, 2202978.
[73] A. Martinelli, G. A. Carru, L. D'Ilario, F. Caprioli, M. Chiaretti, F. Crisante, I. Francolini, A. Piozzi, *ACS Applied Materials & Interfaces* **2013**, 5, 4340.
[74] G. Huber, H. Mantz, R. Spolenak, K. Mecke, K. Jacobs, S. N. Gorb, E. Arzt, *Proceedings of the National Academy of Sciences* **2005**, 102, 16293.
[75] K.-Y. Seong, M.-S. Seo, D. Y. Hwang, E. D. O'Cearbhaill, S. Sreenan, J. M. Karp, S. Y. Yang, *Journal of Controlled Release* **2017**, 265, 48.
[76] W. Sun, P. Neuzil, T. S. Kustandi, S. Oh, V. D. Samper, *Biophysical Journal* **2005**, 89, L14.
[77] S. Y. Yang, E. D. O'Cearbhaill, G. C. Sisk, K. M. Park, W. K. Cho, M. Villiger, B. E. Bouma, B. Pomahac, J. M. Karp, *Nature Communications* **2013**, 4, 1702.
[78] S. Ito, S. N. Gorb, *ACS Applied Materials & Interfaces* **2019**, 11, 24691.
[79] D. Shin, W. T. Choi, H. Lin, Z. Qu, V. Breedveld, J. C. Meredith, *Nature Communications* **2019**, 10, 1379.
[80] Y. Wang, L. Shang, G. Chen, C. Shao, Y. Liu, P. Lu, F. Rong, Y. Zhao, *Applied Materials Today* **2018**, 13, 303.
[81] R. C. Mundargi, M. G. Potroz, S. Park, H. Shirahama, J. H. Lee, J. Seo, N.-J. Cho, *Small* **2016**, 12, 1167.
[82] W. Wang, G. Yang, H. Cui, J. Meng, S. Wang, L. Jiang, *Advanced Healthcare Materials* **2017**, 6, 1700003.
[83] T. Maric, M. Z. M. Nasir, N. F. Rosli, M. Budanović, R. D. Webster, N.-J. Cho, M. Pumera, *Advanced Functional Materials* **2020**, 30, 2000112.
[84] K. Terpilowski, D. Rymuszka, *Glass Physics and Chemistry* **2016**, 42, 535.
[85] Y.-W. Lee, S. Chun, D. Son, X. Hu, M. Schneider, M. Sitti, *Adv. Mater.* **2022**, 34, 2109325.
[86] H. Ceylan, J. Giltinan, K. Kozielski, M. Sitti, *Lab on a Chip* **2017**, 17, 1705.
[87] L. Hines, K. Petersen, G. Z. Lum, M. Sitti, *Adv. Mater.* **2017**, 29, 1603483.
[88] M. Sitti, H. Ceylan, W. Hu, J. Giltinan, M. Turan, S. Yim, E. Diller, *Proceedings of the IEEE* **2015**, 103, 205.
[89] F. Qiu, S. Fujita, R. Mhanna, L. Zhang, B. R. Simona, B. J. Nelson, *Advanced Functional Materials* **2015**, 25, 1666.
[90] I. C. Yasa, A. F. Tabak, O. Yasa, H. Ceylan, M. Sitti, *Advanced Functional Materials* **2019**, 29, 1808992.

[91] M. Dong, X. Wang, X.-Z. Chen, F. Mushtaq, S. Deng, C. Zhu, H. Torlakcik, A. Terzopoulou, X.-H. Qin, X. Xiao, J. Puigmartí-Luis, H. Choi, A. P. Pêgo, Q.-D. Shen, B. J. Nelson, S. Pané, *Advanced Functional Materials* **2020**, 30, 1910323.
[92] I. C. Yasa, H. Ceylan, U. Bozuyuk, A.-M. Wild, M. Sitti, *Sci. Rob.* **2020**, 5, eaaz3867.
[93] S. Tasoglu, E. Diller, S. Guven, M. Sitti, U. Demirci, *Nature Communications* **2014**, 5, 3124.
[94] A. Sydney Gladman, E. A. Matsumoto, R. G. Nuzzo, L. Mahadevan, J. A. Lewis, *Nat. Mater.* **2016**, 15, 413.
[95] A. I. Antoniou, S. Giofrè, P. Seneci, D. Passarella, S. Pellegrino, *Drug Discovery Today* **2021**, 26, 1794.
[96] Y. Kim, H. Yuk, R. Zhao, S. A. Chester, X. Zhao, *Nature* **2018**, 558, 274.
[97] J. Liu, O. Erol, A. Pantula, W. Liu, Z. Jiang, K. Kobayashi, D. Chatterjee, N. Hibino, L. H. Romer, S. H. Kang, T. D. Nguyen, D. H. Gracias, *ACS Applied Materials & Interfaces* **2019**, 11, 8492.
[98] L. Vannozzi, I. C. Yasa, H. Ceylan, A. Menciassi, L. Ricotti, M. Sitti, *Macromolecular Bioscience* **2018**, 18, 1700377.
[99] Y. Hu, Z. Wang, D. Jin, C. Zhang, R. Sun, Z. Li, K. Hu, J. Ni, Z. Cai, D. Pan, X. Wang, W. Zhu, J. Li, D. Wu, L. Zhang, J. Chu, *Advanced Functional Materials* **2020**, 30, 1907377.
[100] H. Y. Jeong, B. H. Woo, N. Kim, Y. C. Jun, *Scientific Reports* **2020**, 10, 6258.
[101] H.-W. Huang, M. S. Sakar, A. J. Petruska, S. Pané, B. J. Nelson, *Nature Communications* **2016**, 7, 12263.
[102] K. Yoshida, H. Onoe, *Advanced Intelligent Systems* **2020**, 2, 2000095.
[103] E. Kim, S. Jeon, H.-K. An, M. Kianpour, S.-W. Yu, J.-y. Kim, J.-C. Rah, H. Choi, *Science Advances* **2020**, 6, eabb5696.
[104] Y. Alapan, U. Bozuyuk, P. Erkoc, A. C. Karacakol, M. Sitti, *Sci. Rob.* **2020**, 5, eaba5726.
[105] U. Bozuyuk, O. Yasa, I. C. Yasa, H. Ceylan, S. Kizilel, M. Sitti, *ACS Nano* **2018**, 12, 9617.
[106] H. G. Schild, *Progress in Polymer Science* **1992**, 17, 163.
[107] M. Hippler, E. D. Lemma, S. Bertels, E. Blasco, C. Barner-Kowollik, M. Wegener, M. Bastmeyer, *Advanced Materials* **2019**, 31, 1808110.
[108] H. Ceylan, I. C. Yasa, M. Sitti, *Adv. Mater.* **2017**, 29, 1605072.
[109] J. K. Hohmann, M. Renner, E. H. Waller, G. von Freymann, *Advanced Optical Materials* **2015**, 3, 1488.
[110] S. Kawata, H.-B. Sun, T. Tanaka, K. Takada, *Nature* **2001**, 412, 697.
[111] A. Ovsianikov, S. Mühleder, J. Torgersen, Z. Li, X.-H. Qin, S. Van Vlierberghe, P. Dubruel, W. Holnthoner, H. Redl, R. Liska, J. Stampfl, *Langmuir* **2014**, 30, 3787.
[112] S. R. Goudu, I. C. Yasa, X. Hu, H. Ceylan, W. Hu, M. Sitti, *Advanced Functional Materials* **2020**, 30, 2004975.
[113] C. Peters, V. Costanza, S. Pané, B. J. Nelson, C. Hierold, presented at 2015 Transducers - 2015 18th International Conference on Solid-State Sensors, Actuators and Microsystems (TRANSDUCERS), 21-25 June 2015, **2015**.
[114] A. Aziz, S. Pane, V. Iacovacci, N. Koukourakis, J. Czarske, A. Menciassi, M. Medina-Sánchez, O. G. Schmidt, *ACS Nano* **2020**, 14, 10865.
[115] A. Halder, Y. Sun, *Biosensors and Bioelectronics* **2019**, 139, 111334.
[116] W. Hu, G. Z. Lum, M. Mastrangeli, M. Sitti, *Nat.* **2018**, 554, 81.
[117] K. L. Kozielski, A. Jahanshahi, H. B. Gilbert, Y. Yu, Ö. Erin, D. Francisco, F. Alosaimi, Y. Temel, M. Sitti, *Sci. Adv.* **2021**, 7, eabc4189.
[118] C. S. X. Ng, M. W. M. Tan, C. Xu, Z. Yang, P. S. Lee, G. Z. Lum, *Adv. Mater.* **2021**, 33, 2003558.
[119] Z. Wu, L. Li, Y. Yang, P. Hu, Y. Li, S.-Y. Yang, L. V. Wang, W. Gao, *Sci. Rob.* **2019**, 4, eaax0613.
[120] K. T. Nguyen, G. Go, Z. Jin, B. A. Darmawan, A. Yoo, S. Kim, M. Nan, S. B. Lee, B. Kang, C.-S. Kim, H. Li, D. Bang, J.-O. Park, E. Choi, *Advanced Healthcare Materials* **2021**, 10, 2001681.
[121] S. Tang, F. Zhang, H. Gong, F. Wei, J. Zhuang, E. Karshalev, B. Esteban-Fernández de Ávila, C. Huang,

Z. Zhou, Z. Li, L. Yin, H. Dong, R. H. Fang, X. Zhang, L. Zhang, J. Wang, *Science Robotics* **2020**, 5, eaba6137.
[122] J. Li, M. Pumera, *Chem. Soc. Rev.* **2021**, 50, 2794.
[123] Z. Ren, W. Hu, X. Dong, M. Sitti, *Nat. Commun.* **2019**, 10, 2703.
[124] Z. Ren, R. Zhang, R. H. Soon, Z. Liu, W. Hu, P. R. Onck, M. Sitti, *Science Advances* **2021**, 7, eabh2022.
[125] M. Medina-Sánchez, V. Magdanz, M. Guix, V. M. Fomin, O. G. Schmidt, *Adv. Funct. Mater.* **2018**, 28, 1707228.
[126] D. D. Damian, K. Price, S. Arabagi, I. Berra, Z. Machaidze, S. Manjila, S. Shimada, A. Fabozzo, G. Arnal, D. Van Story, J. D. Goldsmith, A. T. Agoston, C. Kim, R. W. Jennings, P. D. Ngo, M. Manfredi, P. E. Dupont, *Science Robotics* **2018**, 3, eaaq0018.
[127] L. Li, B. Ouellette, W. A. Stoy, E. J. Garren, T. L. Daigle, C. R. Forest, C. Koch, H. Zeng, *Nature Communications* **2017**, 8, 15604.
[128] C. Pang, J. H. Koo, A. Nguyen, J. M. Caves, M.-G. Kim, A. Chortos, K. Kim, P. J. Wang, J. B.-H. Tok, Z. Bao, *Advanced Materials* **2015**, 27, 634.
[129] Z. Bao, M. Gao, Y. Sun, R. Nian, M. Xian, *Materials Science and Engineering: C* **2020**, 111, 110796.
[130] L. Ge, S. Chen, *Polymers* **2020**, 12, 939.
[131] J. Li, A. D. Celiz, J. Yang, Q. Yang, I. Wamala, W. Whyte, B. R. Seo, N. V. Vasilyev, J. J. Vlassak, Z. Suo, D. J. Mooney, *Science* **2017**, 357, 378.
[132] H. Yuk, C. E. Varela, C. S. Nabzdyk, X. Mao, R. F. Padera, E. T. Roche, X. Zhao, *Nature* **2019**, 575, 169.
[133] N. Annabi, K. Yue, A. Tamayol, A. Khademhosseini, *European Journal of Pharmaceutics and Biopharmaceutics* **2015**, 95, 27.
[134] H. Khoshmohabat, S. Paydar, H. M. Kazemi, B. Dalfardi, *Trauma monthly* **2016**, 21, e26023.
[135] T. B. Reece, T. S. Maxey, I. L. Kron, *The American Journal of Surgery* **2001**, 182, S40.
[136] G. M. Taboada, K. Yang, M. J. N. Pereira, S. S. Liu, Y. Hu, J. M. Karp, N. Artzi, Y. Lee, *Nature Reviews Materials* **2020**, 5, 310.
[137] R. K. Jayne, T. J. Stark, J. B. Reeves, D. J. Bishop, A. E. White, *Advanced Materials Technologies* **2018**, 3, 1700293.
[138] M. Mooney, *Journal of Applied Physics* **1940**, 11, 582.
[139] S. Chun, D. W. Kim, S. Baik, H. J. Lee, J. H. Lee, S. H. Bhang, C. Pang, *Advanced Functional Materials* **2018**, 28, 1805224.
[140] Y. Guan, Y. Zhang, *Soft Matter* **2011**, 7, 6375.
[141] P. M. Reddy, P. Venkatesu, *J. Phys. Chem. B* **2011**, 115, 4752.
[142] S. Schmidt, M. Zeiser, T. Hellweg, C. Duschl, A. Fery, H. Möhwald, *Advanced Functional Materials* **2010**, 20, 3235.
[143] Q. Shi, H. Xia, P. Li, Y.-S. Wang, L. Wang, S.-X. Li, G. Wang, C. Lv, L.-G. Niu, H.-B. Sun, *Advanced Optical Materials* **2017**, 5, 1700442.
[144] S. Sugiura, K. Sumaru, K. Ohi, K. Hiroki, T. Takagi, T. Kanamori, *Sensors and Actuators A: Physical* **2007**, 140, 176.
[145] H. Zhang, A. Mourran, M. Möller, *Nano Letters* **2017**, 17, 2010.
[146] Y.-W. Lee, J.-K. Kim, U. Bozuyuk, N. O. Dogan, M. T. A. Khan, A. Shiva, A.-M. Wild, M. Sitti, *Advanced Materials* n/a, 2209812.
[147] M. Cianchetti, C. Laschi, A. Menciassi, P. Dario, *Nat. Rev. Mater.* **2018**, 3, 143.
[148] S. Fusco, M. S. Sakar, S. Kennedy, C. Peters, R. Bottani, F. Starsich, A. Mao, G. A. Sotiriou, S. Pané, S. E. Pratsinis, D. Mooney, B. J. Nelson, *Adv. Mater.* **2014**, 26, 952.
[149] M. Sitti, H. Ceylan, W. Hu, J. Giltinan, M. Turan, S. Yim, E. Diller, *Proc IEEE Inst Electr Electron Eng* **2015**, 103, 205.
[150] X. Hu, I. C. Yasa, Z. Ren, S. R. Goudu, H. Ceylan, W. Hu, M. Sitti, *Sci. Adv.* **2021**, 7, eabe8436.
[151] T. Wang, Z. Ren, W. Hu, M. Li, M. Sitti, *Sci. Adv.* **2021**, 7, eabf7364.

[152] U. Bozuyuk, Y. Alapan, A. Aghakhani, M. Yunusa, M. Sitti, *PNAS* **2021**, 118, e2022090118.
[153] N. O. Dogan, H. Ceylan, E. Suadiye, D. Sheehan, A. Aydin, I. C. Yasa, A.-M. Wild, G. Richter, M. Sitti, *Small* **2022**, 18, 2204016.
[154] M. P. Kummer, J. J. Abbott, B. E. Kratochvil, R. Borer, A. Sengul, B. J. Nelson, *IEEE Transactions on Robotics* **2010**, 26, 1006.
[155] J. Li, X. Li, T. Luo, R. Wang, C. Liu, S. Chen, D. Li, J. Yue, S.-h. Cheng, D. Sun, *Sci. Rob.* **2018**, 3, eaat8829.
[156] C. C. Mayorga-Martinez, M. Fojtů, J. Vyskočil, N.-J. Cho, M. Pumera, *Adv. Funct. Mater.* **2022**, 32, 2207272.
[157] Y. Alapan, B. Yigit, O. Beker, A. F. Demirörs, M. Sitti, *Nat. Mater.* **2019**, 18, 1244.
[158] U. Bozuyuk, E. Suadiye, A. Aghakhani, N. O. Dogan, J. Lazovic, M. E. Tiryaki, M. Schneider, A. C. Karacakol, S. O. Demir, G. Richter, M. Sitti, *Adv. Funct. Mater.* **2022**, 32, 2109741.
[159] J. Giltinan, V. Sridhar, U. Bozuyuk, D. Sheehan, M. Sitti, *Adv. Intell. Syst.* **2021**, 3, 2000204.
[160] P. Wrede, O. Degtyaruk, S. K. Kalva, X. L. Deán-Ben, U. Bozuyuk, A. Aghakhani, B. Akolpoglu, M. Sitti, D. Razansky, *Sci. Adv.* **2022**, 8, eabm9132.
[161] S. Palagi, A. G. Mark, S. Y. Reigh, K. Melde, T. Qiu, H. Zeng, C. Parmeggiani, D. Martella, A. Sanchez-Castillo, N. Kapernaum, F. Giesselmann, D. S. Wiersma, E. Lauga, P. Fischer, *Nat. Mater.* **2016**, 15, 647.
[162] A. Pena-Francesch, J. Giltinan, M. Sitti, *Nat. Commun.* **2019**, 10, 3188.
[163] X. Ma, A. C. Hortelão, T. Patiño, S. Sánchez, *ACS Nano* **2016**, 10, 9111.
[164] X. Zhao, K. Gentile, F. Mohajerani, A. Sen, *Acc. Chem. Res.* **2018**, 51, 2373.
[165] V. Sridhar, F. Podjaski, Y. Alapan, J. Kröger, L. Grunenberg, V. Kishore, B. V. Lotsch, M. Sitti, *Sci. Rob.* **2022**, 7, eabm1421.
[166] A. Aghakhani, O. Yasa, P. Wrede, M. Sitti, *PNAS* **2020**, 117, 3469.
[167] J.-F. Louf, N. Bertin, B. Dollet, O. Stephan, P. Marmottant, *Adv. Mater. Interfaces* **2018**, 5, 1800425.
[168] B. J. Nelson, I. K. Kaliakatsos, J. J. Abbott, *Annu. Rev. Biomed. Eng.* **2010**, 12, 55.
[169] F. Zhang, R. Mundaca-Uribe, N. Askarinam, Z. Li, W. Gao, L. Zhang, J. Wang, *Adv. Mater.* **2022**, 34, 2107177.
[170] H. Ceylan, I. C. Yasa, U. Kilic, W. Hu, M. Sitti, *Prog. Biomed. Eng.* **2019**, 1, 012002.
[171] F. G. Downs, D. J. Lunn, M. J. Booth, J. B. Sauer, W. J. Ramsay, R. G. Klemperer, C. J. Hawker, H. Bayley, *Nat. Chem.* **2020**, 12, 363.
[172] J. Huang, Y. Liu, Y. Yang, Z. Zhou, J. Mao, T. Wu, J. Liu, Q. Cai, C. Peng, Y. Xu, B. Zeng, W. Luo, G. Chen, C. Yuan, L. Dai, *Sci. Rob.* **2021**, 6, eabe1858.
[173] Z. Ma, C. Bourquard, Q. Gao, S. Jiang, T. De Iure-Grimmel, R. Huo, X. Li, Z. He, Z. Yang, G. Yang, Y. Wang, E. Lam, Z.-h. Gao, O. Supponen, J. Li, *Sci.* **2022**, 377, 751.
[174] M. P. Murphy, B. Aksak, M. Sitti, *Small* **2009**, 5, 170.
[175] H.-W. Huang, F. E. Uslu, P. Katsamba, E. Lauga, M. S. Sakar, B. J. Nelson, *Sci. Adv.* **2019**, 5, eaau1532.
[176] H. Lu, M. Zhang, Y. Yang, Q. Huang, T. Fukuda, Z. Wang, Y. Shen, *Nat. Commun.* **2018**, 9, 3944.
[177] A. Le Duigou, G. Chabaud, F. Scarpa, M. Castro, *Adv. Funct. Mater.* **2019**, 29, 1903280.
[178] M. Sun, Q. Liu, X. Fan, Y. Wang, W. Chen, C. Tian, L. Sun, H. Xie, *Small* **2020**, 16, 1906701.
[179] M. Sun, K. F. Chan, Z. Zhang, L. Wang, Q. Wang, S. Yang, S. M. Chan, P. W. Y. Chiu, J. J. Y. Sung, L. Zhang, *Adv. Mater.* **2022**, 34, 2201888.
[180] Y. Yu, L. He, J. Xu, J. Li, S. Jiang, G. Han, B. Jiang, W. Lei, W. Yang, Y. Hou, *Nano Res.* **2022**, 15, 446, 451.
[181] E. Nader, S. Skinner, M. Romana, R. Fort, N. Lemonne, N. Guillot, A. Gauthier, S. Antoine-Jonville, C. Renoux, M.-D. Hardy-Dessources, *Front. Physiol.* **2019**, 10, 1329.
[182] H. Jia, J. Flommersfeld, M. Heymann, S. K. Vogel, H. G. Franquelim, D. B. Brückner, H. Eto, C. P. Broedersz, P. Schwille, *Nat. Mater.* **2022**, 21, 703.

[183] J. C. Breger, C. Yoon, R. Xiao, H. R. Kwag, M. O. Wang, J. P. Fisher, T. D. Nguyen, D. H. Gracias, *ACS Appl. Mater. Interfaces* **2015**, 7, 3398.
[184] L. Dong, A. K. Agarwal, D. J. Beebe, H. Jiang, *Nat.* **2006**, 442, 551.
[185] X.-J. Ju, L.-Y. Chu, X.-L. Zhu, L. Hu, H. Song, W.-M. Chen, *Smart Mater. Struct.* **2006**, 15, 1767.
[186] C. Yoon, R. Xiao, J. Park, J. Cha, T. D. Nguyen, D. H. Gracias, *Smart Mater. Struct.* **2014**, 23, 094008.
[187] Y. Wu, X. Dong, J.-k. Kim, C. Wang, M. Sitti, *Sci. Adv.* **2022**, 8, eabn3431.
[188] A. Kaiser, A. Snezhko, I. S. Aranson, *Sci. Adv.* **2017**, 3, e1601469.